Interface and catalyst investigation for solar water splitting

Grenzflächen- und Katalysatoruntersuchungen zur photochemischen Wasserspaltung

Zur Erlangung des akademischen Grades Doktor-Ingenieur (Dr.-Ing.)
genehmigte Dissertation von Joachim Klett aus Reutlingen

Darmstadt, 2016 — D 17

TECHNISCHE
UNIVERSITÄT
DARMSTADT

Eduard-Zintl-Insitut für
für Anorganische und
Physikalische Chemie
AK Schäfer

Surface Science

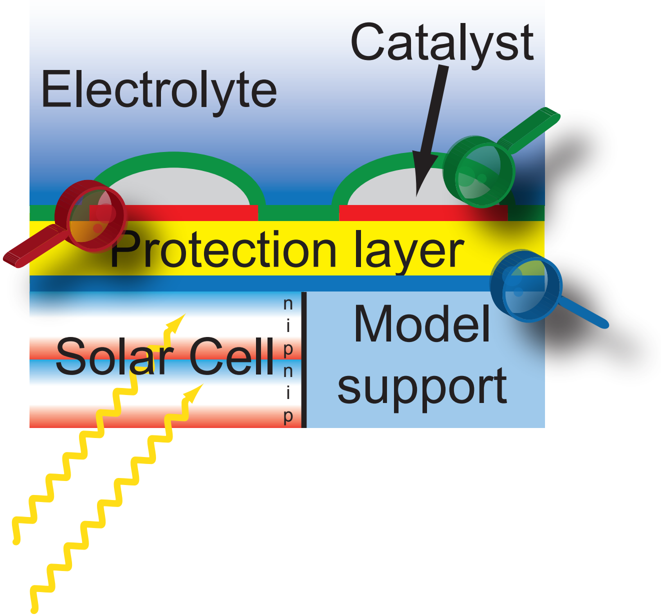

Interface and catalyst investigation for solar water splitting

Grenzflächen- und Katalysatoruntersuchungen zur photochemischen Wasserspaltung

Vom Fachbereich Chemie
der Technischen Universität Darmstadt

zur Erlangung des akademischen Grades eines

Doktor-Ingenieurs (Dr.-Ing.)

genehmigte
Dissertation

vorgelegt von

Joachim Klett
aus Reutlingen

Referent:	Prof. Dr. Rolf Schäfer
Korreferent:	Prof. Dr. Wolfram Jaegermann

Tag der Einreichung:	04. Februar 2016
Tag der mündlichen Prüfung:	22. März 2016

Darmstadt 2016

D 17

Erklärung zur Dissertation

Hiermit versichere ich, die vorliegende Dissertation ohne Hilfe Dritter nur mit den angegebenen Quellen und Hilfsmitteln angefertigt zu haben. Alle Stellen, die aus Quellen entnommen wurden, sind als solche kenntlich gemacht. Diese Arbeit hat in gleicher oder ähnlicher Form noch keiner Prüfungsbehörde vorgelegen.

Darmstadt, den 04. Februar 2016

(Joachim Klett)

Abstract

English:

In this thesis model experiments for a photoelectrochemical water splitting device were performed. The goal was to identify loss mechanisms that reduce the efficiency of the photoelectrochemical device. This includes losses associated with solid state contacts, i.e. charge transfer into the protection layer and catalyst particles, as well as overvoltage losses encountered during catalysis.

Additionally, fundamental photoelectron spectroscopy measurements revealed the complicated nature of small supported catalyst particles. Here, a direct dependence of their electronic structure with respect to their substrate material and deposition techniques was identified. Furthermore, subsequent water adsorption also changes the energetic alignment between support and catalyst.

Deutsch:

In dieser Arbeit wurden Modellexperimente zum Verständnis einer photoelektrochemischen Zelle zur Wasserspaltung durchgeführt. Das Ziel war hierbei die Identifikation der auftretenden Verlustmechanismen, welche die Effizienz der elektrochemischen Zelle mindern. Hierzu müssen sowohl Verluste an Festkörpergrenzflächen, als auch Überspannungsverluste des Katalysators berücksichtigt werden.

Dazu wurden grundlegende Untersuchungen mit Hilfe der Photoelektronspektroskopie an geträgerten Katalysatorpartikeln vorgenommen. Hierbei wurde festgestellt, dass die elektronische Struktur dieser Partikel sowohl vom Substratmaterial, als auch der Depositionsmethode abhängt. Sobald zusätzlich Wasser auf der Oberfläche adsorbiert wird, ändert sich wiederum die elektronische Anpassung zwischen Substrat und Katalysator.

Contents

Acronyms

ALD: Atomic layer deposition

BE: Binding energy

CAD: Computer aided design

CB: Conduction band

CV: Cyclic voltammetry

CVD: Chemical vapor deposition

DFT: Density functional theory

DOS: Density of states

ECAS: Electrochemically active surface area

FWHM: Full width at half maximum

H_{opd}: Over potential deposited hydrogen

H_{upd}: Under potential deposited hydrogen

HER: Hydrogen evolution reaction

HOMO: Highest occupied molecular orbital

HOPG: Highly oriented pyrolytic graphite

HOR: Hydrogen oxidation reaction

IMFP: Inelastic mean free path

ITO: Indium-tin-oxide

LEED: Low energy electron diffraction

MO: Molecular orbital

MPP: Maximum power point

NBO: nonbonding oxygen

OCP: Open circuit potential

OER: Oxygen evolution reaction

ORR: Oxygen reduction reaction

PES: Photoelectron spectrocopy

RHE: Reversible hydrogen electrode

S2H: Solar to hydrogen

SEM: Scanning electron mircroscopy

SHE: Standard hydrogen electrode

SXPS: Synchrotron XPS

UHV: Ultra-high vacuum

UPS: Ultraviolet photoelectron spectroscopy

VB: Valence band

VBO: Valence band offset

XPS: X-ray photoelectron spectroscopy

XRD: X-Ray diffraction

1 Introduction

In 1874 Jules Vernes wrote his world-renowned novel "The mysterious island". In it, captain Harding fathered the famous quote:

> "*Water will be the coal of the future*"

Even today, it still stands representative for a clean, abundant and regenerative energy supply. Although gaining energy directly from water is unfortunately forbidden, he was quite close to our nowadays discussed hydrogen based economy. With major car manufactures recently releasing first retail-ready hydrogen cars, a switch from fossil fuels seems to become more probable [1]. Consequently, to supply the fuel for these cars an efficient and clean production process needs to be established. The most prominent examples for these renewable energy sources are wind and solar power.

A further advantage of hydrogen as the energy carrier is that it allows to buffer the discontinuous operation of the renewable energy sources, which today put a major challenge on the electric grid. Still, hydrogen is in competition with other possible technologies like lithium ion batteries, redox flow cells and the hydrogenation of carbon dioxide using the Fischer-Tropsch synthesis. However, the latter process also needs hydrogen to start the synthesis process.

In this thesis, the splitting of water in order to release hydrogen as an energy carrier, will be in focus. Especially the photovoltaic splitting of water is of interest, since it is emission free and environmentally friendly. The abundance of contemporary books regarding the topic of water splitting underlines that it is one of the "hot topics" of today's research [2–7].

In this context, the SPP 1613 was founded by the Deutsche Forschungsgesellschaft (DFG) in 2012 with the goal to investigate systems that enable the clean production of hydrogen from water using sunlight. The project consist of three branches. The first branch are "photovoltaic devises" that focus on the production of solar cells or photoelectrochemical devices delivering the necessary electrical voltage to drive the water splitting reaction. Second, there is the "catalyst branch" which focuses on the development of efficient dark catalyst for either hydrogen or oxygen evolution. Third, there are "theoretical calculations and model systems" to gain insight into the water splitting process at an atomistic level.

The topics investigated in this thesis rank between the first and the second branch. In detail, the photovoltaic tandem cells consisting of two stacked, amorphous silicon p-i-n structures, were produced by the Forschungszentrum Jülich. These cells have a tunable voltage range from 1.4 to 1.6 volts. As a next step, these cells must be modified by depositing an appropriate buffer layer that protects the cell from the electrolyte while maintaining a good electrical contact. As a last step the cells were finalized by the deposition of a catalyst. These two last steps are of interest in this thesis. Given the limitations of the tandem cell, the duty is to find well adhering, efficient catalysts while avoiding the introduction of additional voltage losses, either in the cell or in the buffer layer [8].

As these cells are complicated to be produced, most experiments were modeled on crystalline silicon. The tandem cells n-type boundary is oriented towards the electrolyte, hence acting as a cathode for the hydrogen evolution reaction (HER). Consequently, n-type silicon was used as the model system. In contrast to the tandem cell which is terminated with a n^+-layer, low doped silicon was used, as it is more sensitive to changes occurring on the surface.

Part of this development is also the optimization of existing catalysts. A recent review by Vesborg et al. emphasizes that despite several improvements, platinum itself and platinum derived alloys are still the best catalysts for the HER [9]. Moreover, model calculations revealed that todays platinum production is sufficient to support a transition to platinum based water splitting devices even on a global scale [10]. The secret to the special activity of platinum lies in its bond strength to the hydrogen atom. A nice overview of the work already invested in the hydrogen-platinum interaction is given by the review article from Climent in 2011 [11].

It is assumed that hydrogen adsorption on the surface is an important intermediate step to provide the further reaction to H_2, in accordance with Sabatier's principle [12]. Two theories have emerged which formulate the overall reaction mechanism, the Volmer-Tafel (1.1) and the Volmer-Heyrovsky (1.2) mechanisms.

$$\begin{aligned} 2H^+ + 2e^- &\longleftrightarrow 2H_{ads} && \text{Volmer step} \\ 2H_{ads} &\longleftrightarrow H_2 && \text{Tafel step} \end{aligned} \tag{1.1}$$

$$\begin{aligned} H^+ + e^- &\longleftrightarrow H_{ads} && \text{Volmer step} \\ H_{ads} + H^+ + e^- &\longleftrightarrow H_2 && \text{Heyrovsky step} \end{aligned} \tag{1.2}$$

Both have the Volmer step in common, which describes the adsorption of one proton to the electrode surface. Due to an electron transfer from the metal to the proton this process is associated with an electrical current. The mechanisms deviate in the second step. Whereas the Tafel step describes the reaction of two adsorbed hydrogen atoms to molecular hydrogen, the Heyrovsky step continues the reaction by utilizing a proton from the solution. Thus, in contrast to the Volmer and Heyrovsky step, the Tafel step is currentless. This in return means, that the Tafel step is independent of potential, because no charges are transfered. Vilekar et al. exploited this difference of the mechanisms by impedance spectroscopy [13]. They were able to show that in alkaline solutions for low overpotentials the Volmer-Tafel mechanism, whereas at higher potentials the Volmer-Heyrowsky is dominating. The primary Volmer adsorption step is never limiting the reaction rate in the investigated potential range. This result resonates well with the general Butler-Volmer theory. Although Butler-Volmer assumes a direct charge transfer from the electrode to the electrolyte and is not applicable to the HER directly, the theory can qualitatively explain these result. Since the Tafel step does not change with potential it is no surprise that at some point it is overtaken by the potential dependent Heyrovsky step. However, both steps require adsorbed hydrogen at the surface and thus must also be dependent on the strength of the metal-hydrogen (M-H) bond.

This correlation was first studied by Trasatti et al. who clearly showed the correlation between exchange current density and the metal-hydrogen bond strength in a *volcano plot* [14, 15]. The reasoning is that a sufficiently high bond strength is required in order to have a sufficient surface coverage with adsorbed hydrogen. A fact that is generally true for transition metals. At the same time, the bond strength must not be too high, so it does not hinder the release of hydrogen. For sp-metals the enthalpy of the reductive adsorption of the proton is typically positive, thus making the Volmer step rate determining. These conclusions drawn from experimental data were later confirmed by work from Hammer et al. [16]. By employing density functional theory (DFT) calculations they were able to directly monitor the formation of the bonding and anti-bonding states of the adsorbed hydrogen. Thus, they showed that for transition metals primarily the d-electrons are involved in the bonding mechanism. The energetic position of the adsorbed hydrogen bonding orbital is therefore a direct consequence of the energetic position of the electronic states of water and the metal. In figure 1.1 the d-band, as well as the Fermi level is depicted for the first series of transition metals [17]. Especially metals on the right side with almost filled d-bands show a good activity for the HER.

In this context it is important to differentiate between the adsorbed hydrogen that is a necessity for the evolution of hydrogen gas, and the commonly "under potential deposited" hydrogen (H_{upd}) that is easily accessible via cyclic-

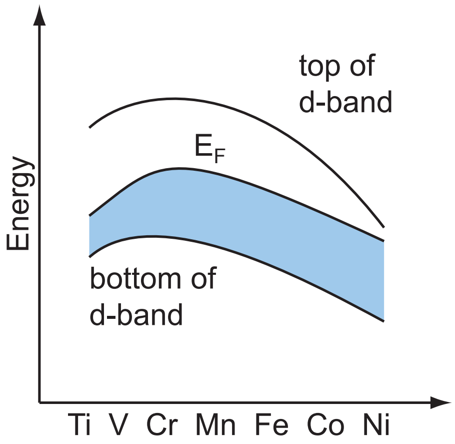

Figure 1.1.: Schematic illustration of the top and bottom of the d-band and the Fermi level. Adopted from [17].

voltammtry [18–20]. These hydrogen atoms are rather strongly and statically bound, thus passivating the surface [21]. It is assumed that the important reactive species for the HER is in fact a weakly bound multilayer hydrogen adsorbate formed at higher potentials, hence its designation is H_{opd} (over potential deposited) [18]. A recent DFT calculation by Roman et al. confirmed this assumption when they observed a direct proton transfer from weaker bound adsorbed hydrogen species into the electrolyte [22]. Still the overall governing relationship to the relative energetic position of the water and metal d-states remains valid. As a consequence it was now possible to directly correlate the electronic structure to the catalytic activity. A useful descriptor in this context is the introduction of the d-bands "center of gravity". The complex structure of the d-band is therefore simplified by only considering its center [23–25]. Based on this research, Jaksic presented a more comprehensive article investigating the general volcano relationships concerning the HER [26]. Here the periodic nature of the catalytic activity in dependence on the atomic number becomes evident. As the electron configurations are repeated within the periodic system, the catalytic activity scales accordingly.

Best activities for the HER are achieved for all metals with d^8-configurations, e.g. platinum and palladium are good HER catalysts. They all feature two holes in the d-shell which would also be required when considering the Volmer-Heyrovsky mechanism to occur at one site [27]. The underlying assumption for the development of better catalyst materials therefore relies on tuning of the metal hydrogen bond strength. Since it is a function of the position of the d-states, two approaches are thought to improve the catalysis:

1. By alloying appropriate metals.
2. By changing the size of the catalyst.

The alloying approach is rather evident. By combining a set of metals a resulting alloy might be obtained that shows an ideal d-level configuration and as a result an optimized H-surface bond strength. Examples for this approach are numerous [28–32]. For these types of catalysts it is also typically intended to synthesize small particles, simply because they exhibit a high surface to volume ratio. Consequently, an improved specific activity can be achieved. This is especially important considering the high cost of the typical noble metal catalysts e.g. platinum, palladium, ruthenium and iridium.

The second approach to increase efficiency is the reduction of the size of the catalyst. The idea behind it goes beyond the classical understanding derived from the surface to volume ratio. If the size shrinks below approximately 5 nm, quantum effects start to emerge. A prominent example is the use of quantum dots in semiconductor devices like lasers where they show discrete, confined electronic states [33]. The same effect is true for metals as well. When the particle grows in size starting from the atom, its electronic structure starts to change until it reaches the typical band structure observed for a bulk material.

The progressive change in the valence band when increasing the cluster size has also a pronounced effect on the aforementioned d-band center. In 2011 Toyoda et al. were able to directly link the position of the d-band center of platinum clusters to the catalytic activity for the oxygen reduction reaction [34]. Further experiments were able to determine specific cluster sizes, that show especially high catalytic activities. A simple reaction to probe in this context is the oxidation of CO to CO_2 in the presence of oxygen [35]. In 2009 Kaden et al. were able to directly correlate the Pd 3d binding energy measured by X-ray photoelectron spectroscopy (XPS) to the catalytic activity of the Pd-particles [36]. Later Watanabe et al. found the Pt_7 cluster to have a extraordinary high activity [37]. However, the reason in this case was not the specific electronic structure of this cluster, but a shape transition occurring for Pt_7. Due to the formation of a second layer and the associated drop in active sites, the activity decreased when going from Pt_7 to Pt_8. In contrast to this, it is often found for the HER, that the specific activity decreases as the particles get smaller [38]. However, only recently Schweinberger et al. published results for the hydrogen evolution on platinum clusters supported by CdS nanorods [39]. Upon illumination they showed a good water splitting activity. Here a maximum in activity was found for Pt_{46} clusters. The argument brought forward for this enhanced activity relies on the assumption that the highest occupied molecular orbital (HOMO) of the cluster is located in-between the conduction band of the semiconductor and the hydrogen redox level. Unfortunately spectroscopic evidence of this fact is not available. Contrastingly, in a simultaneous publication by Nesselberger, it was found that in fact not the cluster size itself but the induced electric field between those clusters is responsible for the enlarged activity [40].

The limited size of the small particles gives rise to another interesting effect. Due to their small size the clusters deposited on the surface are not able to completely screen the electronic interaction with their support. Therefore, the occupation of valence band states changes simply by varying the support material. In 2012 Bruix et al. found an excellent HER activity for Pt_8 cluster deposited on CeO_2 [41]. They attributed this remarkable efficiency to the small clusters ability to rearrange itself electronically as well as geometrically, making the dissociation of water strongly exothermic.

In this thesis also several experiments with clusters consisting of only a few atoms are presented. However, due to the limited supply of these clusters, only a few, mainly photo electron spectroscopy (PES) experiments, are presented. The important aspect in this context is the interaction of confined clusters with the substrate material. The "pinch off" effect originally observed by Nakato et al. in 1985 of gold particles on TiO_2 is probably the most popular example [42]. By the immersion into the electrolyte the electric field of the cluster that typically leaks into the semiconductor is completely pinched off, thus leaving the Fermi level of the cluster floating with respect to the substrate.

In order to investigate these surface and interface processes, several electrochemical and photoelectron spectroscopy measurements were conducted. Starting with well defined surfaces, i.e. single crystalline platinum or silicon, and down to single atoms, the interplay between electrolyte, support and catalyst were investigated in a rigorous manner.

2 Theoretical background

Three interfaces of a photoelectric conversion device are investigated within this thesis. In figure 2.1 the interfaces of interest are schematically depicted. The first between support and protective layer (in blue) is a simple solid state contact and is therefore also accessible by well established methods. The second contact is formed between the catalyst and the protective layer (red). This is also a solid state contact, however its contact properties are complicated by the fact that the small size of the cluster leads to a size-dependent electronic structure. The third interface is formed between the electrolyte and the catalyst and support simultaneously (green). The energetic alignment between catalyst and electrolyte is important for the catalysis process. It is also influenced by the interface between electrolyte and protective layer. The emergence of a crosstalk between these interfaces upon immersing them into the electrolyte is of special interest and basically requires in situ measurements.

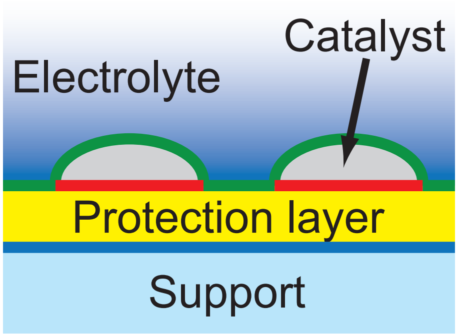

Figure 2.1.: Schematic illustration of the interfaces of interest: In green: Interfaces between the electrolyte and the protective layer and the respective catalyst. In red the interface between catalyst and the protective layer is shown, and in blue the interface between the protective layer and the support is displayed.

In the following the theoretical background for each of these interfaces will be briefly discussed. The fundamental quantity that underlies each investigation is the energetic alignment of the electronic states between two phases across their common interface, i.e. their band alignment.

2.1 Solid state contact

The qualitative shape of a solid state contacts depends on the class of material which forms the interface. A detailed discussion and derivation of the origin of these contacts can be found in the standard work from Sze [43]. The important properties are the energetic position of the Fermi level and the charge carrier density within each material that govern the shape of the contact.

As two materials are brought in contact their respective Fermi level align by transferring electrons across the interface, i.e. an electrochemical equilibrium is formed. The shape of the electric potential across such an interface is now governed by the definition of the electric field $\vec{E}$, eq. 2.1 and Gauss' law, eq. 2.2. Hereby ϕ denotes the electric potential, ρ the charge carrier density, ϵ the permittivity and $\vec{E}$ the electric field.

$$\vec{E} = -\nabla\phi \tag{2.1}$$

$$\nabla \cdot \vec{E} = \frac{\rho}{\epsilon} \tag{2.2}$$

The band alignment will differ depending on the type of material. In figure 2.2 the contact formations between two metals (M), a metal and a n- and p-type semiconductor (SC) and a metal and an insulator (INS) are depicted.

The dominant processes are described in the following.

Two metals: Due to the high charge carrier density of free electrons in metals any penetration of a electric field

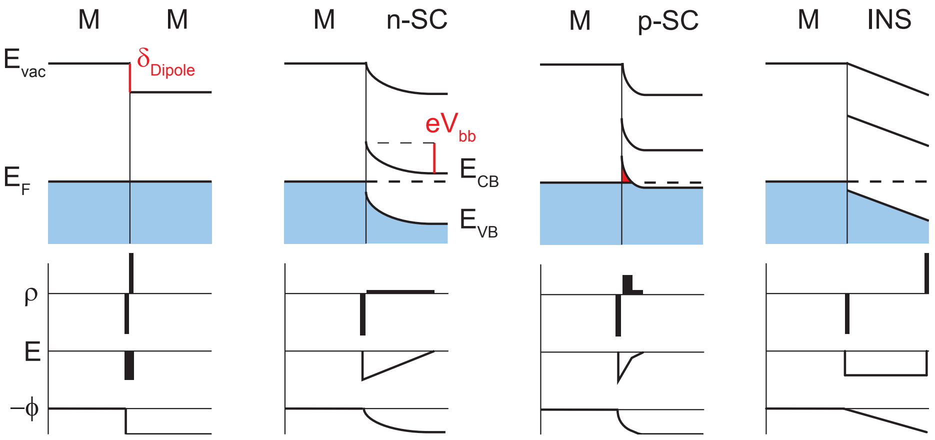

Figure 2.2.: Contact formation between solids. A metal (M) forms a contact with another metal (M), a n-type semiconductor (n-SC), a p-type semiconductor (p-SC) and an insulator. Workfunctions are chosen in such a way, that the WF of the metal (M) is higher than the other contact material.

is directly shielded at the surface by forming an interface dipole δ_{Dipole}. Thus, in the metal there is no electric field and the electric potential ϕ is constant (flat).

Metal and n-SC: Semiconductors have a finite amount of free charge carriers which can be influenced by doping. In the depicted case n-doping leads to an increase of electrons in the valence band. In contact to the metal, electrons are transfered from the SC into the metal. In the Schottky model, they leave charged species, i.e. the dopants, behind, leading to a constant charge carrier density. Assuming this finite constant charge carrier density one arrives at a parabolic dependence for the electric potential within the semiconductor. The charge in the metal and in the so called space charge region of the semiconductor cancel each other. Depending on the majority charge carrier and work functions, a depletion region (as depicted) or an accumulation region can be formed at the surface. In general this effect is called "band bending", as it is a result of the parabolic curvature of conduction (CB) and valence band (VB). Its magnitude is described by $\mathrm{eV}_{\mathrm{bb}}$. The width of the space charge region W can be derived if the doping concentration N_D is known (eq. 2.3, with e being the elementary charge).

$$W = \sqrt{\frac{2\epsilon V_{bb}}{eN_D}} \tag{2.3}$$

Metal and p-SC: In this case the valence band is partially situated above the Fermi level. Thus, also states within the valence band are positively ionized. The high charge density leads to approximately an energy diagram observed for the two metals.

Metal and Insulator: The insulator has no free charge carriers and therefore no possibility to shield the electric field. Since the electric field is constant the electric potential shows a linear dependence.

Apart from the ideal band alignments in reality often Fermi level pinning due to the presence of surface states is encountered. These states form a localized surface charge with a distinct energetic position. A prominent example are the dangling bonds on silicon surfaces that form a midgap defect state. As a consequence the Fermi level is fixed at the surface and upon contact it does not show an ideal behavior.

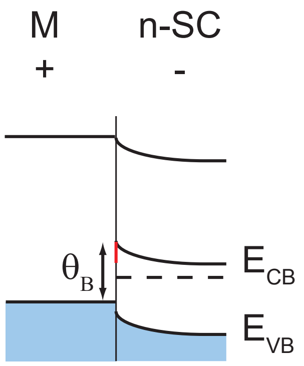

Figure 2.3.: Metal-SC contact under polarization. On the left forward bias and on the right reverse bias is shown. In red the barrier for electron transport is indicated. θ_B denotes the Schottky barrier height.

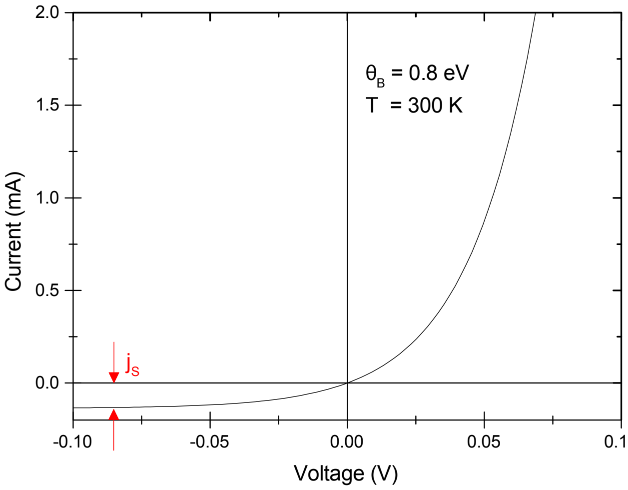

Figure 2.4.: Schottky-diode characteristic at 300 K and a barrier height of 800 meV.

2.1.1 Current transport across the interface

For insulators no current flow is possible as there are no free charge carriers for transport. Contrastingly, in metals the interface dipole is easily overcome by tunneling and usually a simple ohmic contact is observed dominated by their bulk resistance. The charge transport across the semiconductor metal interface is not as simple and requires extra considerations.

From figure 2.2 two situations can be envisioned for the metal-SC interface, depending on the polarization of the interface. Polarizing the electrodes will shift the Fermi level of both sides in accordance with the applied voltage. This situation is depicted in figure 2.3.

If a negative potential is applied to the semiconductor the band bending and thus the barrier (in red) is reduced. This situation is called forward bias because with increasing voltage the barrier decreases and the current increases. The opposite trend is shown at the right. In the reversed bias, the electrons moving from the metal into the semiconductor always encounter the same barrier height. This barrier is also called the Schottky barrier θ_B and leads to a constant, saturated current density of j_S.

This asymmetry in barrier height leads to a rectifying current-voltage characteristic. Assuming that transport over this barrier is thermally activated, the diode equation can be derived (eq. 2.4).

$$\begin{aligned} j &= AT^2 \cdot e^{\theta_B/kT} \cdot \left(e^{eU/kT}-1\right) \\ &= j_S\left(e^{eU/kT}-1\right) \qquad (2.4) \\ \text{where} \quad j_S &= AT^2 \cdot e^{\theta_B/kT} \end{aligned}$$

Hereby A denotes Richardson's constant, T the temperature, θ_B the Schottky barrier height and U the bias potential. In figure 2.4 the current-voltage (jV) characteristic of a Schottky diode with 800 meV barrier height at room temperature is displayed.

The rectifying properties can be seen by the asymmetric jV-curve. Often the formation of these barriers is encountered and it is the goal of interface engineering to engineer these barriers to the needed value.

At the same time Fermi level pinning can be observed which leads to a constant band bending irrespective of the deposited metal. This is called the Bardeen limit and is in contrast to the Schottky limit, where the band bending is given by the difference in electronegativity between metal and semiconductor.

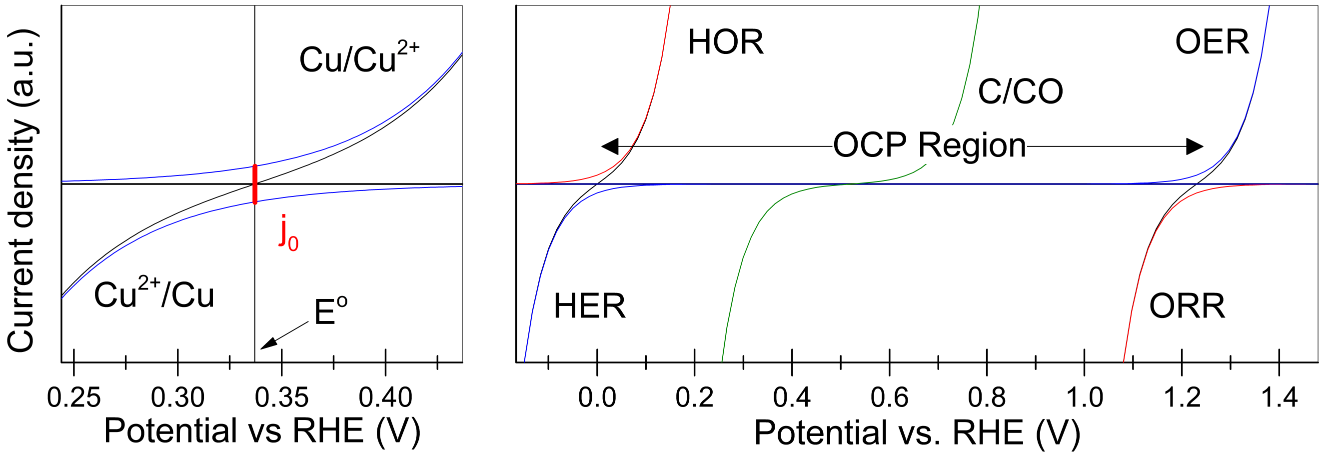

Figure 2.5.: Exemplary electrochemical polarization curves. Left: A well defined redox system like, Cu ⟷ Cu^{2+}. The exchange current j_0 is defined by a singular redox reaction leading to a precise standard potential. Right: Exemplary water splitting curves. Blue reactions are not limited by reactants, red curves lack sufficient reactants. In green the parasitic carbon reaction is shown.

2.2 Solid liquid contact

The first major difference to the solid state contact is that a contact to an electrolyte can – and mostly does – involve chemical reactions. The electrode itself can be part of the reaction or behave inert. Since the hydrogen evolution reaction is investigated and the electrode behaves as a heterogeneous catalyst, the electrode itself is inert with respect to the HER. In general these chemical reactions are sorted by their potential in the electrochemical series known from basic electrochemistry [44]. In this context the Nernst equation plays a central role 2.5:

$$E = E^o - \frac{RT}{zF} \cdot \ln Q \tag{2.5}$$

Hereby E is the cell potential and E^o is the standard potential for a cell reaction with reaction quotient Q. F is Faradays' constant and z the amount of transfered electrons during the reaction. By employing this equation the redox reactions can be placed on a potential scale. The important quantity is the standard potential E^o which is measured against the standard hydrogen electrode (SHE). According to IUPAC the recommended absolute electrode potential (against vacuum energy) for the SHE is 4.44 ± 0.02 V [45]. Using the relationship in equation 2.6 it is possible to relate the electrochemical redox reaction in solution to the band positions in the electrode.

$$E_{abs} = 4.44\ \mathrm{V} + E_{\mathrm{SHE}} \tag{2.6}$$

The band alignment of the electrode with the electrolyte is dependent on the specific redox reaction of interest. In the simple case with only one dominant reaction mechanism, e.g. Cu ⟷ Cu^{2+}, the band alignment between the reactive copper electrode and the solution can be calculated by the Nernst equation. This is somewhat analogous to the solid state contact, where only the electrochemical potential of electrons needs to be regarded. In this case only Cu^{2+} needs to be considered for the electron transfer, hence defining the electrochemical potential of the electrons in the solution.

If more than one electrochemical reaction take place on the surface the situation changes. In the case of water splitting both the hydrogen and the oxygen reaction could in general occur on the electrode surface. The electric potential between the platinum electrode and an arbitrary reference electrode is therefore a priori not known. In fact the equilibrium potential will depend on the reaction rates and concentrations of the corresponding species in the electrolyte.

The resulting band alignment with the electrode is therefore dominated by the reaction rates occurring at the surface. These reactions can be numerous and complicated and their rate constants are a priori unknown. A rather simple approximation of the reactions on inert surfaces was proposed by Butler and Volmer (Butler-Volmer equation, eq. 2.7) [46].

$$j = j_0 \cdot \left[\exp\left(\frac{\alpha z F \eta}{RT}\right) - \exp\left(-\frac{(1-\alpha) z F \eta}{RT}\right) \right] \tag{2.7}$$

In this context j_0 is the exchange current density, α is the charge transfer coefficient, F is Faradays constant and η the overvoltage. The Butler-Volmer equation has several restraints on its applicability. First, it assumes that the rate limiting step is the charge transfer from the electrode into the redox level. Secondly it is valid only for a one electron transfer processes and thirdly, it assumes a linear electric field within the Helmholtz plane.

In figure 2.5 both half cell reactions are plotted exemplary for the copper (left) and the platinum (right) system. The electric potential of the copper systems is well defined by Nernsts equation because it has a appreciable exchange current density for one redox reaction.

In contrast to this, the pure water splitting system has two possible reaction pathways, namely the reactions involving dissolved hydrogen and oxygen. Furthermore, the limited amount of dissolved oxygen or hydrogen in the platinum electrode case leads to small exchange currents and thus to an imprecise definition of the open circuit potential (OCP). This is indicated by the red curves (hydrogen oxidation reaction, HOR and oxygen reduction reaction, ORR) in the plot, as they can become negligible compared to the hydrogen evolution reaction (HER) and oxygen evolution reaction (OER) (blue curves).

The open circuit potential of a platinum electrode will therefore lie somewhere between 0 V and 1.23 V vs. RHE (reversible hydrogen electrode) in an aqueous solution. Outside of these ranges water would not be stable and basically split itself. This is complicated by the fact that contaminations, e.g. carbon will also exhibit an oxidative and reductive current (green), hence they are also influencing the OCP.

2.3 Clusters on support

Clusters deviate from the solid state contact because of their limited number of electrons. Whereas a bulk material will shield the interface and remain undisturbed sufficiently far from the surface, the cluster cannot do so. Additionally the chemical state of the cluster can be quite different from the bulk material. Due to the size dependent hybridization of bands the electronic occupation is dependent on the cluster size [47]. This is also the reason for the significantly increased chemical reactivity of small clusters. Three aspects might give rise to distinct changes in binding energy when comparing bulk materials with clusters.

Chemical reactivity: Due to their reactive nature a cluster might react with the substrate, although this reaction is naturally not observed for bulk materials. Especially on oxide substrates cluster are prone to also form an oxide [48, 49] or to form alloys with supporting metals.

Change in occupation: The lack of hybridization between electronic states in small clusters leads to a changed occupation. This has a direct influence on e.g. the d-band center. Furthermore the occupation can be changed by a charge transfer from the substrate to the cluster without necessarily forming a chemical bond [50–53].

Under-coordinated atoms: Even if no reaction with the substrate occurs, the high amount of under-coordinated bonds at the surface has an influence on the atomic and electronic structure [54].

All of these effects make the evaluation of the electronic alignment to the substrate more challenging. However,

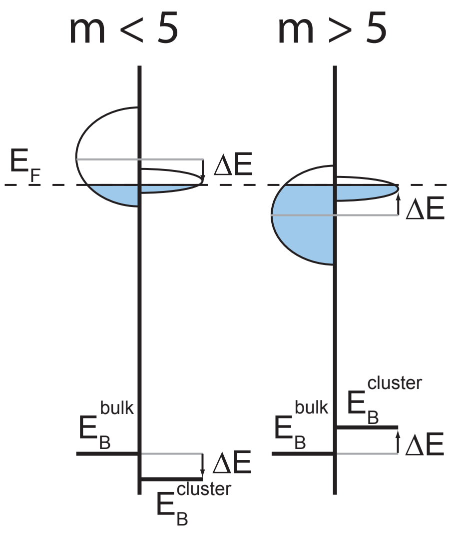

Figure 2.6.: Influence of d-orbital narrowing on the BE. Relative occupation for cluster and bulk are identical. However, narrowing leads to a positive shift in BE for m < 5 and a negative shift for m > 5. Adopted from [55].

even given the complexity, a general rule of thumb for transition metal clusters can be obtained from general considerations.

The measured binding energy (BE) is defined by the distance between the electrons level and the Fermi level. When the cluster get small the valence band density of states (DOS) will contract and consequently influence the BE, because the percentage of filled states relative to the number of available states, i.e. the relative occupation of the VB, must remain unchanged. For transition metals with more than half filled d-levels the BE will decrease compared to the bulk value, whereas for less than half filled shells the BE will increase. Figure 2.6 schematically exemplifies this effect.

As platinum has a more than half filled d-band ($m > 5$), a negative shift would be expected from these consideration. However, in the following experiments, a positive shift will be found for platinum, highlighting the fact that the substrate-cluster interaction also has a large effect on the electronic configuration and is not easily predictable.

3 Methodology

In the scope of this thesis surfaces were prepared by ultra-high vacuum (UHV) based thin film techniques, namely sputtering and electron beam evaporation. Characterization of these layers was done primarily by photoelectron spectroscopy (PES), in some cases also low energy electron diffraction (LEED) and scanning electron microscopy (SEM) were used. At the synchrotron BESSY II water can be directly adsorbed onto the surface of interest and directly investigated by synchrotron X-ray photoelectron spectroscopy (SXPS). To assess catalytic performance also electrochemical experiments were conducted.

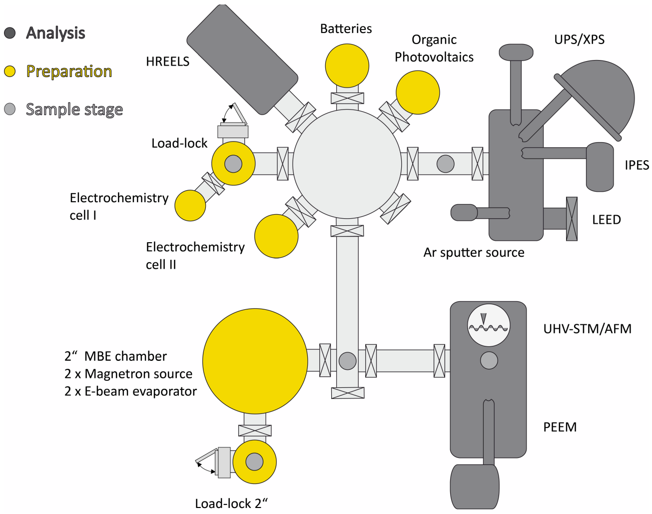

Figure 3.1.: Illustration of the DAISY-FUN laboratory comprising in yellow several preparation and in gray analysis chambers.

3.1 Thin film deposition

To deposit materials vacuum based techniques were employed. The typical background pressure in all ultra-high vacuum (UHV) systems was at least 10^{-8} mbar. In figure 3.1 a top view of the DArmstadt Integrated SYstem for FUNdamental research (DAISY-FUN) is shown. Sample preparation was done in the molecular beam epitaxy (MBE) chamber at the lower left corner. All systems are connected so that samples are never exposed to air.

For electron beam evaporation of platinum (99.9 % Alfa Aesar) a graphite crucible in an EFM2 evaporator from Omicron Nanotechnology GmbH was used. Given the high melting point of platinum (1772 °C) [56] deposition rates were low (0.25 Å/h), although the evaporator was operated close to its maximum capability of 300 W. The ion flux was typically adjusted to 250 nA by applying a 950 V acceleration voltage and an emission current of 270 mA.

For sputter deposition two MeiVac 2" MAK magnetron sputter sources are available. One was typically loaded with platinum (Pt 99.99 %, Scotech Ltd.), the other with either metallic titanium (Ti 99.995 %, Kurt J. Lesker Co.) or nickel (Ni 99.99 %, Kurt J. Lesker Co.). The chamber was additionally fitted with a heatable sample stage and a variety of gas inlets (O_2, N_2, Ar with a purity of 5N or better) controlled by MKS flow meters. During deposition the sample was rotated to ensure a homogeneous deposit.

3.2 Cluster synthesis

The clusters were synthesized by sputtering in a dedicated synthesis chamber. The setup was primarily operated by Stephan Krähling and Benjamin Elger. In figure 3.2 a schematic illustration of the setup is depicted. The target is eroded in a mixture of argon and helium in an aggregation tube (1) and cooled from outside with liquid nitrogen (LN_2). Here the clusters coalescence and leave the nucleation tube through a small pinhole. Their nucleation process is governed by temperature, pressure, sputter power and their dwell time in the nucleation tube [58]. Then, the cluster beam expands into vacuum. Here it enters a skim-

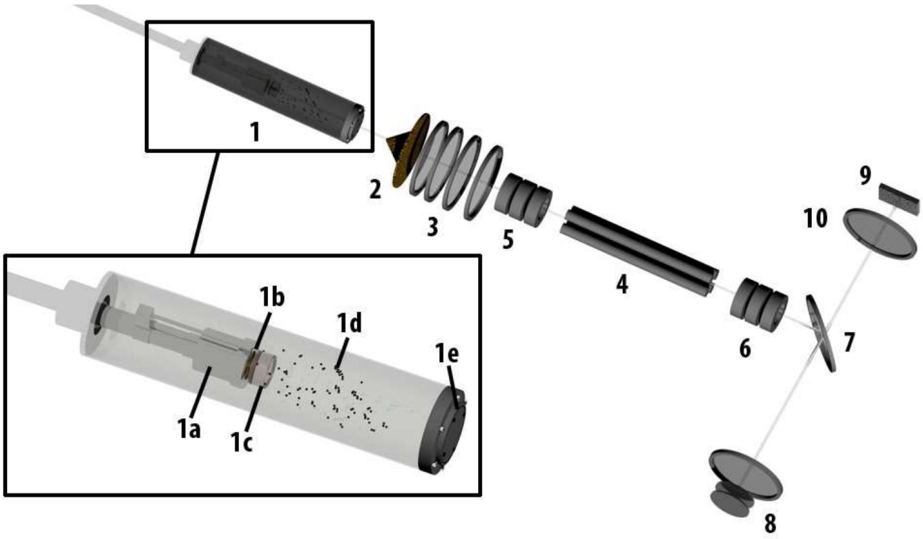

Figure 3.2.: Schematic drawing of the cluster synthesis setup. Aggregation tube (1), sputter head (1a), target (1b), plasma (1c), nucleating clusters (1d), pinhole (1e), skimmer (2), TOF-MS grids (3), quadrupole (4), Einzel lenses (5, 6), electrostatic mirror (7), MCP-detector (8), sample (9), retarding grid (10). Reproduced with permission from [57].

mer (2) to remove part of gaseous species. For mass selection either a time-of-flight (TOF-MS) (3) or a quadrupole mass spectrometer (QMS) (4) are available. At the beginning of the experiments the TOF-MS was used, however due to its discontinuous operation and high kinetic energies during deposition later on the QMS was employed. Via an electrostatic lens the charged clusters can be reflected onto the sample (9) for deposition or onto a multi-channel plate (8) for detection, separating them from all neutral ones.

To further increase the deposition rate the electrostatic lens was also replaced with a quadrupole bender. First experiments and operational parameters are reported in the master thesis of Benjamin Elger [57].

3.3 Photoelectron spectroscopy

Photoelectron spectroscopy (PES) is a viable tool to directly probe electronic properties of materials in surface near regions (< 5 nm) [59]. It relies on the photoelectric effect, namely the emission of electrons from the substrate material upon illumination with X-Rays (XPS) or ultraviolet light (UPS). At a synchrotron also tunable excitation energies are possible (SXPS). In the spectrometer the kinetic energy of the photoelectron is determined. Since the energy contained in the primary photon must be conserved, knowledge of the kinetic energy E_{kin} enables the calculation of the binding energy of the corresponding photoelectron (eq. 3.1).

$$h\nu = BE + E_{\text{kin}} \tag{3.1}$$

The binding energy (BE) itself is determined by the difference between the initial E_{initial} and the final state E_{final}, i.e. the ground state energy and the excited state after removal of the photoelectron including the added contribution of the remaining hole [60]. This theory holds for the "frozen" electron case, where no relaxation of other outer shell electrons is allowed. In reality relaxation $E_{\text{relaxation}}$ of the outer electrons will decrease the observed final state energy. This relationship is given in its simplified form in equation 3.2.

$$BE = E_{\text{final}} - E_{\text{initial}} - E_{\text{relaxation}} \tag{3.2}$$

For chemical analysis, the chemical shift ΔE_{bin} of a photoelectron line is of interest. In a first approximation the influence of the chemical environment changes the initial state energy, but not the final state energy or the relaxation process. Therefore, chemical shifts in general can be attributed and directly correlated to changes in the initial state ($\Delta E_{\text{bin}} = \Delta E_{\text{initial}}$). As a consequence typically an increase in binding energy is observed when the oxidation state increases.

However, there are cases where the final state has an impact on the measurement. For example, as a result of the final state effect, the Co 2p BEs are arranged in such a way that, Co^0 (778.2 eV) $<\text{Co}^{3+}$ (779.6 eV) $<\text{Co}^{2+}$ (780.5 eV). Whether the final state will have a significant impact on the BE is unknown a priori. However, metals usually exhibit a better screening of the remaining hole than ionic solids, due to their free electrons. Hence the final state contribution will mostly be smaller for metals. However, these extra-atomic, i.e. caused by surrounding atoms, relaxation effects become especially important for small clusters, which only have a limited number – or none – of neighboring atoms.

To ease the interpretation of photoelectron spectra of clusters it is advisable to compare the measured BE to the one obtained for the bulk material. Equation 3.2 is therefore modified. Since, $\text{E}_{\text{relaxation}}$ is not separable from E_{final} as they are both dependent on the electron configuration after hole formation, they are combined in a joined $\Delta\text{E}_{\text{final}}$. To interpret changes in relation to bulk material the new form is given in equation 3.4.

$$\begin{aligned}\Delta E_{\text{bin}} &= E_{\text{bin}}(\text{cluster}) - E_{\text{bin}}(\text{bulk}) \\ &= \Delta E_{\text{initial}} + \Delta E_{\text{final}} \qquad (3.3)\end{aligned}$$

The basic assumption is, that the change in BE can be approximated by a simple addition of a change in initial (chemical) state energy $\Delta E_{\text{initial}}$ and a finale state contribution ΔE_{final}. In the even more simplified case ΔE_{final} is simply zero, meaning that the chemical shift is equal to the change in the initial state.

The most pronounced initial state effect of a small supported cluster results from of its high surface to volume ratio. The chemical environment for a small cluster is different from its bulk counterpart. It will strongly depend on whether or not the cluster hybridizes with the support material and if there is an associated charge transfer from the cluster to the support or vice versa. Initial state effects will strongly depend on the materials chosen for the cluster and for the support.

In contrast, the explanation of the final state effects is not as straight forward because they are strongly interdependent and cannot be measured separately from each other. Already in 1988 Wertheim gave a comprehensive review of the BE shifts observed in PES of small supported clusters [61].

The most obvious final state contribution comes from the remaining charge of the core hole. After photoemission the cluster will act as a positively charged sphere and hence contribute its Coulomb potential to the measured BE. If the cluster is deposited on a metallic substrate the Coulomb contribution will be reduced, because the core hole of the cluster will be immediately filled by electrons from the support.

Furthermore, the size of the cluster will change its band structure, compared to the bulk material. This in itself is still an initial state effect, but it may have an impact on the final state as well. A decreased DOS at the Fermi level will reduce the shielding of the core hole and consequently increase the final state energy, i.e. the measured BE is also increased. Since small clusters usually exhibit a reduced DOS at the Fermi level, they show a positive BE shift compared to the bulk value.

As was already mentioned, for large clusters and thicker layers the final state contributions can be usually neglected and changes in BE are directly correlated to the initial state, i.e. the chemical environment.

The experimental setup consisted of a Phoibos 150 semi-hemispherical analyzer from SPECS. For the excitation of photoelectrons different sources were employed: X-rays from an $\text{Al}_{K\alpha}$ anode (XPS) (XR 50), ultraviolet light from a helium discharge lamp (UPS) and synchrotron irradiation at BESSY II (SXPS).

A comprehensive introduction to photoelectron spectroscopy can be found in the work from Briggs and Seah [59]. What is especially important in this thesis is the determination of the thickness and stoichiometry of thin films by XPS. For thin films some adjustments must be made in order to receive meaningful results from XPS. The problem originates from the fact that the thin film signal is weighted against the infinitely thick substrate, thereby overestimating the overlayer contribution. It becomes even more difficult for stoichiometry determination if signals with deviating kinetic energies are compared. In the following the adjustments that must be made will be derived from general considerations first for the homogeneous case and later for thin films.

3.3.1 Stoichiometry determination by XPS

The differential intensity *dI* of a photoelectron line, originating from a thin slice of infinitesimal thickness *dx* is given by equation 3.4 [62]. Photoelectron diffraction, that give rise to a spatial diffraction pattern and thus an angle dependence of the electron emission, is disregarded in this case.

$$dI_i = JK\sigma(E,i)L(E,i)T(E)n_i(x)\exp(-x/\lambda(E))\,dx \tag{3.4}$$

Hereby J is the flux density of the excitation source, K is a proportionality factor (e.g. probed sample area, spot size), σ and L are the atomic cross section and asymmetry parameter respectively, and T is the analyzers transmission function. A lowercase i indicates that the parameter is also dependent on the element i that is being investigated. The atomic density of the element i is described by $n_i(x)$, not necessarily being a constant throughout the sample. The last exponential describes the damping of photoelectrons due to Lambert Beer's law with the damping constant λ that is dependent on the chemical composition of the matrix. To describe this damping effect the inelastic mean free path (IMFP) is used. It describes the mean distance a photoelectron can travel before inelastic scattering occurs. A rough estimation of the IMFP is possible from the "universal curve" for solids described by Seah et al. reproduced in figure 3.3 [63]. Typically it is assumed that a sample is homogeneous, i.e. $n_i(x) = \text{constant}$. The intensity dependence can then be derived by integrating *dx* from zero to infinity. Additionally the constant factors K, L and σ can be combined in a element specific sensitivity factor S_i. It follows equation 3.5, which describes the signal intensity I_i^h for a species i in the homogeneous composition case (hence the superscript h).

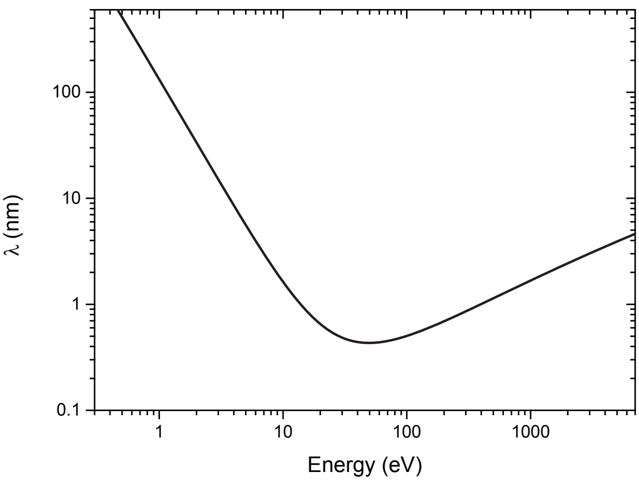

Figure 3.3.: Dependence of the IMFP (λ) on the kinetic energy of the photoelectron. Adopted from [63].

$$\begin{aligned} I_i^h &= \int_0^\infty JTS_i n_i \exp(-x/\lambda(E))\,dx \\ &= JTS_i n_i \lambda \end{aligned} \tag{3.5}$$

In the homogeneous case the atomic density of elements can be derived if the transmission function T, the atomic sensitivity factor S_i and the IMFP λ is known. The transmission function is known and supplied with the spectrometer. Values for S_i can be found in literature [64, 65], while in our case they were also supplied by the manufacturer. The sample composition can therefore by derived by equation 3.6, assuming a homogeneous composition.

$$x_i = \frac{n_i}{n_{total}} = \frac{I_i^h/(S_i T\lambda)}{\sum_i I_i^h/(ST\lambda)} \tag{3.6}$$

Equation 3.6 is also implemented in the dedicated XPS software CasaXPS for automated evaluation, further information can be found in the handbook [66]. The evaluation becomes more complicated as soon as the sample is not homogeneous. An often encountered system for example consist of stacked layers.

In this case the integration for the overlayer goes from zero to a thickness t, whereas the substrate starts at t and goes to infinity. For the atomic distribution $n_i(x)$ a step function is assumed, hence there is no overlayer material found in the substrate. Since there are only two unknowns, t and n_i, knowing one of them enables the calculation of the other one. Integrating equation 3.4 for a layer with finite thickness yields the following relationship for the intensity of the overlayer (eq. 3.7).

$$\begin{aligned} I_i^o &= \int_0^t JTS_i n_i \exp(-x/\lambda(E))\,dx \\ &= JTS_i n_i \lambda (1-\exp(-t/\lambda(E))) \\ &= I_i^h (1-\exp(-t/\lambda(E))) \end{aligned} \tag{3.7}$$

Here I_i^h denotes the homogeneous case (eq. 3.5). For the substrate also a correction is necessary, due to the damping of its signal. Integration of equation 3.4 from thickness t to infinity yields equation 3.8

$$\begin{aligned} I_i^s &= JTS_i n_i \lambda \exp(-t/\lambda(E)) \\ &= I_i^h \exp(-t/\lambda(E)) \end{aligned} \tag{3.8}$$

Correcting the respective signals by these factors the stoichiometry can also be obtained for thin films or for signals that are damped by an overlayer. What they all have as a common requirement is a precise knowledge of thickness or IMFP λ. By knowing either value the thickness t or the stoichiometry can be obtained.

3.3.2 Film thickness determination by XPS

The easiest way to determine the thickness of an overlayer is to monitor the absolute damping of the substrate signal. This is already basically described by equation 3.8. However for this measurement it is necessary that the intensity of photoelectrons of a blank sample is known and that the nominal flux J is steady during all the measurements. Since alignment in the XPS machine is usually not very reproducible, this process is error-prone. A much more reliable thickness can be derived from monitoring relative intensity ratios between substrate and overlayer. For the thickness dependent intensity of the overlayer equation 3.7 and for the substrate equation 3.8 were already derived. Now, a signal I_s unambiguously originating from the substrate and I_o from the overlayer are compared.

$$\begin{aligned} I_o &= JT(E_o)S_o\lambda_o n_o (1-\exp(-t/\lambda(E_o))) &(3.9)\\ &= I_o^h (1-\exp(-\lambda(E_o)/t)) \\ I_s &= JT(E_s)S_s\lambda_s n_s \exp(-t/\lambda(E_s)) &(3.10)\\ &= I_s^h \exp(-\lambda(E_s)/t) \end{aligned}$$

The atomic density of overlayer n_o and substrate n_s as well as precise values for the IMFPs must be known, to determine the film thickness. In general, this equation set cannot be solved analytically for the thickness of the film, but instead must be solved numerically. However, if the photoemission lines from the overlayer and the substrate are close by, i.e. their deviation in the IMFP $\lambda(E)$ is small, the equation set can be simplified and solved for the thickness t (eq. 3.11).

$$t = \lambda \cdot \ln\left(1 + \frac{I_o \cdot T(E_s) n_s S_s}{I_s \cdot T(E_o) n_o S_o}\right) \tag{3.11}$$

Here the atomic density of the overlayer and substrate must be put in as known parameters. In table 3.1 the atomic densities of several compounds are listed. In any case the result depends significantly on the IMFP λ. Here

Table 3.1.: Parameters used for quantification [56]

Material	Density [g/cm³]	Molar mass [g/mol]	Atomic density [mol/cm³]
Pt	21.45	195.1	0.110
Ag	10.49	107.9	0.097
Si	2.34	28.1	0.083
SiO_2	2.32	60.1	0.039
TiO_2	3.84	79.9	0.048
NiO	6.72	74.69	0.090

more reliable values than the rough estimation from the universal curve are necessary. Very accurate values for the IMFP can be found in the NIST IMFP Database [67] or from predictive formulas also integrated in the databases software [68]. The IMFPs of relevant photoelectron lines in several matrix materials are listed in table 3.2.

3.3.3 Band diagram derivation

An important indicator to judge charge transfer across interfaces is the band alignment across such an interface. The lineup can be derived from XPS interface experiments, in which the energetics of core levels are monitored during the stepwise deposition of the second contact material onto the substrate [69].

From the blank substrate the valence band offset (VBO), i.e. $E_F - E_{VB}$, and core level binding energies can be measured. Upon starting the stepwise deposition of the contact material, a shift in core level energies can be observed, if band bending or a chemical reaction occurs. The VBO becomes difficult to monitor during such an experiment because it is a superposition of the DOS of both layers. In the case of band bending the energetic position of the surface Fermi level is changed, consequently the shift in all core level BEs compared to the bulk values are identical. If chemical interface reactions take place, the chemical environments of the interfacial atoms are rearranged, thus non-identical shifts of core levels can be observed. In the case of band bending, the change in the VBO in the substrate is assumed to be identical to the change in core level BEs originating from the substrate. Hence, the movement of the valence band, albeit being not unequivocally traceable, can be extrapolated from the core line shifts. When the final overlayer is completed the VBO of the overlayer can be deduced, because the substrate signal is completely damped.

Table 3.2.: IMFP values of a PES Line with kinetic energy $E_{kin}(L)$ (approximated) in a matrix. Values relevant for excitation with Al K_α.

Line	E_{kin} [eV]	Matrix	IMFP [Å]
Pt 4f	1415	Pt	16.2
Si 2p	1387	Pt	16.0
Ag 3d	1119	Pt	13.6
Ti 2p	1028	Pt	12.9
Si 2p	1387	SiO_2	37.7
O 1s	954	SiO_2	28.3
Si 2p	1387	TiO_2	27.3
Ti 2p	1028	TiO_2	21.7
O 1s	954	TiO_2	20.5
Si 2p	1387	NiO	23.7
O 1s	954	NiO	17.8
Ni 2p	633	NiO	13.2

To complete the band diagram, knowledge of the band gap (E_G) of both materials (if applicable) is necessary. Knowing the band gap the conduction band edge can derived by simply offsetting the valence band by E_G.

3.3.4 Water adsorption

For water adsorption experiments samples were transfered under UHV conditions to the synchrotron at BESSY II. A description and the functionality of the UHV transport chamber can be found in chapter 10. The samples were transfered into the Solid Liquid Analysis System (SoLiAS) at BESSY II without breaking the vacuum. For adsorption experiments the sample was cooled by liquid nitrogen (LN_2)

to cryogenic temperatures. The cooled manipulator connects an adsorption chamber with the XPS measurement chamber. The cooled sample was moved into the adsorption chamber and exposed to water vapor. Water was introduced through a leaking valve. The dosage was controlled by the exposure time and the pressure, monitored with a hot-cathode pressure gauge. Afterwards the valve connecting the XPS and adsorption chamber was opened and the sample directly moved to the measurement position.

To measure the sample after desorption, it was removed from the cooled manipulator. Subsequently it was moved to a transfer slide, at room temperature. The sample reached room temperature within a few minutes combined with a strong pressure surge due to the desorption of water. Afterwards the sample was again inserted into the cooled manipulator and measured.

At BESSY II the excitation energy can be adjusted from 86 eV to 1890 eV with a peak intensity at 700 eV. By adjusting the excitation energy, the depth resolution can be tuned from a surface sensitive to a more bulk sensitive measurement (see figure 3.3).

3.4 Electrochemical characterization

For electrochemical characterization a dedicated in situ electrochemical cell was used, which is described in detail in chapter 10.2. As a potentiostat a PalmSens^2 was used with a current range of ±10 mA. Only at the end of the experiments a new potentiostat (PalmSens^3) was acquired, that now also supports impedance spectroscopy.

Experiments were conducted in the 3-electrode setup as schematically illustrated in figure 3.4. The potential is measured relative to a reference electrode (RE) located in close proximity to the working electrode (WE) to minimize ohmic losses. The current passes through the counter electrode (CE), making it possible to investigate the half cell reaction at the working electrode without the interference of the counter reaction taking place at the counter electrode.

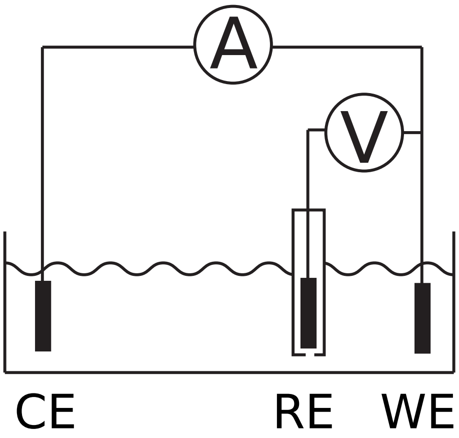

Figure 3.4.: Schematic of the 3-electrode setup. Current runs through the counter (CE) and working electrode (WE), while the potential is measured between WE and a reference electrode (RE).

The samples were measured in a three electrode setup, first with a 3 M NaCl Ag/AgCl (0.205 V vs. SHE), later with a 1 M KOH Hg/HgO (0.100 V vs. SHE) reference electrode. The reference electrode was switched because it was noticed that strong alkaline solutions (1 M KOH or NaOH) lead to a swelling of the glass frit. At first this lead to slight drifts in the measured potential, until later the frit was completely closed. To prevent this, the reference electrode was switched to Hg/HgO.

Photoelectrochemical measurements were conducted in a Zahner PECC-2 electrochemical cell and a Zahner Zennium potentiostat, both from Zahner-Elektrik GmbH. The AM1.5 (Air Mass 1.5) spectrum was produced by a solar simulator model #81150 from LOT-QuantumDesign.

3.4.1 Electrochemically active surface area

At first the electrochemically active surface area (ECAS) of the crystals was determined by hydrogen ad- and desorption experiments. For that purpose cyclic voltammetry (CV) was used in the potential range from 50 to 1050 V vs. RHE (Reversible hydrogen electrode) with a scan rate of 100 mV/s. As a result of the already mentioned electrode instability, the potential regime had to be adjusted occasionally.

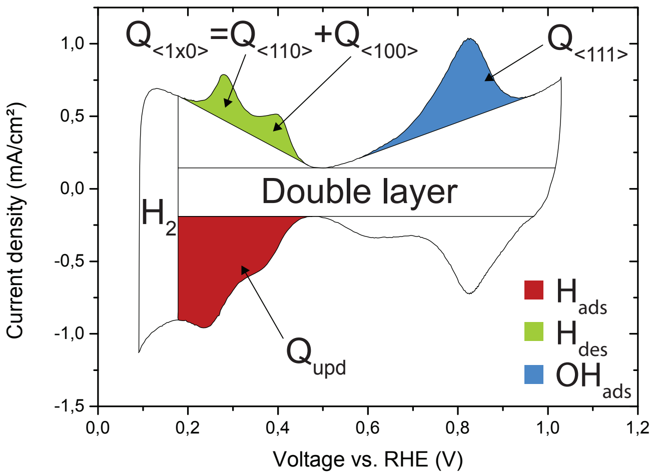

Figure 3.5.: Cyclovoltamogramm of polycrystalline platinum. The active surface area was determined by integrating Q_{upd}. Amounts of (100) and (110) facets were determined by integrating hydrogen desorption, and by integrating hydroxide adsorption for (111).

In figure 3.5 a typical CV cycle is shown for a polycrystalline sample. The electrochemically active surface area was determined by the non-specific hydrogen under potential deposition (Q_{upd}) as indicated by the red area. It is integrated from the onset of hydrogen adsorption until hydrogen starts to evolve from the solution. Its integral value is equivalent to the hydrogen desorption, i.e. integrating the anodic current, however the HER onset gives a clear boundary for the integration. For this reason the hydrogen adsorption was used [70]. In order to convert the obtained integral value of dimension [mA/cm²·V] to the surface charge density of adsorbed hydrogen, it must further be divided by the scan rate of typically 100 mV/s yielding the surface charge density in [μC/cm²]. The constant double layer capacitance is removed from the area. Measured values for Q_{upd} of platinum surfaces are 210 μC/cm² or 220 μC/cm² in 0.5 M H_2SO_4 and 145 μC/cm² in 1 M KOH, independent of the surface morphology [71–73].

As an indication for the amount of facets present also site specific peaks were integrated. The <100> and <110> orientations are jointly integrated because they tend to overlap (green area). A linear background was used in order to separate the unspecific hydrogen desorption from the site specific one. The <111> planes do not show a specific hydrogen peak, nevertheless they show a pronounced hydroxide adsorption as highlighted by the blue area. Again, a linear background was fitted in order to only include the site specific OH adsorption.

4 Silicon substrate preparation

Throughout this thesis a variety of different substrates was used. This includes hydrogen passivated silicon (Si:H), silicon passivated with SiO_2, indium tin oxide (ITO), titanium and highly oriented pyrolytic graphite (HOPG). For ITO, HOPG and titanum no elaborate sample preparation was necessary, therefore their preparation will be described shortly in the corresponding chapters. In contrast, silicon posed a challenge. The preparation of the Si wafers and the application of an appropriate surface passivation will be discussed in the following chapter.

4.1 Hydrogen terminated silicon

The silicon wafers were bought from ChrysTec and are diced into a size of 1x1 cm^2 with a thickness of 500 μm. The wafers are phosphorous n-doped and show a specific resistivity of 6.5 Ωcm. Given this resistivity the doping concentration N_D can be calculated in accordance to the SEMI Norm MF723-0307E [74] to be roughly $7 \cdot 10^{14}$ cm^{-3}. This already highlights the fact that the sample is a lightly doped semiconductor which can easily be influenced by surface defects. In table 4.1 general physical parameter for silicon are listed. The conduction band density of states of silicon is $N_C = 2.8 \cdot 10^{19}$ cm^{-3}. Using equation 4.1 the energetic distance between conduction band E_{CB} and Fermi level E_F can be calculated [43].

$$N_D = N_C \exp\left(-\frac{E_{CB} - E_F}{kT}\right) \tag{4.1}$$

Solving for $E_{CB} - E_F$ a value of 0.27 eV is found. Given the band gap of 1.12 eV this yields a valence band offset (VBO $= E_F - E_V$) of 0.85 eV.

In order to prepare a not pinned wafer, i.e. a wafer showing flat band conditions, an elaborate cleaning method is required. Pietsch et al. give a comprehensive review of the typical wet-chemical etching methods used today to remove surface defects [75]. They all finalize the wafer by oxide stripping with either NH_4F or buffered HF solution. The etching procedure employed in this thesis is as follows:

Table 4.1.: General electronic parameters of silicon [43]

Energy gap (indirect), E_G	1.12 eV
Electron affinity, ξ	4.05 eV
Intrinsic carrier concentration, N_i	$9.65 \cdot 10^9$ cm^{-3}
DOS in conduction band, N_C	$2.8 \cdot 10^{19}$ cm^{-3}
DOS in valence band, N_V	$2.65 \cdot 10^{19}$ cm^{-3}

As a first step the samples were cleaned in acetone, isopropanol and ethanol consecutively. Afterwards they were rinsed with deionized water from a Millipore filtration system (resistivity > 18 MΩ). Lastly they were immersed in a mixture of 2/3 concentrated (97 %) H_2SO_4 and 1/3 hydrogen peroxide (40 %) for 15 min. This strongly oxidizing solution (sometimes referred to as Piranha solution) removes most organic contaminants. Afterwards the samples were rinsed, to remove the acid, and subsequently immersed in 40 % NH_4F for 15 min to strip the oxide layer. After an additional rinsing step a clean hydrogen terminated surface prevails [75].

In figure 4.1 the survey XPS spectra after each cleaning step are shown. The untreated wafer is always covered with a native oxide. A strong O 1s signal at 532.94 eV from the silicon dioxide can be seen for the untreated wafer. Using the empiric formula derived by Hill et al. [76] the thickness of the native oxide can be calculated to be approximately 0.9 nm. The thickness is calculated from the ratio between the Si 2p bulk and the Si 2p oxide component. In figure 4.2 the detail spectrum of a Si 2p line is

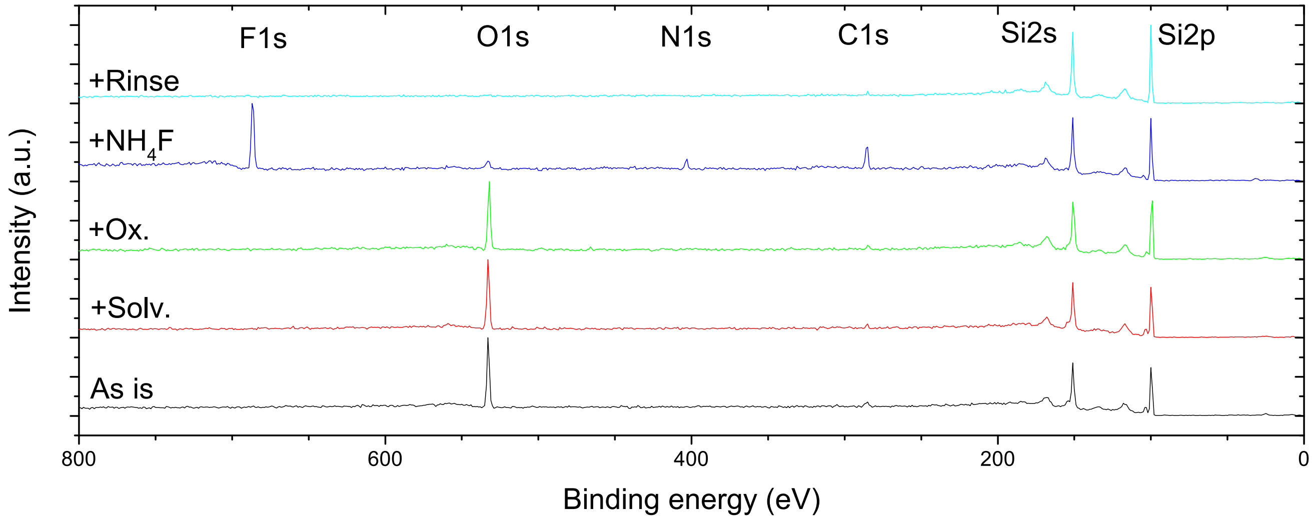

Figure 4.1.: Survey XPS spectra of a n-type silicon wafer. From bottom to top: As is wafer, cleaned with solvents, oxidized in piranha solution, etched in NH_4F and after rinsing.

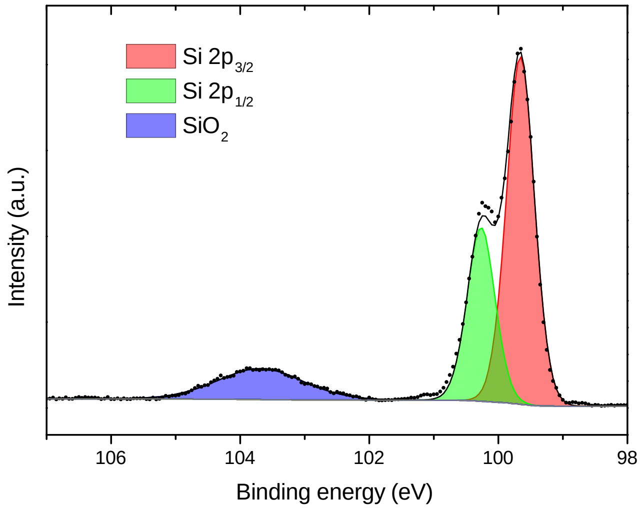

Figure 4.2.: Si 2p detail scan with bulk silicon components (Si $2p_{3/2}$ and $2p_{1/2}$) and the silicon oxide peak (blue). With Hills equation the oxide thickness is deduced from the bulk-to-oxide intensity ratio. [76]

depicted showing the Si $2p_{3/2}$ and Si $2p_{1/2}$ doublet splitting at approximately 100 eV and the SiO_2 component at 104 eV. The spin-orbit splitting of the oxide component was disregarded since it cannot be resolved for the broad oxide peak. The advantage of Hills equation is that it solely relies on the Si 2p line, therefore the SiO_2 thickness can be monitored even if other oxides are deposited on the wafer that also influence the O 1s line.

Uncleaned and in air the wafer usually only shows minor carbon contamination, as a consequence the cleaning in acetone, ethanol and water does not change the contamination level significantly. Only a negligible change in the C 1s signal is observed after washing with solvents. However, the cleaning step was performed anyways to remove the occasional occurrence of dust particles. Afterwards the samples were oxidized in piranha solution to remove all carbon contamination. Consequently, the C 1s emission is further decreased. The oxide layer on the wafer does not grow by the piranha treatment, as is evident by the unchanged O 1s electron emission. As a next step the oxide was stripped in ammonium fluoride (NH_4F). Clearly the O 1s line is diminished. However, instead fluorine and some nitrogen appear in the spectrum, a remnant of the NH_4F treatment. Unfortunately, also some carbon reappears probably resulting from the plastic storage containers of the NH_4F solution. Only after the samples were rinsed with water neither fluorine nor nitrogen were found. Also most of the carbon contamination is washed off. The rinsing step is therefore necessary. During rinsing with water the fluorine termination is exchanged for hydrogen termination, in accordance with mechanism 4.2 [77].

$$\mathrm{Si{-}F + H_2O \rightarrow Si{-}H + OH} \tag{4.2}$$

In early experiments small amounts of sodium were found after rinsing. Spiking the water used for rinsing with a drop of concentrated HCl effectively resolved this problem, as recommended by Constant et al. [78]. The samples were then quickly introduced into the UHV system to avoid an oxidation of the surface. Usually the time between etching and introduction into the load lock chamber is around 5 min. This is enough to avoid the oxidation of the surface, since it has been shown that Si:H can be stable for up to a few hours in air without significant oxidation [79].

The quality of the passivation can be judged by the position of the Si 2p line. With no or an insufficient passivation, the Fermi level at the surface is pinned in mid-gap position [80]. The hydrogen termination can remove this pinning state, thus the surface Fermi level coincides with the bulk Fermi level. As an example figure 4.3 displays the difference between a p- and a n-type wafer. The discrepancy in BE stems from the altered position of the Fermi level within the band gap as illustrated schematically by the inset band diagram. Since BE is measured relative to the Fermi level, a p-type wafer displays a lower BE than a n-type wafer.

The changed doping also influences the workfunction. For the clean nSi:H the workfunction was measured to be 4.31 eV. Given the electron affinity of 4.05 eV and the distance $E_{CB} - E_F$ of 270 meV (derived above), a workfunction of 4.32 eV can be expected, which is in good agreement with the measured value.

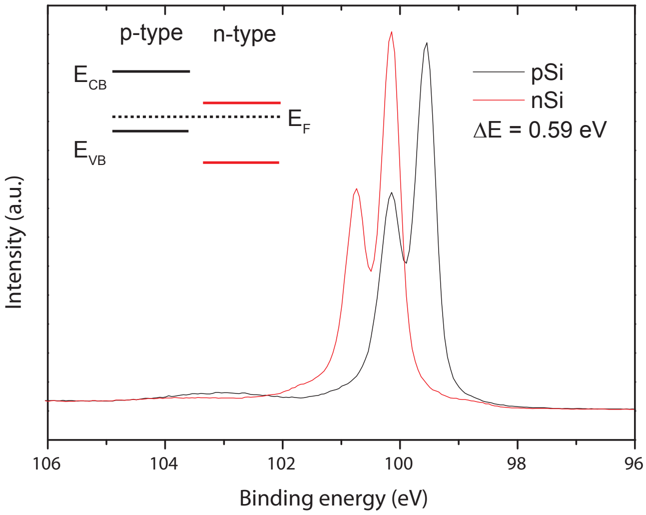

Figure 4.3.: Si 2p emission of a p- and a n-type silicon wafer. The doping changes the position of the Fermi level indicating a good passivation of the substrate. The BE of the substrate shifts accordingly as illustrated by the schematic band diagram.

4.2 Silicon dioxide passivation

It is known that silicon and platinum tend to form platinum silicide [81]. Furthermore the hydrogen termination is not very stable even under UHV conditions. Silicon dioxide on the other hand can passivate the surface with defect densities as low as 10^{10} cm^{-2} [82]. The challenge lies in the fact that the oxide must be thin enough to allow for a charge transfer without a significant voltage loss, while at the same time perfectly saturating the surface. Quite a lot of literature is concerned with the manufacturing of metal-oxide-semiconductor (MOS) structures for integrated circuits (e.g. field-effect-transistors) [77, 82–84]. Yet, in these structures, thick, isolating oxide layers are required. Consequently the parameters proposed do not necessarily apply for thin films. Thin films were successfully synthesized by the Rapid Thermal Annealing (RTA) method, which exposes the sample for a brief moment to a high temperature and an oxidizing agent (oxygen or water) [85–87]. Unfortunately dedicated equipment is needed to employ this technique. Since the preparation chamber can only heat substrates up to 800 °C, a different approach was chosen. Namely, the samples were slowly oxidized at low oxygen partial pressure [88].

In order to have a defined starting condition, hydrogen terminated silicon wafers were prepared as previously described. The samples were mounted on stainless steel sample holders and fixed with titanium screws to avoid cross contaminations from stainless steel. As an oxidizing atmosphere a mixture of argon and oxygen was chosen

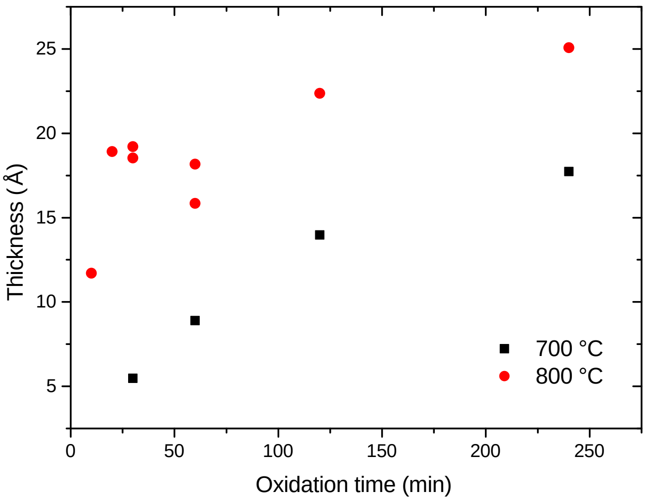

Figure 4.4.: Oxide layer thickness in dependence of the oxidation time and substrate temperature.

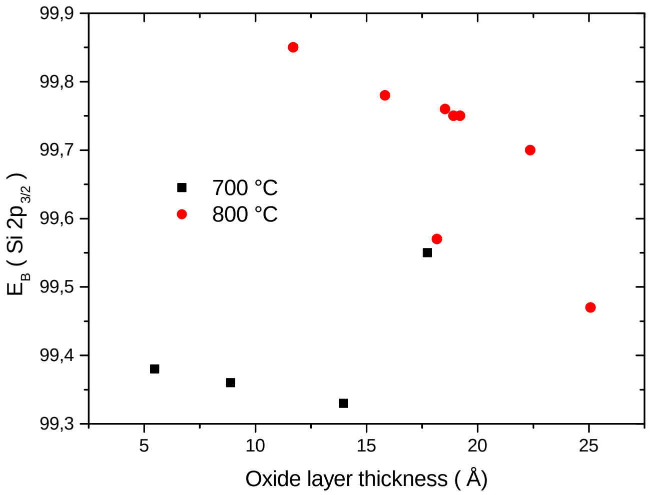

Figure 4.5.: Binding energy of the Si $2p_{3/2}$ line as a function of oxide thickness. The reason for the outlier at 99.6 eV is unknown as the survey XP spectrum shows no contaminations.

(50 sccm Ar, 50 sccm O_2) at a total pressure of 0.1 mbar. The thickness of the oxide layer was determined by the empirical formula proposed by Hill [76]. In figure 4.4 the growth of the oxide layer is plotted against the oxidation time. Clearly silicon oxidizes faster at 800 °C than at 700 °C. At low oxidation times the strong fluctuation illustrates the influence of the initial sample preparation. Trace amounts of water left on the substrate may have a notable impact on the oxidation progress, as water leads to a two orders of magnitude increased oxidation rate. This increase is owed to the enhanced solubility of water in SiO_2 compared to oxygen ($1 \cdot 10^{16}$ cm^{-3} for O_2 vs. $1 \cdot 10^{19}$ cm^{-3} for H_2O) [77].

However the thickness by itself gives no indication whether or not the oxide is sufficiently passivating the dangling bonds of silicon. Being a result of a missing neighboring silicon atom, the dangling bond surface defect state is generally located in the middle of the band gap. For a n-type semiconductor a downward bending at the surface is to be expected [89]. In figure 4.5 the Si $2p_{3/2}$ binding energy is plotted as a function of the previously derived oxide thickness. For the 700 °C samples the BE suggests that the Fermi level is pinned mid-gap, yielding an insufficient passivation of the wafer. Only the last data point after 4 h of oxidation (at 17.5 Å) indicates an improvement in passivation. Probably the diffusivity of oxygen is not high enough yet to completely saturate all defect states at the interface. At 800 °C the BE decreases with increasing oxide thickness. The best passivations are observed at low oxidation times. However, after up to 30 min sometimes minor carbon contaminations could still be identified in XPS. As a consequence, a 30 min oxidation time was chosen as the default parameter. It is still unclear what caused the outlier at 17.5 Å in the 800 °C data set. The survey spectra shows no contaminations, still all core lines are shifted.

Two He II valence band spectra are shown in figure 4.6 for a sample oxidized for 30 min and one for 240 min. Due to the increased surface sensitivity the valence band is dominated by the SiO_2 film. The sharp peak at 11 eV is the characteristic feature of the Si-O molecular bonding orbital. Its occurrence would coincide with a low defect density. However, at the same time the O(2p) doublet can not be clearly resolved after 30 min oxidation time [90]. With increasing oxidation time a slight narrowing of the O 2p orbital is observed. This is particularly visible in the dip between Si-O and O 2p states at 11 eV. Furthermore, the doublet splitting of the O 2p orbital becomes visible. This is a clear indication that the first oxide layer on the sil-

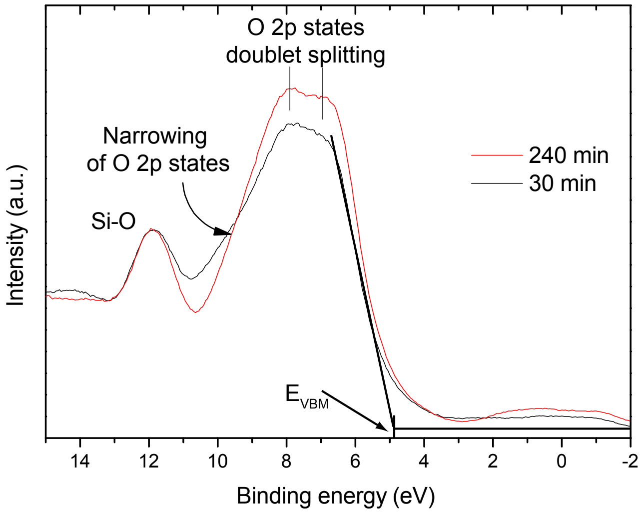

Figure 4.6.: He II valence band of silicon dioxide after 1 hour of oxidation.

icon substrate is distorted, yet it does not negatively affect the passivation. The valence band offset E_{VBM} of silicon dioxide is 4.75 eV and close to results published literature [91, 92]. It was derived by linearly extrapolating the valence band edge to the background signal as indicated by the solid line in figure 4.6. The satellite features between 4 eV and -2 eV result from the excitation with the weaker He II 3p → 1s transition (48.37 eV) that occurs simultaneous to the desired He II 2p → 1s transition (40.81 eV). Due to the higher excitation energy all features are shifted by approximately 7.5 eV to lower BE but are much weaker in intensity [93].

An additional indication for the amount of defects in the oxide layer is the distance between the bulk Si 2p line and its oxide shoulder. For low defect densities a distance of 4 eV for thin films is achieved due to the crystalline structure of the SiO_2 (quartz) layer [94]. Upon transition into vitreous silica the energy difference decreases to 3 eV. In our case, all samples exhibit an energy difference of close to 4 eV. It is therefore reasonable to assume that a mostly crystalline silica passivation layer is formed with a low defect density.

As a side note it needs to be mentioned that besides the Si 2p oxide component, also the O 1s line of SiO_2 changes its BE when switching from crystalline to vitreous SiO_2. As a result, some deposition techniques induce large shifts of the O 1s line, simply by destroying the crystalline nature of the passivation layer. This must not be confused with changes in the Fermi level or band bending effects, respectively.

4.3 7x7 reconstructed silicon

The preparation of 7x7 reconstructed silicon was explored in order to have a clean silicon surface. Typically the preparation involves flashing the wafer to high temperature of 1000 °C and up to 1200 °C for a short period to "lift off" the thin oxide layer [95].

In order to achieve such high temperatures a dedicated electron beam heating stage was constructed. Within the electron beam heating stage electrons from a filament are accelerated onto the backside of the sample holder by applying a high voltage between them. To avoid contact to the substrate holder which is floating at high voltage, the temperature was measured using a pyrometer. Temperatures above 1000 °C were reached but no clean silicon surfaces were obtained from the ex situ wafers. Usually carbon contaminations were found irrespective of the heating rate or the maximum temperature, respectively.

This problem could be avoided by using the previously prepared silicon dioxide passivated wafers. During the oxidation step most contaminant are also removed from the sample holder. Flashing these wafers above 1000 °C lead to the formation of a clean 7x7 reconstructed silicon surface. In figure 4.7 the LEED image of such a reconstruction is shown.

Overall the preparation of reconstructed silicon proved to be rather difficult. On these surfaces also alloying of deposited platinum into the silicon might occur [96]. As a consequence it was refrained from pursuing the preparation of 7x7 silicon further. However, the process described here might be helpful if the usage of unpassivated 7x7 silicon becomes relevant again.

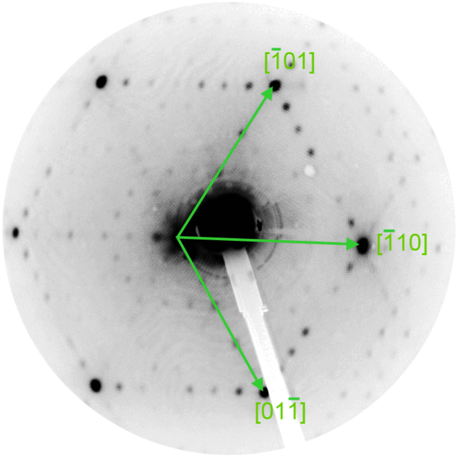

Figure 4.7.: LEED image of reconstructed Si (111)-7x7 after 1000 °C annealing. The wafer is slightly misaligned, shifting the primary spot to the left.

4.4 Conclusion

Both hydrogen and SiO_2 passivated silicon wafers show a good electronic passivation, i.e. a flatband condition. 30 minutes of oxidation time was found to be the best compromise between cleanness and electronic properties. For nearly all experiments SiO_2 passivated wafers were used. They have the big advantage that alloying with the deposits can be excluded. Furthermore when depositing oxides, the stable SiO_2 inhibits the further oxidation of the silicon wafer which is mostly accompanied by the introduction of new defect states.

5 Protection layers

A final goal of all experiments was to deposit highly active catalysts on the silicon tandem cell provided by the Forschungszentrum Jülich. The two p-i-n cells are arranged such that the p-layer is oriented towards the front contact on the glass substrate and the n-type layer to the backside. The high reactivity of the silicon layer leads to the growth of a silicon dioxide layer, especially when immersed in the electrolyte. This layer then poses a barrier for the electron transfer towards the catalyst leading to an undesired voltage loss. Furthermore small pinholes that can occur in the tandem cell enable the electrolyte to reach the ITO front contact. In acidic media this leads to the dissolution of the front contact and a complete disintegration of the cell. To overcome this problem an appropriate intermediate layer is required. This layer has to fulfill three major tasks:

1. *Chemically protect the cell from the electrolyte.*
2. *Adhere well to the substrate.*
3. *Electronically adapt the catalyst to the semiconductor without introducing additional electron transfer barriers.*

Two materials were considered to posses the needed properties. The first one is nickel oxide, besides from being also mostly chemically stable, in addition it possesses a significant catalytic activity for the HER. The second material is titanium dioxide. Typically degenerately n-doped it has a good electronic conductance and is chemically stable in most media. Furthermore it is known to form contacts with low barriers to n-type silicon.

To probe their coupling to the tandem cell, model experiments were conducted. Passivated n-type silicon wafers were prepared as a model substrate. Then interface experiments followed to monitor the formation of potential electrical barriers.

5.1 Platinum silicon interface

The most obvious case to consider is the direct deposition of the platinum catalyst onto the silicon tandem cell. This was modeled using the silicon dioxide passivated n-type silicon samples prepared as described in the previous chapter 4. The platinum layer thickness was determined via XPS measurements, assuming a simple exponential damping model which implies a homogeneous film growth. Platinum was deposited by DC sputter deposition using 5 W of sputtering power and $1 \cdot 10^{-2}$ mbar of argon with a flux of 100 sccm. Upon deposition a shift of all substrate core lines to lower binding energies was observed. The Si 2p line in the end decreases by 0.62 eV, which is shown in figure 5.1. The initial VBO is 0.86 eV in accor-

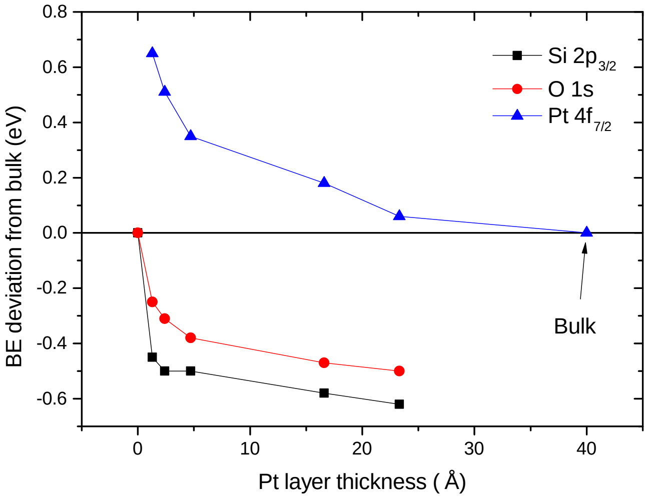

Figure 5.1.: Deviation of the BE of substrate and platinum overlayer in dependence of film thickness.

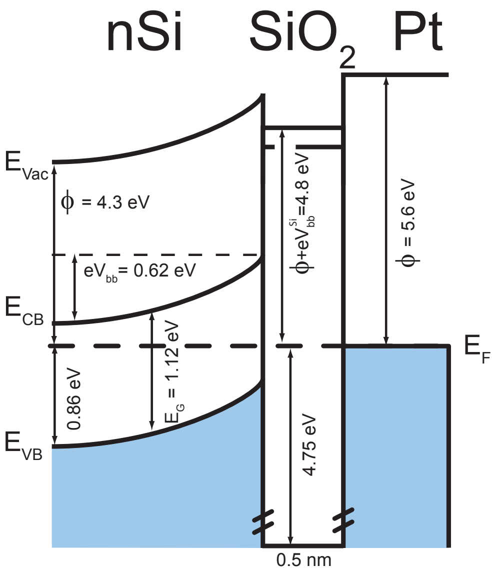

Figure 5.2.: Band diagram derived for a contact between passivated silicon and a thick platinum film (> 3 nm). A strong depletion layer is formed with a band bending of 0.62 eV.

dance with flatband conditions, see chapter 4. The slight discrepancy between the behavior of the Si 2p and the O 1s line is attributed to a change in chemical composition during sputter deposition. For platinum band bending can be excluded due to its metallic nature. Still, even for platinum a shift in BE is observable. However, it results from a chemical change of the thin platinum layer as well as a final state contribution during the photoemission process observable for small supported particles. This effect will be discussed for small clusters in more detail in chapter 8.

From the change in the Si 2p BE a band diagram can be derived, which is shown in figure 5.2. The semiconductor-metal contact leads to the formation of a Schottky barrier with a band bending of 0.62 eV. The initial workfunction difference between hydrogen terminated silicon and platinum is 1.3 eV, thus an interface dipole of 0.7 eV remains at the interface. Although the Schottky contact is in forward bias, the barrier needs to be overcome in order to drive the hydrogen evolution reaction (HER). The high band bending also indicates that the interface is not pinned, hence the thin SiO_2 layer does not disturb the silicon-platinum contact. The valence band offset (VBO) of SiO_2 was determined in chapter 4 to be 4.75 eV. For any charge transfer (especially holes) this low lying valence band of the SiO_2 is irrelevant and will be disregarded in the following. The same argument holds for the conduction band of SiO_2, which is approximately 9 eV higher than the VB and therefore also irrelevant for charge transport [97].

The formed depletion zone hinders the electron transfer from the n-type silicon into the platinum layer. Such a contact will inevitably lead to a voltage loss and as a consequence also to a reduced efficiency of the solar cell. In order to facilitate the charge transfer into the platinum catalyst an intermediate layer is necessary to avoid the strong band bending in the silicon. Consequently, the tandem cell is terminated with n^+-Si layer, which should exhibit no or only minor band bending. In reality however, band bending is also encountered for the tandem cell [98].

5.2 Nickel oxide buffer layer

The first option to be considered to eliminate the barrier inbetween platinum catalyst and silicon substrate was nickel oxide. NiO is stable in alkaline solutions due to the formation of a $Ni(OH)_2$ passivation layer [99]. In addition it is known to be a p-type semiconductor [100]. What makes NiO especially attractive as a passivation layer for the HER is that nickel already has an intrinsic catalytic activity [14].

Stoichiometric NiO was deposited via sputter deposition. A 15 sccm argon and 5 sccm oxygen mixture was used as sputtering gas. The pressure during deposition was $1 \cdot 10^{-2}$ mbar. The sputter source was operated at 40 W, yielding a deposition rate of approximately 6 nm/min. In figure 5.3 the measured XPS spectra of the stepwise deposition can be seen.

The first Ni 2p deposition spectrum at 7.2 Å still deviates from the further more bulk like spectra, highlighting the change in chemical environment, i.e. the (shape) transitions from a reduced NiO into the one observed for stoichiometric NiO [101]. Also metallic Ni and $Ni(OH)_2$ can be excluded from the shape and position (853.80 eV) of the Ni $2p_{3/2}$ line. The O 1s line shows a high BE compo-

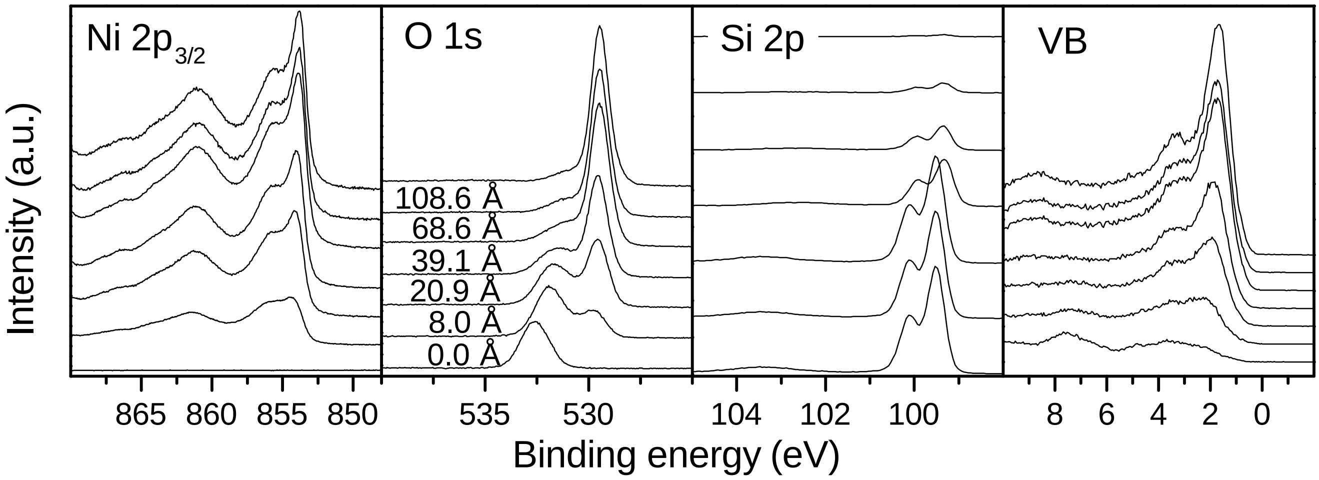

Figure 5.3.: Measured spectra of the deposition of NiO on passivated silicon. The O 1s line splits into a NiO and a SiO_2 component. In the valence band the transition into wide band gap NiO can be observed. The valence band offset was determined from the linear extrapolation of the VB edge, as described in chapter 4.

nent for SiO_2 (532.59 eV) and a low BE component for NiO (531.10 eV). A strong shift to a lower BE for the O 1s (SiO_2) can be identified for the first deposition step. The Si 2p spectrum also shifts and decreases in intensity with each subsequent deposition cycle. The last cycle shows no Si 2p signal, therefore no layer thickness could be determined anymore. In the valence band a transition from silicon into NiO can be observed. The valence band offset decreases from 0.81 eV for silicon to 0.74 eV for NiO.

From the core lines the relative shifts in BE are displayed in figure 5.4. The O 1s line was deconvoluted into a Ni-O and a Si-O species and their BE monitored independently. The change of more than 1 eV in the O 1s line of SiO_2 can again be attributed to a change in chemical environment during sputter deposition. As was already mentioned in chapter 4, the distortion of the crystalline SiO_2 network shifts the O 1s line to a lower BE. Here, sputter deposition seems to damage the crystallinity of the silicon dioxide layer.

The Ni 2p and O 1s line of NiO behave similar, hence no chemical change occurs in the NiO during deposition, as both decrease in BE by 0.4 eV during the deposition process. This behavior is also observed for the Si 2p line. Here a move to a more negative BE by 0.2 eV is identified.

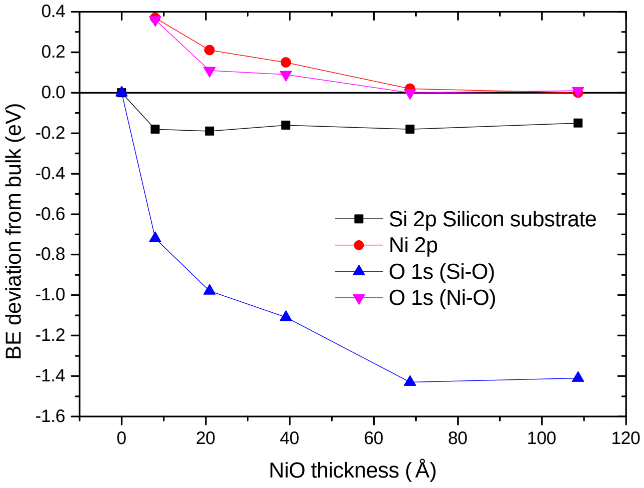

Figure 5.4.: Relative core level shift for the deposition of NiO onto passivated silicon.

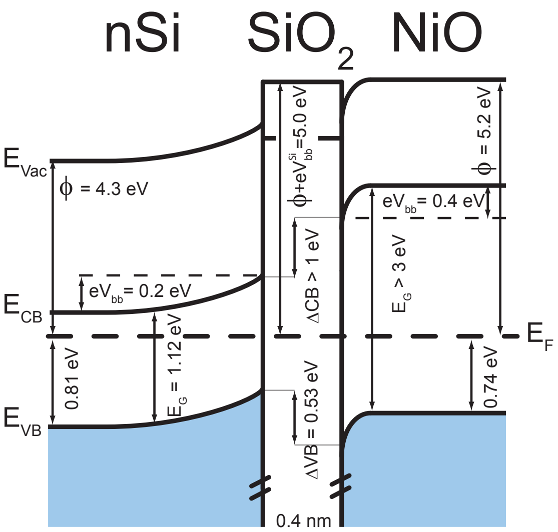

Figure 5.5.: Band diagram of the nSi-SiO_2-NiO interface. The high conduction band offset ΔCB is fatal for the electron transfer.

From these values a band diagram can be constructed as depicted in figure 5.5. The conduction band of NiO was reconstructed from the valence band, by adding the band gap of NiO. The band gap of NiO is difficult to measure, but was estimated to be around 3.2 - 3.3 eV [100, 102, 103]. Comparing the workfunction between the silicon and the NiO layer, a difference of 0.9 eV is found. From that, 0.6 eV relate to the total band bending (0.2 eV in the silicon and 0.4 eV in the NiO), while the remaining 0.3 eV contribute to a interface dipole. Given the valence band offset of 0.74 eV, NiO is clearly p-type as expected. A hetero-contact is formed with both semiconductors developing a depletion zone at the interface. The parallel change of the Ni 2p and the O 1s (Ni-O) BE indicates that no chemical change occurs in the NiO layer and that the shift in BE is due to band bending. Furthermore, the high band gap of NiO leads to a conduction band offset ΔCB larger than 1 eV. This barrier needs to be overcome in order to transfer electrons from the n-Si to the catalyst. For this reason NiO might be a good catalyst, but is not an ideal buffer layer for the HER.

The situation could be different when considering hole transport in the valence band for the oxygen evolution reaction (OER). Here, a valence band offset ΔVB of 0.5 eV is encountered. This barrier should be significant reduced when p-type silicon is used in a n-i-p structure. Nickel also shows activity towards the OER. Adding its p-type nature, it could be a viable passivation – or even catalyst layer for the OER. However, whether the hole conductance is sufficient for this process should be clarified beforehand.

5.3 Titania buffer layer

As an alternative to NiO, titania was considered. Titania is thermodynamically stable even under reductive conditions in neutral to alkaline solutions. It is not stable in concentrated acids [104]. Due to the doping effect by oxygen vacancies it is usually n-doped and has a good electric conductivity.

Titania was sputter deposited reactively from a metallic titanium target. The deposition power was 40 W at a pressure of $5 \cdot 10^{-3}$ mbar. 2.5 % oxygen were added to the Ar sputter gas, yielding a total flux of 20 sccm. No additional heating of the substrate was used to crystallize the titania layer. In X-Ray diffraction (XRD) only a broad background is visible indicating the formation of amorphous TiO_2. The diffractogram and additional information concerning the coupling to the real tandem cell can be found in the corresponding publication [98].

Figure 5.6 shows the development of the primary lines of a passivated n-type silicon upon the deposition of titania. In the O 1s spectra bonding to titanium and to silicon can be distinguished. During the stepwise deposition the Ti 2p signal increases, whereas the Si 2p substrate signal is damped. The initial binding energy of the O 1s line of SiO_2 is 533.0 eV, the final BE of the O 1s line of TiO_2 is 530.3 eV. From the Si 2p spectrum the thickness of the dioxide layer can be extracted. It increases from 1.3 nm at the beginning to 1.6 nm after the second to last deposition step. After the final deposition step no Si 2p line is visible anymore,

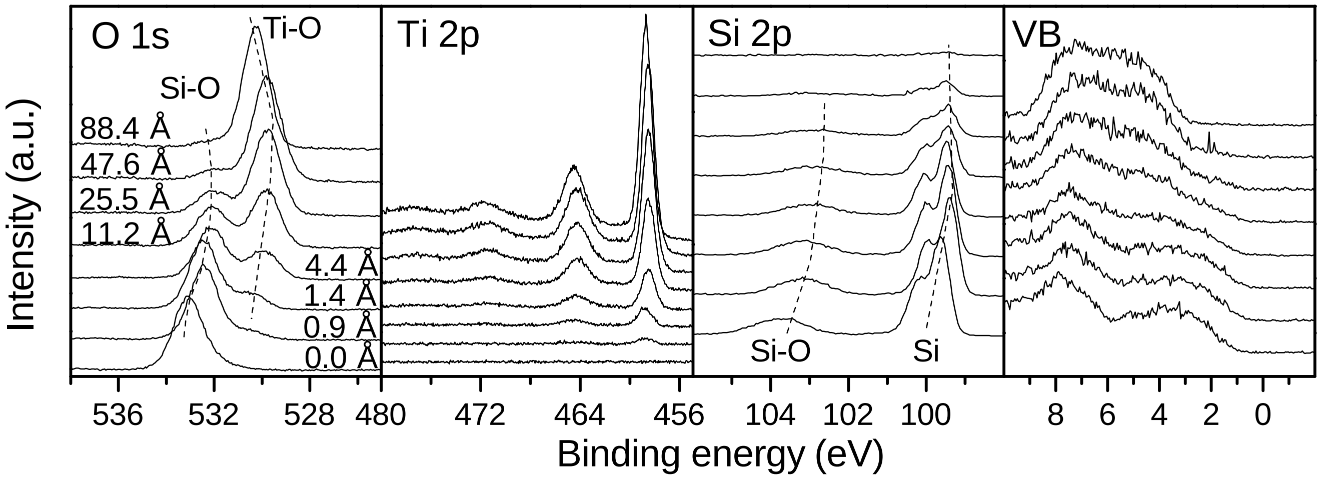

Figure 5.6.: Measured XPS spectra of the interface formation between nSi-SiOx-TiO_2. The O 1s spectrum shows components of TiO_2 and SiO_2. The valence band changes into the wide band gap TiO_2.

making the determination of the thickness of the interfacial oxide impossible. The valence band shows a clear transition from n-silicon, with a valence band offset (VBO) of 0.89 eV to TiO_2 with a VBO of 2.87 eV. From the initial VBO it can be concluded that the silicon is sufficiently passivated at the start of the experiment.

In order to identify the TiO_2 phase, the distance between Ti 2p and the valence band edge (Ti $2p_{3/2}$ – VBM) was determined to be 455.84 eV. In contrast, Pfeifer at al measured 456.0 eV for anatase and 456.4 eV for rutile [105]. It stands to reason that amorphous TiO_2 was produced, due to the low deposition temperature. In fact, the distance between O 1s and Ti 2p for amorphous TiO_2 produced at 210 °C was evaluated to be 71.5 eV, identical to the value found here [106].

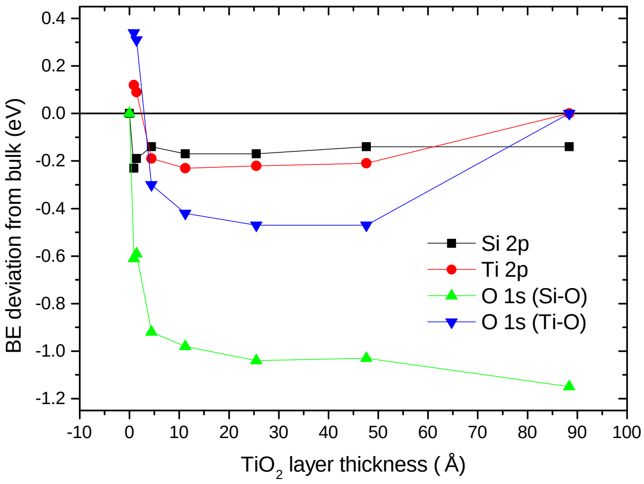

Figure 5.7.: Deviation of core lines from the bulk material. A strong additional chemical shift is visible in the O 1s line. From the Si 2p line a small band bending can be deduced.

The core level shifts are depicted in figure 5.7. Upon the first deposition there is a 230 meV shift visible in the substrate signal that reduces to only 140 meV when the last layer is applied. In contrast, the O 1s line shows a shift up to more than 1 eV within the first deposition steps. As in the case of NiO, this is direct evidence for a chemical change in the thin passivation layer. The Ti 2p signal starts at higher than bulk BE and then transitions into a lower BE. The same trend is observed for the O 1s (Ti-O) signal, however the magnitude of the observed shifts in the Ti 2p and O 1s of titania differs. This quantitative difference in BE change can be understood as a mixture of chemical shift and doping effect. At first the thin titania layer shows a high BE, due to the proximity to the silicon dioxide layer. As one monolayer is completed, at roughly 3 Å, the BE shifts to intrinsic titania. Upon further deposition the oxygen deficiency leads to the n-doped character and the line arrives at a typical Ti 2p binding energy for n-TiO_2 of 458.71 eV. This value was already reported for mildly reduced TiO_2 [107, 108].

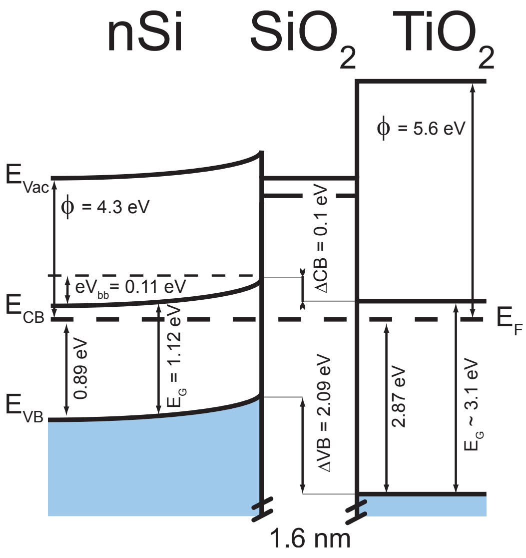

Figure 5.8.: Band alignment between passivated silicon and titania (t = 9 nm). No significant barrier is formed.

In the silicon substrate almost a flatband condition is maintained. Figure 5.8 shows the final band alignment between silicon and the titania layer. Since, the large workfunction difference of 1.3 eV leads to only a minor band bending, a strong interface dipole is present at the interface.

In the silicon substrate a depletion layer with a band bending of 0.11 meV remains. The band gap of the amorphous titania layer was assumed to be approximately 3.1 eV [109]. Given the VBO of 2.87 eV, only a small conduction band discontinuity ΔCB is present, except for the silicon dioxide layer.

With this experiment it was proven that in general the energetic lineup between n-type silicon and titania is promising. For a good conduction across the interface the next step would be to reduce the thickness of the silicon dioxide layer, thus enabling an easier tunneling process between the two materials.

5.3.1 Platinum on TiO_2

The second important charge transfer mechanism is the one across the TiO_2/Pt interface. Platinum was again sputter deposited, as described in chapter 5.1. The as measured XPS spectra are displayed in figure 5.9.

There is no trend visible in the O 1s and the Ti 2p core level emission. They scatter around 100 meV, but no distinct band bending can be observed. The Pt 4f line is shifted from a high value of the binding energy (72.4 eV) down to the bulk value of 71.2 eV [110]. This can be attributed to the electrophilicity of the TiO_2 substrate as well as the limited hole screening of the thin film. For isolated platinum atoms it has been shown that a partial negative charge is transfered from the platinum to the titania substrate, yielding a higher BE in XPS [111]. The valence band reveals that within the first two depositions, platinum is not yet in its metallic state. A fact that is clearly visible as a lack of states around the Fermi level. Overall the contact formation resembles the contact between two metals, which is to be expected considering the typically high charge carrier density in TiO_2 ($\approx 10^{18}$ cm^{-3}) [112]. Thus there should be no voltage loss associated with the TiO_2/Pt contact.

In figure 5.10 the final band alignment of the complete stack is drawn. The only barrier that is encountered is the silicon dioxide layer. This layer needs to be avoided or made thin enough to enable tunneling into the titania layer. Even though titania is a semiconductor, no Schottky contact is formed and no relevant electron transfer barrier exists between titania and the platinum catalyst. The contact is of the Bardeen type. The good electrical conductivity of titania should enable it to collect the current across the whole device and transfer it into the small platinum particles.

5.4 Conclusion

As was already stated in the introduction, three criteria must be fulfilled for a good passivation layer. Good adhesion to the substrate, high electrical conductivity, and chemical stability. In this context good electrical conductivity also implies that in our case no electron transfer barriers are formed from the substrate to the catalyst layer. Direct platinum deposition leads to the formation of a strong depletion zone on the n-Si, that is not beneficial for the charge transfer. But the real tandem device has a strongly

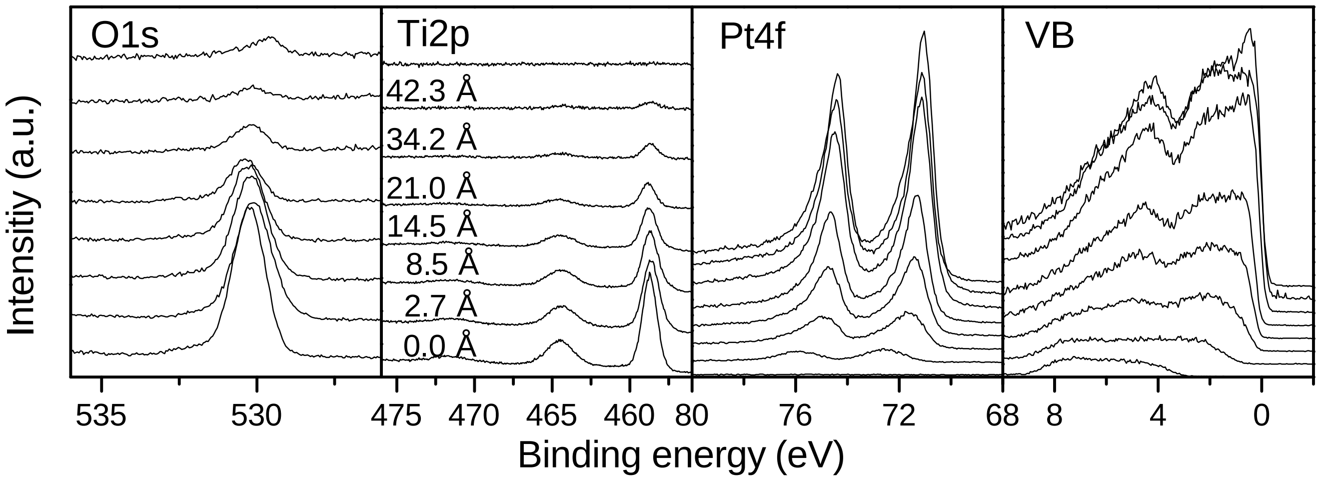

Figure 5.9.: Measured spectra of the interface formation between TiO_2-Pt.

n^+-doped amorphous silicon layer. Albeit this layer being highly doped, XPS investigations revealed that it behaves analogous to the model experiments conducted here [98]. For NiO the large valence band offset is a major drawback. Even if charge injection would not be inhibited, its p-type character would not make it a good electron conductor for the HER. It could only be potentially employed as a catalyst considering a low thickness, thus allowing charge transfer by tunneling but not as a thick protective layer.

Titania, on the other hand, satisfies all mentioned criteria, although its deposition by sputtering increases the thickness of the interfacial oxide. To circumvent the creation of the interfacial SiO_2 layer a soft deposition process such as atomic layer deposition (ALD) of TiO_2 could be explored. Seger et al. were able to show that ALD-titania can be long term stable also under HER conditions while giving a good contact to the silicon substrate [113].

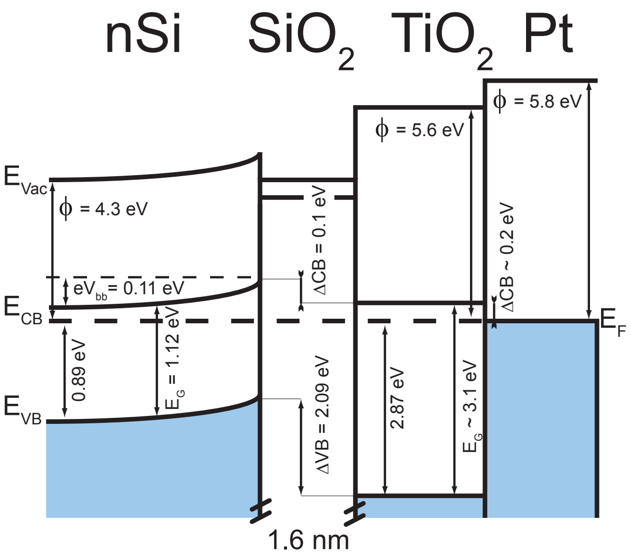

Figure 5.10.: Final band alignment of the n-Si/SiO_2/TiO_2/Pt interface. No significant conduction band barriers are encountered, except for the SiO_2 layer. The conduction band offset strongly depends on the chosen band gap of TiO_2.

6 Catalysis on Pt-single crystal surfaces

Before polycrystalline platinum films or platinum clusters (chapter 7 and 8) were investigated, first experiments with platinum single crystals were conducted [114]. The three main crystal directions (111), (110) and (100) were investigated. To probe the electronic structure these crystals they were explored by a combination of XPS and UPS measurements. Orientation and quality of the surfaces were checked with LEED. A quantity of interest in these experiments is the d-band center, since it should correlate to the catalytic activity.

To evaluate the electrochemical activity these crystals were also investigated in the in-situ electrochemical cell. The active surface area was determined via hydrogen ad- and desorption measurements. This allows to evaluate the correlation between electronic structure and catalytic activity.

Some of the electrochemical data presented here were contributed by Frederick Heinz during his Bachelor thesis [115].

6.1 Single crystal preparation

Platinum single crystals with 1 cm diameter and 0.5 mm thickness were purchased from SPL. The crystals expose the following surface orientations: (111), (110) and (100). They were aligned within 0.1 degrees and had a surface roughness of less than 30 nm. As a first step to remove most contaminants the crystals were etched in nitric acid (40 wt%) or piranha solution. A XPS spectrum after etching in piranha solution is shown at the bottom in figure 6.1. After the etching procedure no carbon contaminations are found, however oxygen from adsorbed sulfates is visible. Therefore, the crystals were sputtered for several cycles with argon ions with a kinetic energy of 2 keV. This treatment results in a clean, but amorphous surface. To recrystallize the surface the crystals were annealed to approximately 1000 °C in a dedicated electron beam heating stage [116]. Usually this leads to a recurrence of carbon contaminations due to desorption from the sample holder, as was identified by XPS. Only after several sputter and annealing cycles a clean surface is obtained as shown in the topmost spectrum in figure 6.1.

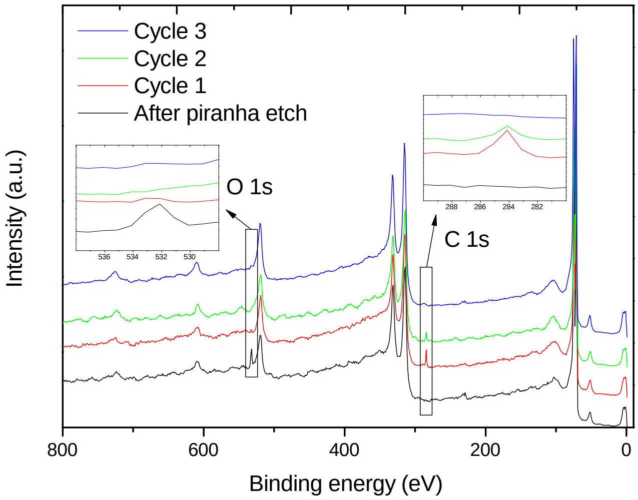

Figure 6.1.: XPS spectra of consecutive sputter, annealing cycles to prepare a clean platinum (111) surface.

After it was confirmed via XPS that the samples were clean, their crystallinity was checked by taking LEED pictures (OCI Inc.). In figure 6.2 the LEED pictures of the primary crystal directions are shown. The (100) direction shows the hexagonal (hex) reconstruction often observed for samples cooled from elevated temperatures [116, 117]. During cool-down the topmost layer relaxes into a more dense pseudo-hexagonal packed surface [118]. The resulting LEED pattern is complicated to analyze as it leads to a supercell of size 5x20, giving rise to the two adjacent LEED spots observed along the primary directions in figure 6.2 (a). The (110) samples shows no reconstruction at a first glance. However, there is an indication of very weak

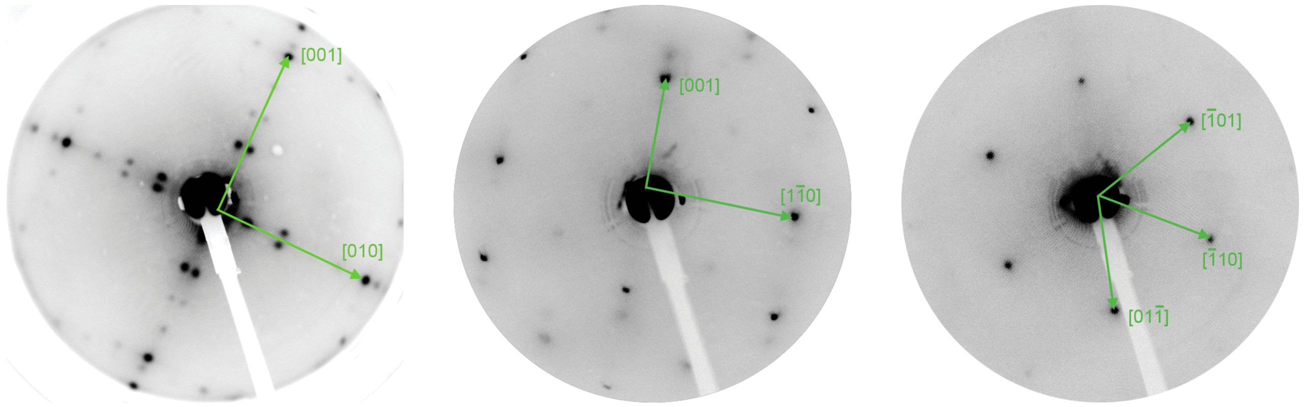

(a) Pt-(100)-hex 50 eV **(b)** Pt-(110) 100 eV **(c)** Pt-(111) 60 eV

Figure 6.2.: LEED images of the Pt (100), (110) and (111) single crystals and the used electron energy. In squared brackets the crystal directions are marked.

Table 6.1.: Work function of clean platinum single crystals prepared by sputter-annealing.

(hkl)	He I	He II	XPS	Lit [121]
(100)	4.98	4.98	5.13	5.86
(110)	5.25	5.26	5.26	5.72
(111)	5.35	5.34	5.39	5.94

c(2x2) spots. These can be attributed to minor amounts of adsorbed oxygen [119, 120]. Lastly, the platinum (111) surface shows no reconstruction.

The work function is also a quantity strongly influenced by the surface termination. In table 6.1 the work functions obtained for all three crystal direction are listed and compared to literature values.

Overall the work functions obtained from XPS measurements in the DAISY-Fun are reduced compared to literature values [121], albeit the individual techniques being in fair agreement. The exact cause of this can not be ascertained, since XPS shows no contaminations on these samples. However, it clearly shows that the work function is a very surface sensitive quantity that can be easily modified by minor amounts of adsorbates.

6.2 Electrochemical analysis

To avoid contaminations and adsorbates on the clean surface, electrochemical measurements were conducted in the in-situ cell. The enclosing chamber is constantly flushed with argon to ensure an inert gas atmosphere. To remove dissolved oxygen from the electrolyte that can lead to a cathodic parasitic current, the 1 M NaOH solution was purged with argon prior to the experiment.

At first it was checked if the crystals are clean and exhibit the correct surface orientation by measuring their characteristic hydrogen adsorption/desorption features by cyclic voltammetry (CV). Figure 6.3 displays the second recorded CV cycle for the three crystal directions after sputter annealing and immersion in the electrolyte. In accordance with literature the desorption features for the respective crystal directions are present. The (110) direction shows its hydrogen desorption feature at a potential around 0.3 V vs. RHE (shaded in red). For (100) this occurs at around 0.4 V (shaded in green). For the (111) direction the OH^- adsorption around 0.8 V vs. RHE is characteristic (shaded in black). These values are in agreement with literature data [18, 73]. However, their shape is not as sharp as reported in the literature, an indication that still some

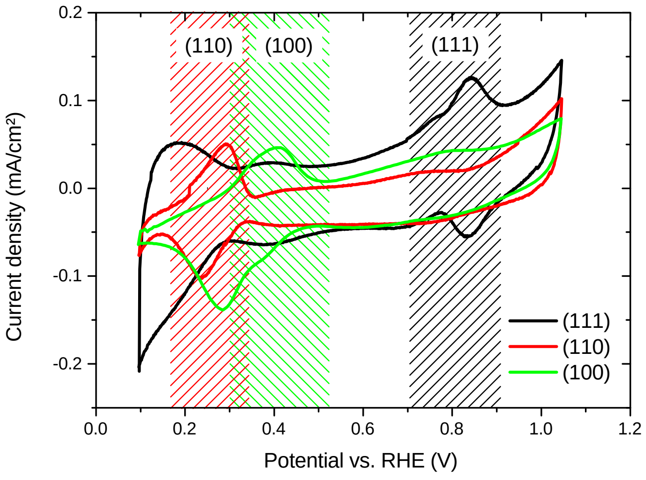

Figure 6.3.: Cyclovoltammograms at 100 mV/s scan rate of the primary platinum surfaces. Each surface exhibits the adsorption and desorption of either hydrogen or hydroxide at a unique potential as indicated by shaded the areas lines.

contaminations are present, probably introduced with the electrolyte.

For the (111) surface the OH-adsorption was only recordable during the first few initial cycles. After several cycles the (111) surfaces diminishes and transforms into a superposition of (110) and (100) surfaces, as can be observed in figure 6.4. With increasing cycle number the OH^- adsorption feature on Pt (111) is diminished. At the same time there is an increase in (110) and (100) desorption peaks. Already the first cycle shows a (110) hydrogen desorption feature at 0.1 V vs. RHE that increases with the cycle number. This probably is one of the edge defects that initiate the transition from (111) to (110) and (100). It is well known that the (111) facet is the least stable one in the electrolyte and therefore decomposes into the other crystal directions [122]. In extreme cases this leads to an overall roughening of the platinum surface [123].

The amount of charge displaced during the ad- or desorption cycles gives information about the number of active sites where the according process occurs. The surface charge density can be obtained by numerical integration of each such feature as described in chapter 3.4.1. Since typically the desorption is sharper and more well defined, it

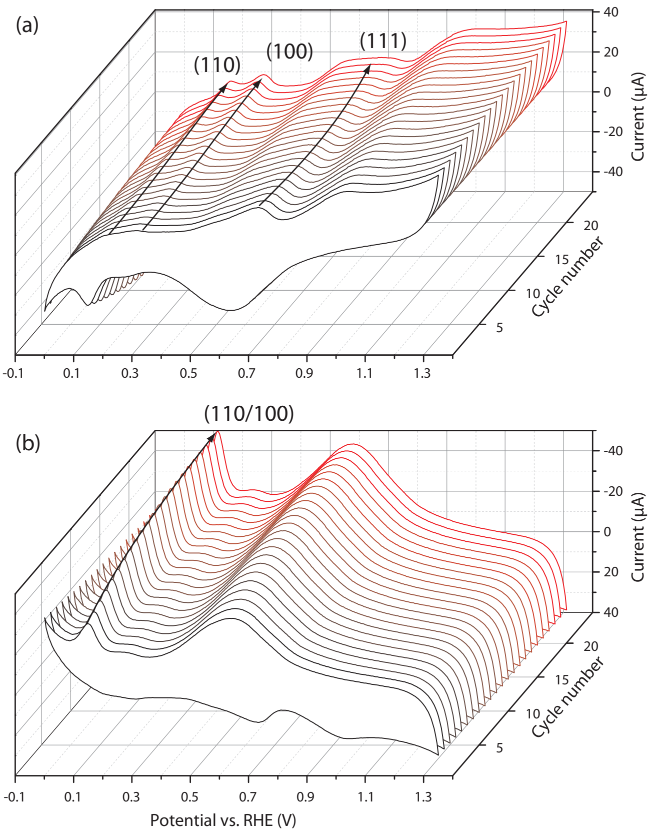

Figure 6.4.: Destruction of the (111) surface during electrochemical cycling. In (a) the anodic features are visible, whereas (b) shows the cathodic ones. With increasing cycle number the Pt-(111) specific OH^- adsorption peak vanishes, while the (110) and (100) features increase in intensity. The first cycle already shows a (110) hydrogen desorption feature at 0.1 V vs. RHE, that also increases during cycling.

Table 6.2.: Displaced charge surface density for characteristic peaks and overall active surface area (Q_{upd}). Q_{ideal} is calculated from the lattice parameters.

(hkl)	Q_{1x0}	Q_{111}	Q_{upd}	Q_{ideal}
		[μC/cm²]		
(100)	62	0	117	208
(110)	137	0	246	147
(111)	0	130	58	294

was used to calculate the number of corresponding sites. The displaced charges are tabulated in table 6.2.

Hereby Q denotes the charge density displaced within the corresponding potential regime. The (110) and (100) features were combined as they overlap and are not clearly separable from each other. In lack of a hydrogen signal for the (111) surface, the hydroxide adsorption at 0.85 V was used. The total amount of under potential deposited hydrogen is integrated to yield Q_{upd}. Unfortunately, the (111) surface has no clear hydrogen evolution onset which makes the determination of Q_{upd} for this surface challenging. Q_{ideal} is calculated from the lattice constant from platinum of a = 3.9231 Å, assuming one adsorbed hydrogen atom per platinum surface atom [56]. The strong discrepancy between Q_{upd} and Q_{ideal} reveals that in the in situ cell still unwanted side reactions or contaminations are present.

In addition, the catalytic activity of such surfaces is of great interest. As a benchmark the overvoltage at 5 mA/cm² current density was defined. For this a single sweep from cathodic potentials using 10 mV/s scan rate was recorded. In figure 6.5 the pseudo Tafel plots for the three single crystals are shown. They deviate especially from real Tafel plots in that they lack the bubbling of hydrogen gas along the surface. Thus, they lack the HOR as the complementary oxidation reaction. To achieve some more reliable information the scan direction was always from reductive to oxidizing current, e.g. from left to right. This ensures that some hydrogen is present on the surface when the curve passes through the standard potential. However, as can be seen in figure 6.5, the curves are shifted to the right and their singularity is not at the origin. This kinetic effect was excluded for the determination of the overvoltage, i.e. the overvoltage is measured against the reference potential.

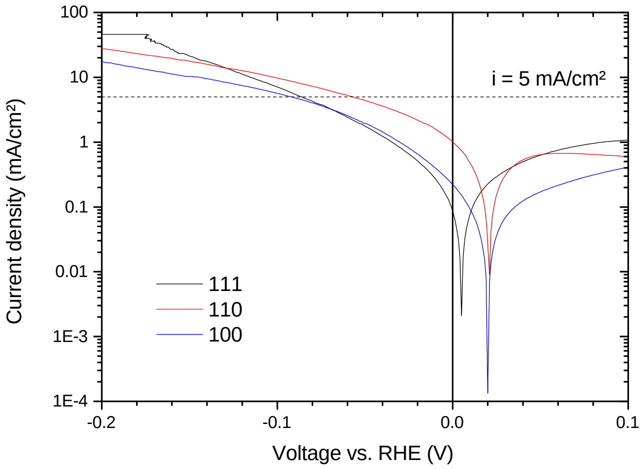

Figure 6.5.: Pseudo Tafel-plots for the HER on platinum single crystal surfaces.

Table 6.3.: Measured and literature values for overvoltage at 5 mA/cm² and measured exchange current and Tafel slope

(hkl)	$\eta_{5\ \mathrm{mA/cm^2}}$		Tafel	
	Meas.	Lit. [18]	j_0	slope
	[mV]	[mV]	[mA/cm²]	[mV/dec.]
(100)	96	57	1.38	165
(110)	58	27	2.69	181
(111)	86	132	0.70	100

In table 6.3 the overvoltage at 5 mA/cm², the exchange current density and the Tafel-slope are listed. The overvoltages for (110) and (100) are higher than in literature, albeit [18] used only 0.1 M NaOH.

According to literature the catalytic activity for the HER changes in the order (111) <<(100) <(110) [18]. In the measurements shown in figure 6.5 the (111) direction performed better than expected. This is a result of the aforementioned instability of the (111) surface. In fact, when recording the overvoltage, it was already transformed into a mixture of (110) and (100) due to previous cycling, hence it shows the improved value of the overvoltage.

Bagotzky et al. found that the exchange current density j_0 in alkaline solution is rather constant and independent of crystal direction at 0.1 mA/cm^2. Their value is significantly lower than the values encountered here. Since the current depends exponentially on the potential, any error in potential has an amplified effect on the exchange current. It stands to reason that when measuring in equilibrium conditions, i.e. the solution is hydrogen saturated, the curves would be shifted to the left, leading to much smaller exchange current densities.

The Tafel slope on the other hand is independent from the potential and therefore also agrees with typical values found in literature.

6.3 Photoelectronspectroscopy

As was already discussed, the d-band center of platinum should play a decisive role in the catalytic efficiency. In contrast to core XPS lines, a non-ambiguous deconvolution is not easily possible. However, the width of the 6s^1 states and their low contribution to the overall DOS enables us to treat the platinum VB as being mostly d-like. Hence, to determine the d-band center first a Shirley background is subtracted from the spectrum (10 eV – -2 eV), after which the DOS is integrated from 10 eV up to the Fermi edge. The median of this integration yields the approximate d-band center [29]. In He I measurements the tail of inelastically scattered electrons gives rise to an exponentially decaying background. Consequently He II spectra were taken for the evaluation of the d-band center.

In figure 6.6 the VB spectra of the three clean crystal surfaces are shown. The spectra were recorded in the DAISY-FUN setup (XPS hν = 1486.74 & UPS hν = 40.81 eV) and at the synchrotron at BESSY II (hν = 700 & 100 eV). The d-band center was derived for each technique and crystal direction and is highlighted by a vertical line in each plot. The general shape correlates well with DFT calculations [124].

The (111) direction shows a clear increase of states around 6 eV with increasing excitation energy. They are a result of an increased bulk sensitivity at higher excitation energies. These states between 8 eV and 5 eV are also present for the other crystal directions, however there they are independent of the excitation source. This development of a tail when going from more surface sensitive He II to more bulk sensitive XPS measurements has a large impact on the d-band center. Here a strong deviation depending on the excitation source is noticeable. Close to the Fermi energy a sharp peak can be found for all excitation energies. It results from the formation of a surface band at the Pt-(111) surface [125].

In (110) direction the least deviations between the different techniques are visible. As a result also the calculated d-band center deviates only slightly.

Finally the (100) direction is defined by a rather flat DOS close to the Fermi level. Again the deviation between techniques is minor, leading to a rather excitation independent value of the d-band center.

In addition to the observed changes of the valence band, one would expect a shift in the Pt 4f core level BE due to the increased surface sensitivity. As explained in chapter 2.3 for clusters, the same argument holds for surface atoms. For platinum ($m > 5$) a negative core level shift, i.e. to a lower BE, would be expected. However, in the 700 eV measurement, no Pt 4f core level shifts were identified compared to the XPS measurement. At lower, more surface sensitive, energies the Pt 4f level was not accessible, hence no conclusion can be drawn about the presences of a surface induced core level shift.

Since the d-band center should be a measure for the overall catalytic activity, it is worth to explore the determined values further. In figure 6.7 the binding energy of the d-band center is plotted for the different techniques. It is evident that the tailing observed for the (111) direction leads to a divergence of almost 1 eV for the value

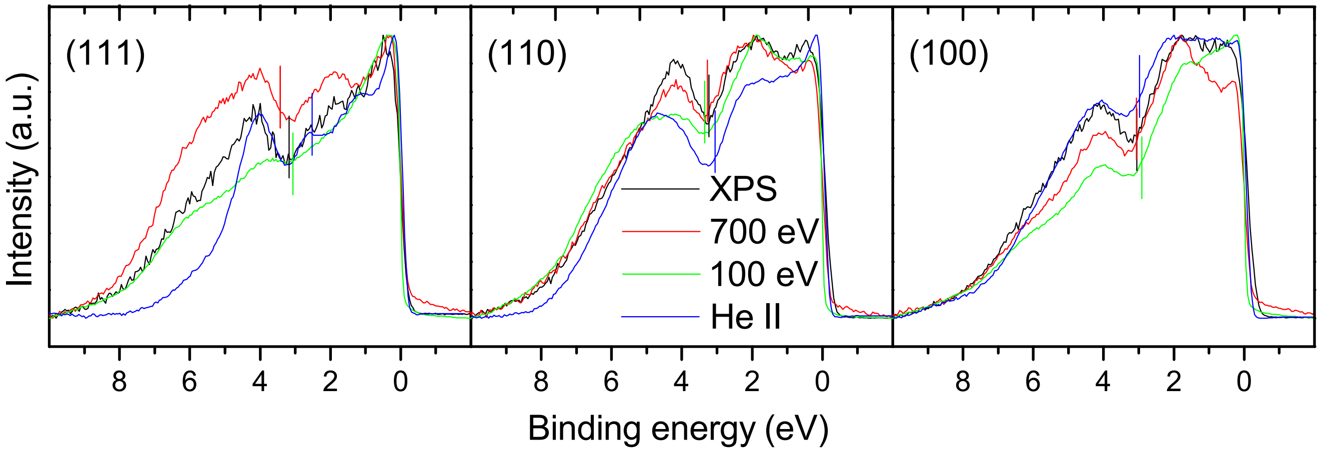

Figure 6.6.: Valence band spectra recorder for platinum single crystals by different PES techniques. As a solid vertical line the d-band center is marked for each direction and technique.

of the d-band center. The average of all techniques of 3.05 ± 0.38 eV has therefore little meaning. However, the d-band centers obtained from the (110) and (100) crystal direction are well defined, with 3.23 ± 0.13 eV and 3.00 ± 0.07 eV, respectively. In a related study, Hofmann also found that the platinum d-band center strongly scatters depending on the measurement technique or DFT algorithm [30].

From DFT calculations a d-band center of 2.44 eV for the (111) direction was calculated using a thin slab model [23]. This is in good agreement with the value obtained from the He II measurement, as it is the most surface sensitive technique. Generally the d-band centers obtained in this thesis tend to be too high, when compared with literature [29].

Recalling the already discussed volcano relationship, it should be possible to correlate the d-band center BE to the catalytic activity. In order to weaken the hydrogen-oxygen bond a partial electron transfer from water to platinum was predicted [126]. The more energetically lowered that d-band center, i.e. the higher the BE, the easier this partial electron transfer can occur. For the He II measurement we can qualitatively sustain this assumption, as we also find that change in d-band center BE (111) << (100) <(110), agrees with the trend in activity (110) >(100) >> (111).

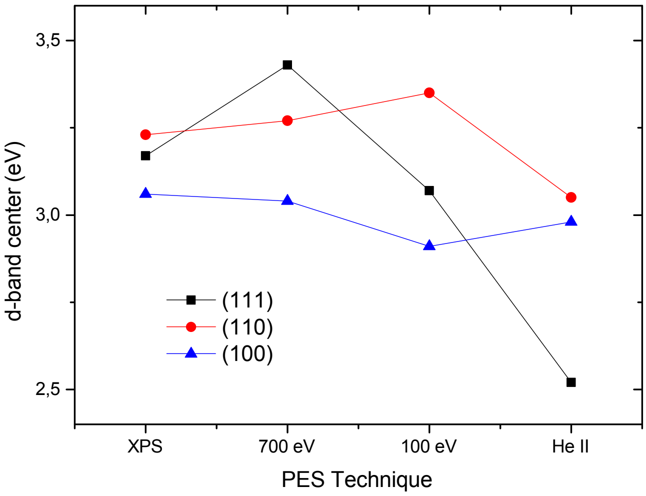

Figure 6.7.: d-band centers derived by different excitation energies. The (110) and (100) direction are well reproducible, however (111) changes significantly depending on the excitation energy.

However, given the strong fluctuation in these values this correlation is hardly conclusive.

The excitation energy has a direct influence on the surface sensitivity as well as the cross section for the photoemission process. Both influence the shape of the valence band. The simplification of using solely the d-band center therefore appears to be insufficient. The same conclusion was found by Hofmann when investigating a multitude of transition metals [30].

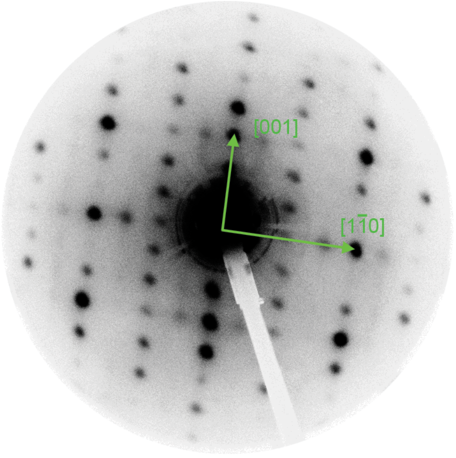

Figure 6.8.: LEED diffraction pattern of a Pt-(110)-(4x3)-S reconstruction with 100 eV beam energy.

For the HER also steric considerations that are not evident in the photoelectron spectra are important and have to be kept in mind. This will be especially important when switching from single crystals to small clusters. Here the determination of the d-band center will be even more challenging as it will also be influenced by the final state effect observed in PES measurements.

6.4 Water adsorption on platinum single crystals

During the preparation of new clean single crystalline surfaces for water adsorption experiments at BESSY II, the Pt (110) surface was contaminated with sulfur. Source for the contamination was probably the etching step in concentrated sulfuric acid. The subsequent sputter annealing cycles removed the oxygen from the sulfate, however sulfur remained on the surface. This was revealed in LEED studies showing a peculiar (4x3) reconstruction, unknown for clean Pt-(110) (figure 6.8) [127]. The contamination was also revealed in SXPS at BESSY II, unfortunately however it was missed in the XPS in Darmstadt due to its low signal intensity.

As a result the platinum (110) single crystal showed no water adsorption, which is probably due to the passivation with a sulfur layer and a strongly decreased water-platinum interaction.

On Pt-(100) and Pt-(111) water adsorption was possible. To reveal the minor changes between the adsorption steps difference spectra were deduced, effectively removing the high DOS of platinum and revealing the electronic states of adsorbed water. First, from each spectra a Shirley background was subtracted, ranging from 15 eV to -2 eV. Secondly, the spectra were normalized at the highest intensity. Finally, the clean platinum spectrum was subtracted from the one obtained after adsorption. In figure 6.9 the difference spectra for Pt-(100) (a) and Pt-(111) (b) are shown. The strong noise is a consequence of the small contribution from water to the overall DOS.

When looking at the difference spectra the usual molecular orbitals (MO) of water become visible ($1b_2$, $3a_1$ and $1b_1$). On Pt-(111) water adsorbed better as can be seen by the overall higher intensity. The pronounced $1b_1$ orbital is shifting to higher binding energies with increasing coverage. This can be interpreted as a stabilization of the water layer by the formation of hydrogen bridges via the oxygen lone pair ($1b_1$ orbital) [128].

The valence band was deconvoluted into its primary molecular orbital contributions as indicated by the shaded areas in figure 6.9. Namely, the $1b_2$, $3a_1$ and $1b_1$ contribute to the valence band of water. In figure 6.10 the contribution of each molecular orbital compared to the total signal is depicted. It was only carried out for samples exposed to 2 and 5 Langmuir of water because lower coverages are to vague to achieve a reliable result. As a reference the data of a pure ice film obtained at 10 L coverage is also given. It is noteworthy that the electronic structure of the adsorbed water film deviates significantly from the pure ice. When deconvoluting the three MOs of water (shaded areas in figure 6.9), pure ice shows a $3a_1$ molecular orbital with higher FWHM due to a charge redistribution from the oxygen lone pair ($1b_1$) [129]. This charge donation due to the hydrogen bridges is even more pronounced for liquid water [128].

In the case of adsorption on platinum however, the contribution of the $3a_1$ MO is decreasing with increasing water coverage. In fact, low coverages (up to 1 L) do not show

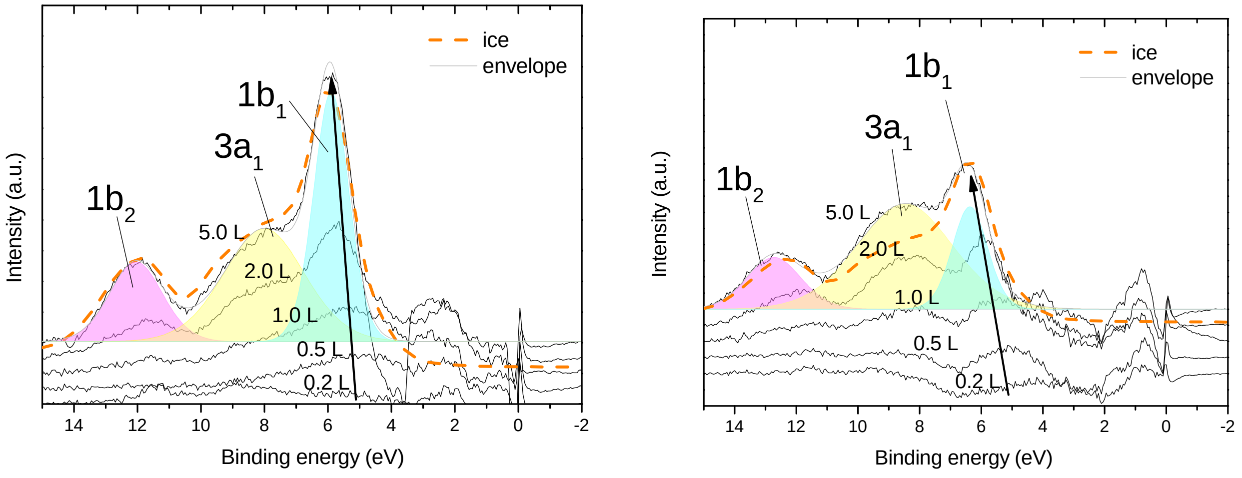

(a) **(b)**

Figure 6.9.: Valence band difference spectra of Pt-(100) (a) and Pt-(111) (b) with increasing water adsorption. The shaded areas represent the molecular orbitals deconvolution of the 5 L spectra, while the gray line is their resulting envelope. For comparison, the dashed orange line represents an intensity and BE adjusted ice spectrum. The dip in intensity at 3.5 eV in the Pt-(100) 5 L spectra is a measurement artifact.

the pronounce $1b_1$ lone pair orbital. The DOS seems to be smeared out across the $1b_1$ and $3a_1$ MOs. The first monolayer of water therefore undergoes a strong hybridization with the platinum d-states.

This already points to the fact that bonding to the platinum substrate is not in majority due to a sole interaction with the oxygen lone pair, because its valence band contribution is small at low coverages. This is in agreement with recent DFT studies by Blanco et al. showing that water behaves similarly on Pt(111) and Pt(100) and adsorbs almost horizontally on the surface [130]. This was further confirmed by X-ray absorption spectroscopy (XAS) measurements by Ogasawara et al. showing that the bonding mechanism to the platinum (111) surface is through the oxygen lone pair (Pt-O) as well as the Pt-HO group [131].

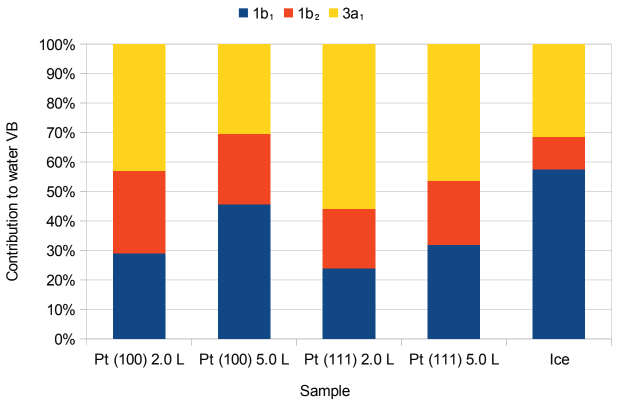

Figure 6.10.: Orbital contribution to the valence band DOS of adsorbed water on platinum and of a pure ice layer. Notice the rise in the $1b_1$ contribution as more water is adsorbed, due to an increased hydrogen-bridge bonding. This contribution is maximized for the pure ice.

Since the amount of adsorbed water is not equal after similar exposures, it is necessary to compare the MOs with roughly the same coverage. This means comparing Pt-(100) after 2 L with Pt-(111) after 5 L exposure. As can be seen in figure 6.10, their relative contribution is almost identical. Due to the similar behavior of the relative valence band intensities, it can be concluded that the bonding mechanism discussed above is also true for the platinum (100) surface. This is also supported by the fact, that Blanco at al. found the same adsorption energy of -27 kJ/mol for both surfaces [130].

6.5 Conclusion

Well defined platinum single crystalline surfaces were prepared. The electrochemical measurements were not sensitive enough to yield the correct active surface area of these crystal surfaces. However, the crystal direction could be identified by their specific desorption features. This is always complicated by the fact that the (100) and especially the (111) direction tend to form (110) facets after several CV cycles. (110) was therefore found to be the most stable surface in contact to the electrolyte.

Overvoltage measurements deviate strongly from values reported in literature. Here the formation of bubbles poses a major problem. Given these drawbacks the measurements still allow to be used as a reference point for other, polycrystalline samples.

PES measurements show that the d-band centers differ depending on the surface orientation and the technique that was employed. For surface sensitive He II measurements a general correlation between d-band center and catalytic activity can be revealed. Yet, the strong dependence on the excitation energy may pose questions to the general reliability of correlating the values determined from XPS for the d-band center with catalytic activity.

7 Platinum chemical vapor deposition

One route to synthesize platinum catalysts is via a chemical vapor deposition (CVD) process. Due to the low temperature stability of the tandem cell one goal was to reduce the necessary deposition temperature to 150 °C, which the cell could endure over a short period. The CVD process, due to its chemical nature, should yield a good adhesion of platinum catalysts with a high surface area. The initial buildup and preliminary experiments were done by Andreas Eva during his master thesis [132].

A strong influence upon the deposition parameters was found by the type of the reactive gas. Thermal precursor decomposition without reactive gas yielded poor results with only minor deposits. Alternatively oxygen and hydrogen gas were tested. Here different particle growth modes could be identified yielding distinctly different morphologies.

In order to evaluate the catalytic properties of these particles they were investigated by electrochemical techniques and compared to the results obtained for the platinum single crystals. A strong correlation was found for the dependence of the overvoltage on the active surface area [133].

7.1 Chamber setup

In figure 7.1 a schematic set-up of the CVD chamber is shown. The whole tubing was preheated to T_{pre} in order to prevent condensation of the precursor. The distances between precursor crucible and chamber were kept as small as possible. In contrast to most CVD setups, the carrier gas was not passed through the crucible but passed by it. Deposition rates are rather small which is advantageous since only thin layers or isolated particles were desired.

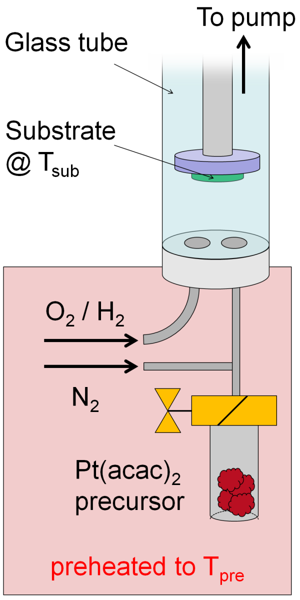

Figure 7.1.: Schematic illustration of the CVD chamber.

The substrate can be heated up to 500 °C and is placed directly over the precursor inlet. Reactive gases are introduced next to the precursor inlet without the addition of a shower head to facilitate mixing. The shower head was intentionally excluded because it poses an additional complication. It also has to be preheated to prevent premature nucleation and condensation.

As a substrate, titanium foil covered with a native oxide layer obtained from Alfa Aesar (99.5 %) was used. The precursor was 97 % pure platinum (II) acetylacetonate from Sigma-Aldrich.

7.2 Reactive gas and morphology

Significant differences could be identified between depositions carried out in oxygen and hydrogen. In oxygen a typical nucleation process on the surface is taking place. In contrast, in hydrogen gas the initial nucleation already

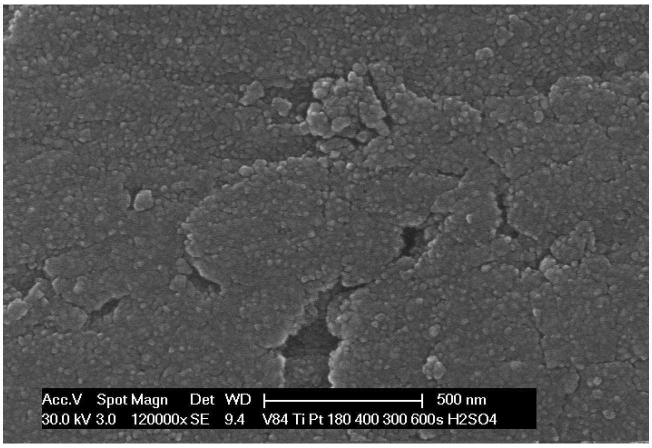

Figure 7.2.: Typical SEM image of a sample synthesized in oxygen atmosphere. The roughness stems from the titanium foil. The platinum overlayer forms a granular film. ($T_{sub} = 400$ °C)

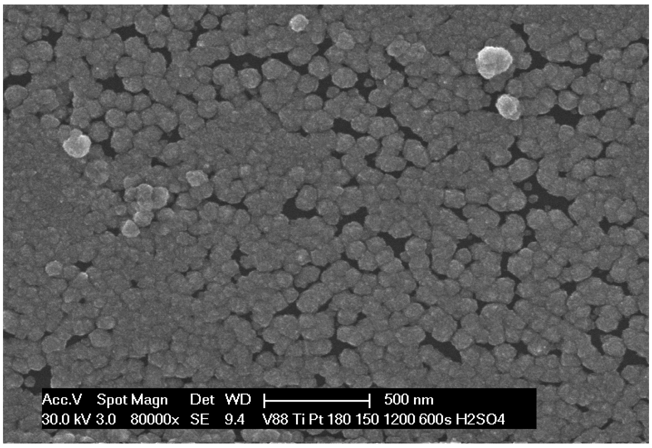

Figure 7.3.: Typical deposition in hydrogen atmosphere. The formation of stacked spheres is a result of gas phase nucleation. ($T_{sub} = 150$ °C)

commenced in the gas phase prior to deposition. A detailed study of these effects can be found in the corresponding publication [133], thus only the major results are discussed here.

In oxygen a high substrate temperature T_{sub} of 400 °C is necessary to achieve significant deposits. During deposition two growth modes can be identified for thin or thicker layers. The initial nucleation on the bare titania surface is characterized by a low growth rate and a more lateral than perpendicular growth. After this induction period the growth rate accelerates and results in a growth of columnar grains. These growth modes were also observed by Igumenov who in addition identified by means of XRD the columnar growth to be [200] oriented [134]. In figure 7.2 a typical scanning electron microscopy (SEM) image is shown for the deposition process in oxygen atmosphere. The film consists of many small intersecting grains exhibiting an edgy structure. The underlying roughness is determined by the titanium foil.

In hydrogen atmosphere the nucleation already begins in the gas phase, hence a spherical appearance of the particles is observed. This results in the formation of a porous layer consisting of stacked platinum spheres. In order to anchor these particles to the substrate, a substrate temperature of at least 150 °C is needed. In figure 7.3 a SEM image of a layer deposited at $T_{sub} = 150$ °C is shown. At higher substrate temperature (200 °C) the growth of the particles on the surface becomes dominant and transforms into the formation of a flat film.

7.3 Electrochemical measurements

The prepared samples were also investigated by electrochemical means. As for the single crystals, the active surface area, as well as the predominant surface directions were assessed by CV measurements. Finally also the overvoltage necessary for the HER was measured and correlated to the active surface area.

In oxygen atmosphere a majority of (111) facets was identified for thick films, which is in agreement with the proposed texture in [200] direction, since the [200] direction is terminated by octahedral (111) surfaces. Thinner films show both (100) and (110) facets indicative for a lot of edge and kinc sites.

The hydrogen samples exhibit no distinct majority orientation, but their overall active area is increased due to their porous nature.

A main result of these investigations is depicted in figure 7.4. Here a clear correlation between overvoltage and the surface charge density, i.e. the electrochemically active

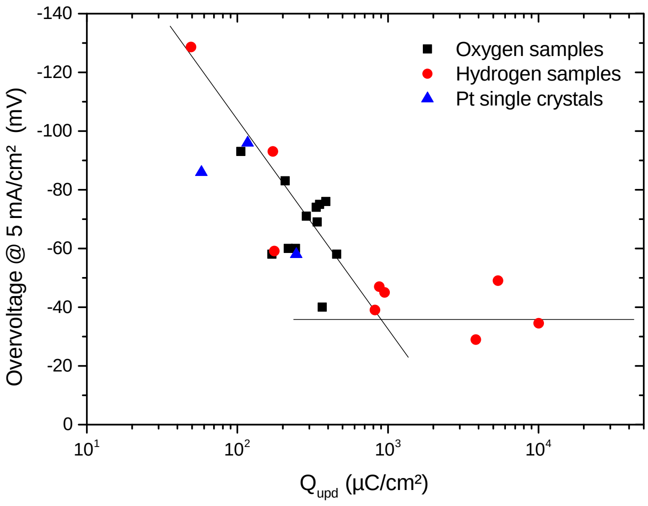

Figure 7.4.: Overvoltage as a function of active surface area. The semi-logarithmic correlation fits to a Butler-Volmer like process.

surface area, can be seen. The semi-logarithmic plot fits well to a Butler-Volmer type reaction mechanism, where the overvoltage is proportional to the logarithm of the inverse of the exchange current density, which in turn is proportional to the active surface area.

At 1000 μC/cm² the overvoltage saturates and becomes constant. This is most likely due to the diffusion limit of the reaction, i.e. the removal of gas bubbles becomes the limiting factor. The surface orientation seems to have little to no impact on the overvoltage as can be seen by the fact that samples synthesized in hydrogen and oxygen behave similar. Increasing the surface area is therefore an easy tool to decrease the voltage loss occurring at the platinum cathode.

7.4 Precursor temperature

An important aspect influencing the deposition process is the precursor temperature. Already in the master thesis of Andreas Eva, it was claimed that the small crucible outlet should lead to an almost equilibrium vapor pressure within the crucible. It is assumed that the growth rate is proportional to the amount of precursor in gas phase. It was not possible to directly prove this idea on the datasets existing at that point. Only a weak correlation between particle size and precursor temperature was found.

However, to prove the idea that the growth rate depends on the amount of precursor in the gas phase, it is assumed that in the crucible an equilibrium vapor pressure exists, which is governed by a simple Clausius-Clapeyron relationship. Due to the small opening in the needle valve the amount of precursor in the carrier gas flux is then proportional to the vapor pressure. A proportionality between growth rate $\dot{t}$ and the precursor pressure can therefore be expected. However, the growth rate is not directly accessible. Hence the active surface area was used as an indicator. Assuming a spherical nucleation, volume V and surface A are related by: $V \propto A^{3/2}$. In equation 7.1 the basic relationship is given. Hereby Q_{upd} denotes the active surface area obtained by cyclic voltammetry. The associated deposited volume is given by the volumetric growth rate $\dot{V}$ times the deposition time t. The volumetric growth rate depends on the precursor flux J_{pre} and thus finally also on the vapor pressure of the precursor p_{pre}.

$$Q_{\text{upd}}^{\frac{3}{2}} \propto \dot{V} \cdot t \propto J_{\text{pre}} \cdot t \propto p_{\text{pre}} \cdot t \tag{7.1}$$

In order to guarantee that all the precursor in the gas phase is deposited, the substrate temperature was set to 300 °C and a hydrogen flux of 500 sccm was used. Then the precursor temperature was varied from 140 to 200 °C, using a constant deposition time of 1200 s.

In order to correlate vapor pressure to the precursor temperature the Clausius-Clapeyron equation in its integral form is required. Assuming a negligible change in the heat of evaporation with temperature it is given by:

$$\ln \frac{p_2}{p_1} = \frac{\Delta H_m}{R} \cdot \left(\frac{1}{T_2} - \frac{1}{T_1} \right) \tag{7.2}$$

Combining equation 7.1 and 7.2 a plot of $\ln(Q_{\text{upd}}^{1.5})$ against $1/T_{\text{pre}}$ should yield a linear relationship. The corresponding fit is given in figure 7.5. The regression yields values which are in good agreement to the literature values [135]. From the slope the heat of sublimation can be

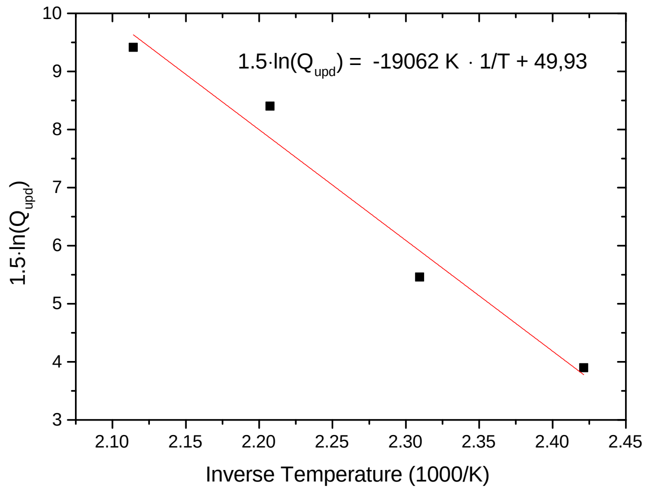

Figure 7.5.: Pseudo Clausius-Clapeyron plot correlating the surface area to the precursor temperature.

derived to be 105 ± 12 kJ/mol. Compared to the literature value of 129 ± 9 kJ/mol a remarkable agreement is found, considering the assumptions made [136].

The correlation found in figure 7.5 and the good agreement of the heat of sublimation conclusively shows that the amount of precursor in gas phase is governed by the ideal Clausius-Clapeyron law. An additional important result is that the deposition apparatus allows to perform a stationary process. Often it is encountered that sintering of the precursor leads to a decrease in its surface area and as a result the deposition rate is lowered. In the worst case the process becomes uncontrollable within one deposition, e.g. at the beginning there is a high deposition rate and at the end a low rate. From an experimentalists point of view this result was expected because it was possible to prepare more than 50 samples with one single crucible filling, demonstrating the stability of the process. Finally it is important to note that with this setup the deposition rate can be easily adjusted by changing the precursor temperature.

7.5 Photoelectrochemistry

Besides optimizing the HER, it is also necessary to evaluate the whole photoelectrochemical device under working conditions. For this reason, a high surface area platinum catalyst synthesized by CVD was combined with a tandem cell and a commercial ruthenium oxide counter electrode (15 g/m² Ru on titanium, Metachem), as indicated in figure 7.6.

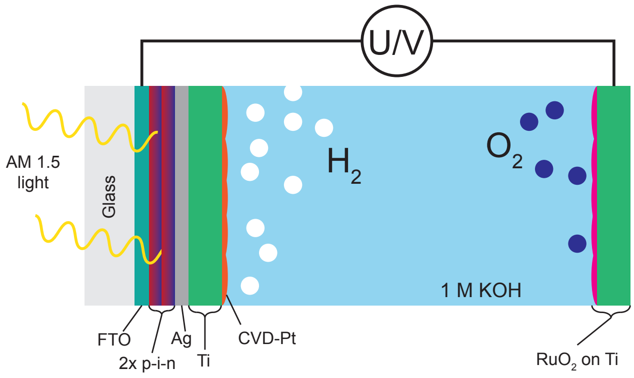

Figure 7.6.: Schematic illustration of the measurement setup. The standard tandem cell with a Ag back contact was connected to a high surface area platinum catalyst on titanium. The measurement was conducted in a two electrode setup with the commercial RuO_2 counter electrode.

For comparison the current-voltage (j-U) characteristic of the solid state tandem cell with the silver back contact was measured. In figure 7.7 its j-U-characteristic is shown. The current density reaches a short-circuit current of $j_{SC} = 7.94$ mA/cm² and an open-circuit voltage of $U_{OC} = 1.79$ V. Also contained in figure 7.7 is the power output of the tandem cell. It peaks at the maximum power point (MPP) at $P_{mpp} = 9.02$ mW/cm² with $U_{mpp} = 1.33$ V and $j_{mpp} = 6.78$ mA/cm², yielding a fill factor of 63 %.

From these values the electrical efficiency of the bare tandem cell can be calculated using equation 7.3. The obtained efficiency of the unmodified tandem cell is 9.02 %. This is already an indication that the cell itself is not one of the best ones, since efficiencies of up to 11 % were published [137]. Usually the breaking and cutting of these solar cells to smaller sizes introduces some defects that lower their performance.

$$\eta = \frac{I_{mpp} \cdot U_{mpp}}{P_{solar}} = \frac{P_{mpp}}{1000\ \mathrm{W/m^2}} \tag{7.3}$$

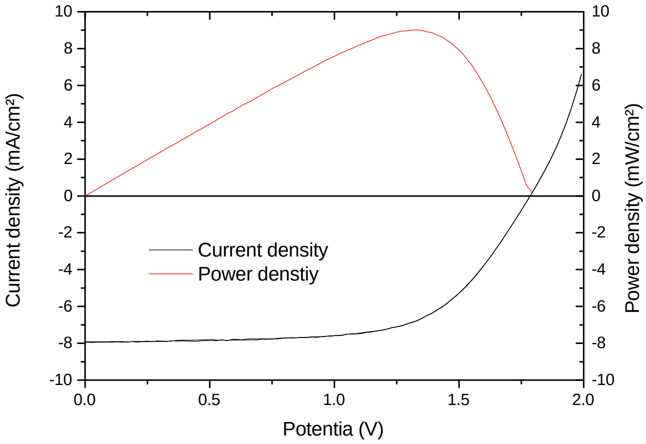

Figure 7.7.: Photovoltaic measurement of the tandem cell with silver back contact. Potential is measured between FTO front and silver back contact.

In figure 7.8 a photograph of the photoelectrochemical setup is shown. The shadow mask at the front has the same diameter as the o-ring exposing the cell to the electrolyte ensuring that the photoactive area is the same as the catalytically active area. The RuO_2 counter electrode is placed in 1 cm distance from the tandem cell. The tandem cell has a back contact made from silver which gives a good electronic contact to the titanium catalyst support. As light source a solar simulator from LOT-Quantum Design with AM 1.5 spectral composition was used. Both 1 M KOH and 1 M H_2SO_4 were tried as electrolytes.

In figure 7.9 CV curves with the two electrolytes are shown. Both reach a short-circuit current of 4.30 mA/cm². At higher cathodic overvoltage the saturation current density in KOH (7.81 mA/cm²) is slightly higher than in H_2SO_4 (7.14 mA/cm²). Both are close to the photovoltaic short-circuit current of 7.94 mA/cm². In the anodic regime the reverse reactions can be seen. Due to the large platinum surface this regime is dominated by the hydrogen desorption and HOR.

The solar-to-hydrogen efficiency η_{S2H} can be easily calculated using equation 7.4. It is given as the amount of energy stored in hydrogen divided by the energy irradiated on the photoelectrochemical cell. With $I_{SC} = 4.30$ mA/cm² a S2H efficiency of 5.29 % is calculated. As can be seen

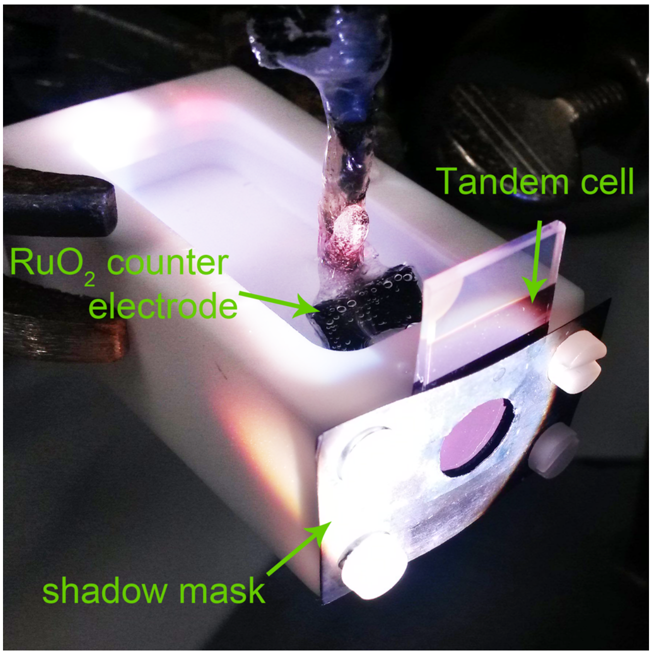

Figure 7.8.: Photograph of the photoelectrochemical cell immersed in the electrolyte. Illumination is from the front, the visible bubbles evolve at the counter electrode.

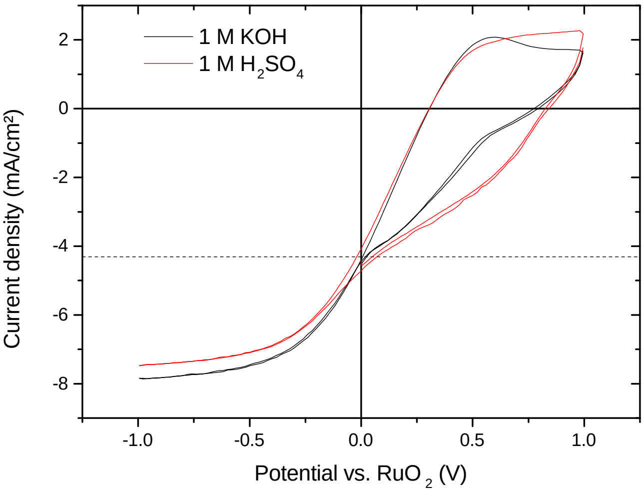

Figure 7.9.: CV obtained from the in operandi electrochemical setup with platinum electrode and a RuO_2 counter electrode. Without bias (at 0 V) the cell produced a current of 4.30 mA/cm², irrespective of the electrolyte.

in figure 7.9 the operating point is still within the onset of the current where a steep slope is present in the j-U-characteristic. Any change in catalytic overvoltages therefore has a strong impact on the S2H efficiency.

$$\eta_{\mathrm{S2H}} = \frac{1.23\,\mathrm{V} \cdot I_{SC}}{1000\,\mathrm{W/m^2}} \tag{7.4}$$

To further increase the efficiency it will be necessary to further optimize the tandem cell and the OER catalyst. As was seen in the CVD part in figure 7.4 the HER overvoltage is in the order of 40 mV at the given current densities. A further improvement is difficult and its influence onto the S2H will be minimal. Probably, a better tandem cell with a more steep j-V-characteristic will strongly improve the efficiency. At the same time degradation of the RuO_2 counter electrode must be excluded.

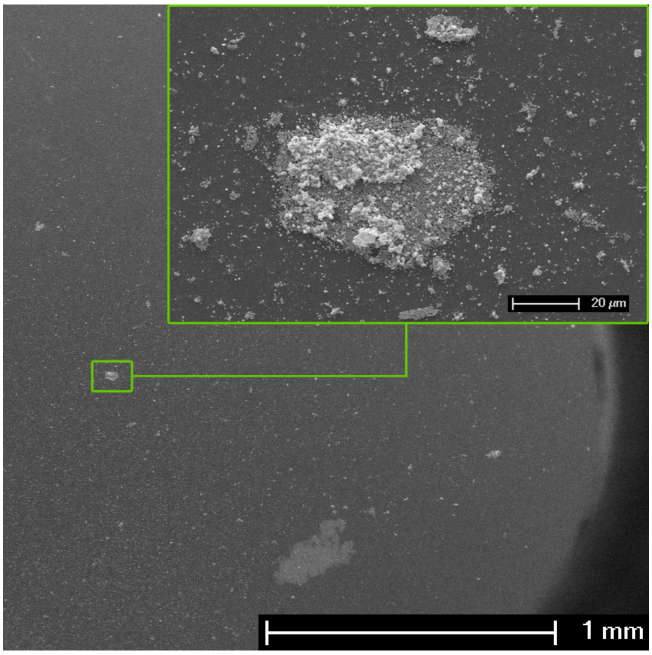

Figure 7.10.: SEM image showing the inhomogeneous nucleation of platinum on the tandem cell. The inset shows a magnification of an area with high coverage.

7.5.1 Chemical vapor deposition on tandem cells

It was already discussed that the ultimate goal is to deposit platinum directly onto the tandem cell. Since deposition at 150 °C onto titanium foil proved to be possible also experiments using the tandem cell were conducted.

As a first step, to protect the tandem cells from corrosion, a 5 nm thin titania layer was sputtered onto the surface. As concluded from the interface experiments in chapter 5.1 this should give good electronic contact to the the n^+-type contact layer of the tandem cell. Furthermore, the sputtered titania should be mostly chemically identical to the thin passivation layer found on the titanium sheet metal, that was typically used as the substrate material. Figure 7.10 shows the nucleation on the tandem cell at 150 °C substrate temperature. The nucleation is not homogeneous over the sample. In the inset an area is shown where the nucleation resembles the one observed on the titanium foil. It seems that the adhesion of the gas phase particles is suppressed on the tandem cell.

At first it was assumed that the substrate temperature was lower on the tandem cell than it is on the titanium foil. The thick glass substrate of the tandem cell with a low thermal conductivity could lead to a lower temperature at its front than the one that is measured by the thermocouple. For the 0.1 mm thin titanium foil this should not pose a problem. For the next experiments the substrate temperature was increased to 180 °C and even 200 °C. Yet, still no significant deposits were found.

Probably the temperature was not the critical parameter. Instead the surface termination of the titania might be decisive. The naturally oxidized titanium will be terminated with hydroxide groups, whereas the sputter deposited titania might still show no such termination. Immersion in water prior to deposition, or the addition of water vapor could prove beneficial for the deposition of the Pt-particles [138]. It was generally found that immersing of the titanium solely in solvents and water is not sufficient. Etching in concentrated H_2SO_4 improved the homogeneity of the deposits, however such a treatment is difficult to perform on the tandem cell due to its fragile nature. As an alternative atomic layer deposition of titania will also result in an hydroxide group terminated titania and might improve the deposition process.

7.6 Conclusion

In general the deposition of metallic platinum from $Pt(acac)_2$ proved to be feasible in hydrogen and in oxygen atmosphere. Whereas in oxygen a typical two-zone growth process was observed, in hydrogen the nucleation already initiates in the gas phase. The subsequent formation of a porous structure is especially interesting for catalysis in general and the HER in particular.

The growth process is easily predictable and shows a good reproducibility. Especially the fact that one filling of the crucible lasts for several depositions underlines the stability of the process as a whole. Furthermore, it was accomplished to correlate growth kinetics with the partial pressure of the precursor gas as predicted by the Clausius-Clapeyron equation.

Via CV measurements the active surface area was assessed and its importance for the HER overvoltage confirmed. Moreover the preferential surface directions were derived from the specific peaks in the CVs. Both agree to the morphology observed in the SEM images.

To evaluate the performance of the complete device a tandem cell was combined with a high surface area platinum catalyst. A S2H efficiency of 5.29 % was reached. Unfortunately the direct deposition of platinum onto the tandem cell proved to be more complicated than expected. It will be necessary to further investigate the cause of the insufficient deposition.

8 Clusters on surfaces

A free cluster consisting of a few atoms represents a very reactive species. (Naturally this means a lot of unknown effects that might occur as soon as free clusters land on the surface. Especially chemical reactions cannot be excluded a priori.) The chemical state of deposited clusters will be governed by three parameters in particular: The elemental composition of cluster and surface, as well as the kinetic energy of the cluster. The chemical composition will determine whether the materials tend to form an alloy or rather stay separate. Highly energetic clusters however might form alloys simply by being embedded into the substrate material.

The influence of the substrate is investigated by depositing platinum onto silver and onto SiO_2. These two materials represent two fundamentally different substrates. On the one hand silver, as a metallic material, forms alloys with minor amounts of platinum [139]. Additionally it possesses filled d-states that can interact with empty d-states of platinum. On the other hand, SiO_2 is a mostly ionic compound, without any d-states. Instead it is governed by strong sp-bonding. Alloying in this case is not to be expected.

Further the deposition technique will be explored exemplary by comparing e-beam evaporation with sputter deposition. Finally the knowledge gained from these fundamental studies will be transfered to mass selected clusters prepared via the cluster tool which was operated by Stephan Krähling and Benjamin Elger.

8.1 Influence of the substrate

Platinum was thermally evaporated onto a silver foil (99.9 % pure) and SiO_2 passivated n-type silicon. The silver foil was cleaned by Ar sputtering. The silicon dioxide was prepared as previously described in chapter 4. The XPS spectra of platinum evaporated onto silver are displayed in figure 8.1. The thickness was derived from the damping of the Ag 3d signal with respect to the Pt 4f line. IMFP were accounted for as described in chapter 3. The change in BE of the Pt $4f_{7/2}$ and Ag $3d_{3/2}$ lines are reproduced in figure 8.2 as a function of the platinum film thickness. Thick lines indicate the respective bulk binding energy values. In the Ag $3d_{5/2}$ line no significant chemical change is visible as it almost remains close to its initial bulk binding energy of 368.21 eV [140]. While the deposition progresses, the line moves to a slightly lower BE of 368.13 eV. The Pt $4f_{7/2}$ line exhibits the opposite trend. It shifts from 70.74 to 70.98 eV, hence approaching its bulk BE of 71.09 eV [141]. Concerning the shape of the Pt 4f line, a clear asymmetry is found even for thin layers. This is a result of the scattering of the photoelectrons with free electrons in the metallic valence band of the substrate [142]. For a small supported cluster typically a lower asymmetry is expected because they lack the free electrons [143]. To clarify this point, the Pt 4f spectra in figure 8.1 also includes the one observed for bulk Pt-(111) in red. Clearly, the cluster's spectrum is shifted to lower binding energy and exhibits an approximately 50 % increased FWHM of 1.53 eV. However, the asymmetry in the Pt 4f line is still clearly visible, a fact that will be explained in the following.

The initial shift to a lower binding energy than its bulk value is rather uncommon since it must be due to an initial state effect and cannot be explained by an increased

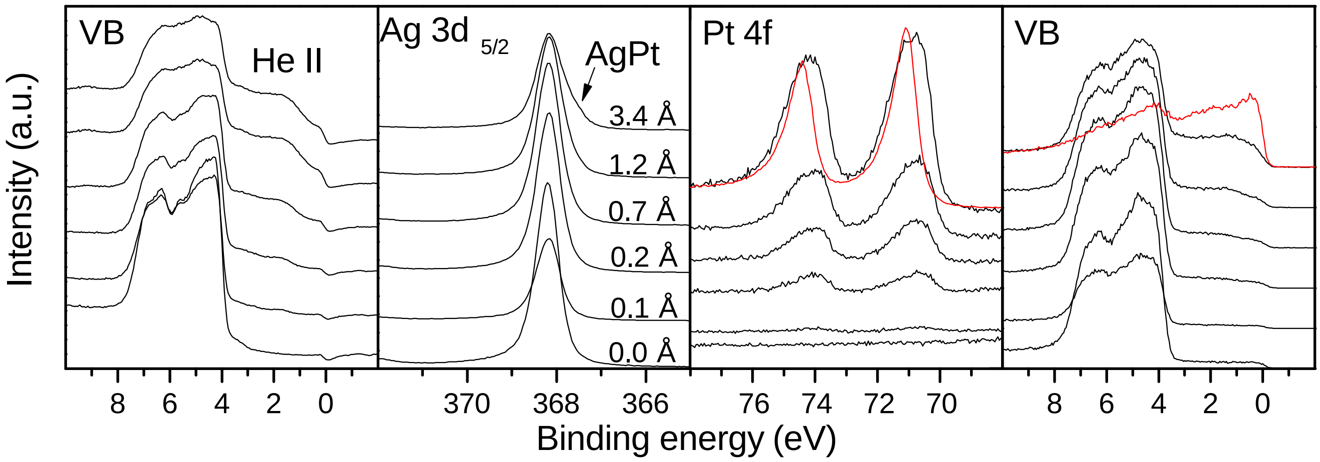

Figure 8.1.: Interface experiments of platinum evaporated on silver investigated by XPS & UPS. The platinum line shows an asymmetric shape as to be expected for metallic samples. In the UPS He II valence band, the mixing of the Pt and the Ag-d-states can be observed. In red the Pt 4f line of a Pt-(111) single crystal is added for comparison.

electron-hole interaction, i.e. a final state effect. Hence, the observed shift must have a chemical nature.

In the XPS valence band the almost constant 5s DOS of silver can be seen from 3 to 0 eV binding energy. The pronounced $4d^{10}$-states are located around 3 – 8 eV. As platinum is being deposited a rise in photoelectron emission intensity close to the Fermi level can be observed while simultaneously the silver d-states decrease in intensity. A trend that can be better seen in the more surface sensitive He II spectrum. This change in population of the valence band DOS is responsible for the shift of the Pt 4f core binding energy. An electron transfer from the silver to the platinum cluster leads to an increase in the d-band population of the platinum cluster. Scattering with these filled d-states is the reason for the asymmetric tail in the Pt 4f line. Simultaneously, the Ag $3d_{5/2}$ develops a shoulder at lower BE, indeed indicating en electron transfer from silver to platinum.

Effectively, platinum is reduced while silver is oxidized. The charge transfer can already be expected, when comparing the work function of silver of 4.6 eV with the one for platinum of 5.4 eV. This process has been widely observed in literature and occurs for supported clusters as well as for alloys [48, 144–146].

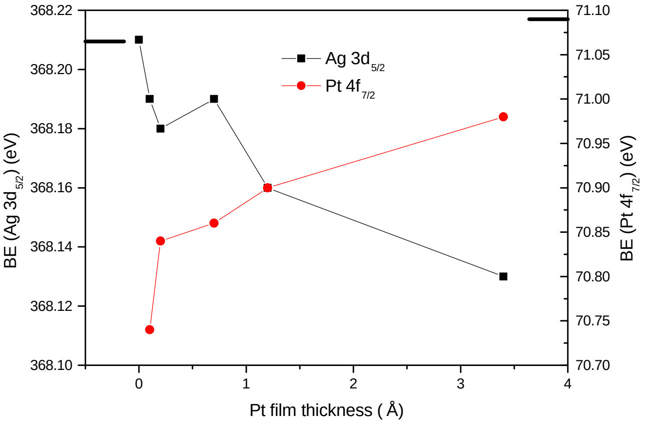

Figure 8.2.: Change in BE of the silver substrate and the platinum overlayer. Thick lines indicate bulk BEs.

The deposition of singular atoms or small clusters is therefore not significantly different from the formation of an alloy. For dilute alloys even lower BEs have been reported, e.g. for $Ag_{98.9}Pt_{1.1}$ a value of 70.2 eV is found for the Pt 4f line [147]. As more platinum is deposited, the platinum becomes chemically more pure platinum, hence its convergence to the bulk value.

When investigating the deposition on SiO_2 a different picture emerges. In figure 8.3 the uncorrected XPS spectra are reproduced. The first major difference that catches the eye is the strong shift to lower BE in the O 1s and Si 2p lines.

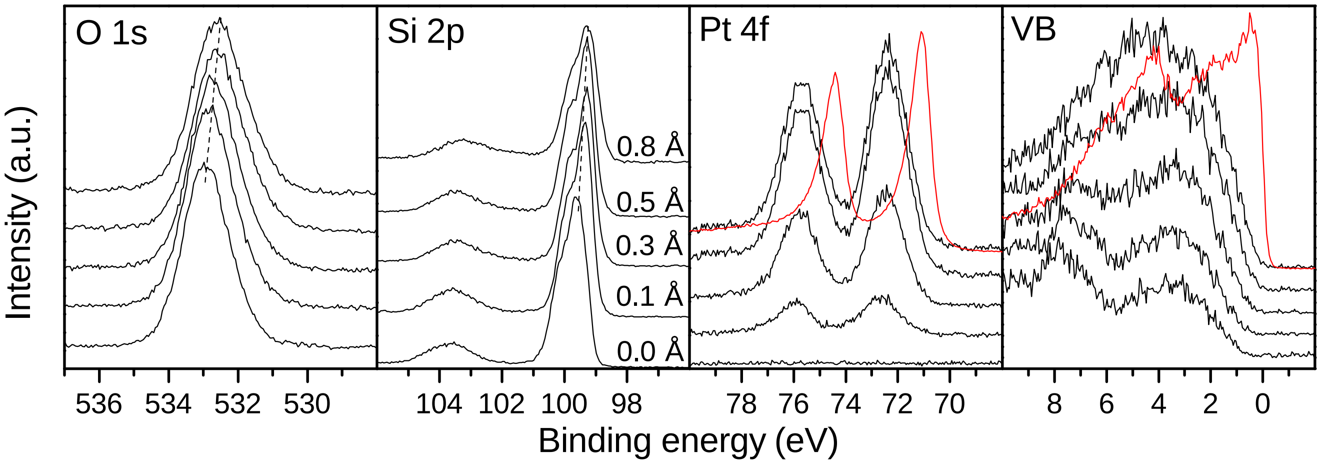

Figure 8.3.: Measured spectra of the electron beam evaporated platinum on SiO_2. Dashed lines indicated the core level shift. In red the Pt 4f line and VB of bulk Pt-(111) is shown as a reference.

In figure 8.4 the change in BE is depicted for the Si $2p_{3/2}$ and Pt $4f_{7/2}$ line. The O 1s line is not depicted as it moves analogous to the Si 2p line. This is a result of the formation of a Schottky barrier between the passivated silicon substrate and the platinum overlayer. Since the layer is still very thin, it is expected that the shift would increase with increasing deposition time.

During deposition a mild reduction of the SiO_2 layer can be observed, as the stoichiometry changes from $SiO_{1.8}$ to $SiO_{1.5}$ during the first three deposition cycles. This effect can be attributed to the high condensation energy of platinum atoms (5.852 eV/atom) when they coalescence into bigger clusters, thereby releasing molecular oxygen [148]. Consequently, also a higher amount of sub-oxides with oxidation states below +4 is found in the Si 2p spectrum. The last scan shows a higher oxygen content only because the sample was exposed to UHV overnight

The Pt $4f_{7/2}$ line is located at the beginning at 72.65 eV, a value notably different from the one observed on silver, even though the layer thickness is comparable. Previous evaporation experiments revealed the same trend [149]. Additionally, the Pt 4f line is almost symmetrical compared to the previous experiment. Both factors indicate that in this case the platinum deposit is electronically decoupled from the substrate and no photoelectron scattering with metallic valence band electrons is possible. The valence band spectra further acknowledge this fact, as the DOS of the deposited Pt only starts to approach the Fermi level. The same trend has been observed for small mass selected clusters on SiO_2 [150]. The clusters are not yet in a metallic state, since the d-states are still not broad enough to reach the Fermi level. Also no s-states are visible at the Fermi level, however due to their low intensity this might be misleading. This is especially obvious when comparing the 0.8 Å layer with the bulk VB (in red), where clearly a lack of states close to the Fermi level can be observed. In contrast to the silver 4d-orbitals the O 2p orbital of SiO_2 is energetically situated too low, hence no hybridization between the substrate and the cluster takes place.

These effects were already investigated in detail by Mason who established a rule of thumb, that also applies here [47]. If the substrate exhibits localized p- or d-bands that overlap with the clusters d-states, a shift to lower BE is to be expected. On weakly interacting substrates the opposite is true. Mason attributes the majority of the change in BE to the initial state effect, thus the clusters' chemical state. This observation was later confirmed in detail by Borman et al., who studied several transition metal clusters on graphite [55]. In Mason's research most of the experiments were done on conducting substrates, e.g. metal on metal or metal on conductive carbon. They obtained a positive shift of e.g. 1.4 eV for platinum embedded in amorphous

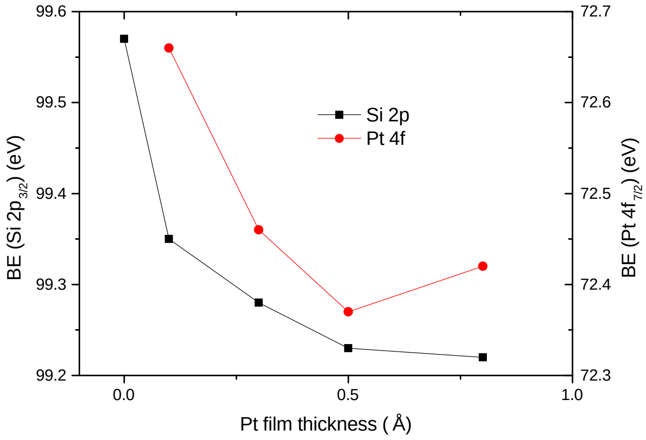

Figure 8.4.: Change in BE of the passivated silicon substrate and the platinum overlayer during e-beam evaporation of platinum on n-Si/SiO$_2$.

carbon (i.e. a Pt 4f BE of 72.5 eV). In the case of platinum on SiO$_2$ approximately the same value ($\approx$ 72.4 eV) was found, while it is shifted to even higher BEs for lower coverages. Since during evaporation both, the final state and chemical environment can be influenced, a clear distinction is not yet possible between initial and final state contribution.

For gold clusters supported on SiO$_2$ the final state effect was unambiguously identified, since it is directly dependent on the charge transfer rate from substrate to cluster and the consequent recombination of the core hole [151]. This also explains why the final state effect is negligible in the case of a silver substrate. There, a fast enough charge transfer is guaranteed, effectively marginalizing the final state contribution. However, this experiment highlights the challenge to separate initial and final state effects from each other, since it can not be concluded how much of the 1.3 eV shift can be attributed to final and how much to initial state effects.

8.2 Influence of the deposition technique

In the previous chapter platinum was evaporated. From the Maxwell Boltzmann energy density distribution function 8.1 the percentage of particles within a certain energy interval can be derived.

$$f(E) = \sqrt{\frac{4 \cdot E_n}{\pi(kT)^3}} \cdot \mathrm{e}^{-\frac{E_n}{kT}} \tag{8.1}$$

If we define, that for a gentle deposition process the kinetic energy should be less than 1 eV, the amount of particles with an energy higher than that can be calculated by numerical integration of equation 8.1 from 1 eV to infinity. The temperature of the evaporator is close to the melting point of platinum (1800 °C). Using these values the amount of platinum atoms with an energy higher than 1 eV is only about 0.5 %. We can therefore conclude that evaporation is in fact a gentle process, even when a material with a high melting point is used for deposition.

In contrast sputter deposition might lead to kinetic "energies that range from a few eV to several hundred eV" [152], making it a rough method that is prone to introduce defects into the substrate during the deposition process. Besides the metal atoms that are sputtered, the sputtering gas must also be considered. Ionized argon can lead to a preferential sputtering of oxygen atoms on oxide surfaces and thus leaves a "reduced" surface, i.e. oxygen is deprived [62, 153]. To see the influence of highly energetic particles on the electronic structure, the deposition of platinum on SiO$_2$ was reproduced, this time via sputter deposition.

In figure 8.5 the XPS spectra are shown. The deposition rate is higher than for the e-beam evaporation. As a consequence the thickness was more difficult to be controlled, hence the larger deposition steps. The BE of the core lines is again reproduced in figure 8.6. The substrate core lines behave analogous to the evaporation experiment, albeit the overall shifts are a little bit larger due to the thicker platinum layer. The Pt 4f line starts at a significantly lower BE of 71.53 eV, a value still higher than bulk platinum but at least 1 eV smaller than the values encountered during platinum evaporation.

Two reasons might lead to the decreased BE observed for Pt 4f. First, it could result from the increased thickness of the platinum layer. However, with a layer thickness of

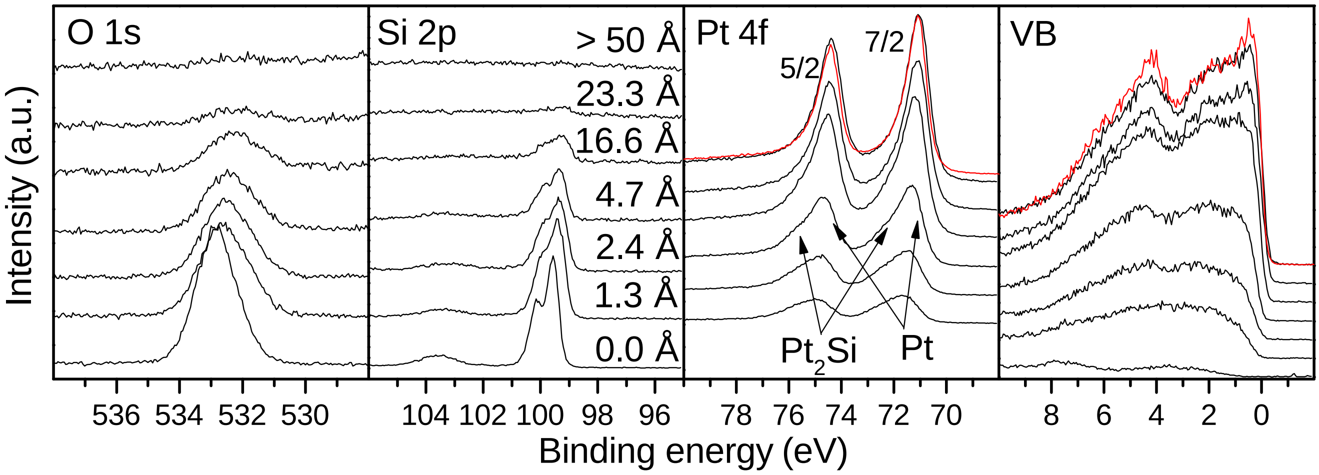

Figure 8.5.: Measured spectra of a sputter deposition of platinum onto SiO_2. Red spectra show the Pt 4f and VB of the Pt-(111) surface as a reference.

1.3 Å, it is well below the Pt-Pt bond length of 2.77 Å [56]. A covering film is therefore impossible and thus the chemical environment should not be significantly different solely because of a higher film thickness. The second possibility is a changed chemical environment due to the kinetic energy during deposition and the presence of the argon sputtering gas.

As was already discussed sputtering can lead to preferential sputtering and thus to depletion in oxygen content. In this case, the reducing effect can be directly observed by monitoring the O:Si ratio. It starts at 2.0 and immediately after the first deposition cycle drops to 1.1. It can be assumed that the loss of oxygen leads to a formation of a mixed Pt-SiO_x compound, which gradually approaches bulk platinum with increasing thickness. In fact, during the initial deposition steps the BE is close to a value found for Pt_2Si having BEs of 71.4 – 71.8 eV [96, 154]. Hence, it can be assumed that the reduction of the substrate in combination with the high kinetic energy during sputter deposition leads to the formation of a platinum silicide or silicate intermediate layer, that later on transforms into bulk platinum. An indication for this process can also be found in the Pt 4f line in figure 8.5. Up to a thickness of 4.7 Å a small shoulder at 71.5 eV can be found at the high BE side of the Pt 4f line. Unfortunately, this shoulder is not pronounced enough to warrant a precise deconvolution of the spectrum.

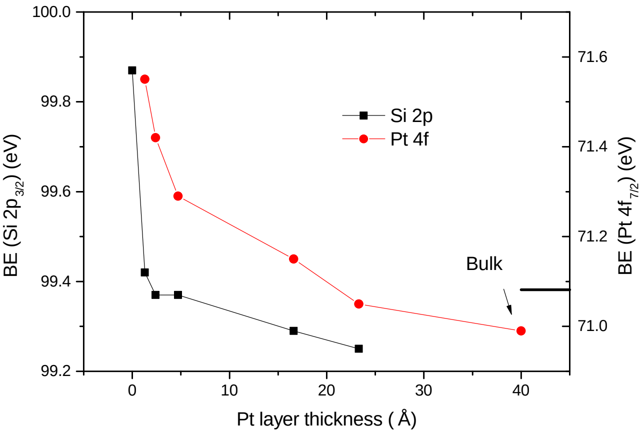

Figure 8.6.: Change in core level BE during sputter deposition.

The possible formation of a PtO species on the SiO_2 layer can not be excluded, as the typical platinum oxides (PtO, PtO_2 and $Pt(OH)_4$) are located around the position of this shoulder, beginning at 72.2 eV up to 74.4 eV [155–157]. However, the exact phase composition remains elusive.

8.3 Mass selected clusters

Clusters prepared in the cluster source have two major advantages compared to sputter and e-beam deposition techniques. First, the cluster size is known by filtering through a mass filter. Secondly, the kinetic energy can be controlled by adjusting the sample bias. High kinetic energies can

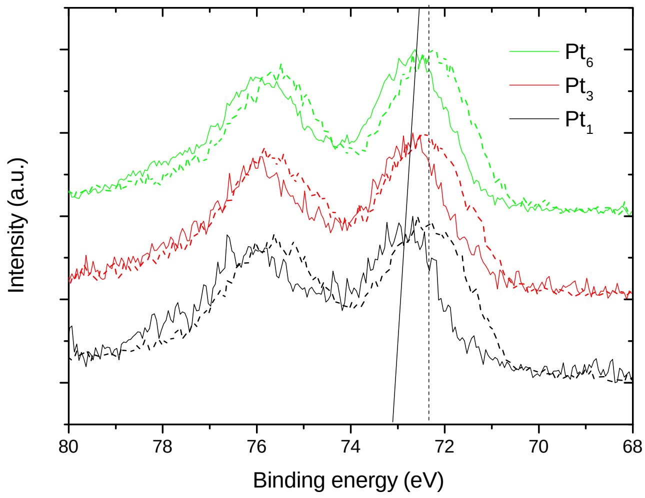

Figure 8.7.: XPS spectra of platinum clusters deposited on HOPG. Solid line spectra correspond to soft landed clusters on the surface, whereas dashed lines spectra were deposited with 16.6 eV/atom kinetic energy. Total platinum coverage was approximately 1 %ML for each deposition. The vertical lines highlight that for soft landed clusters the BE decreases with increasing cluster size.

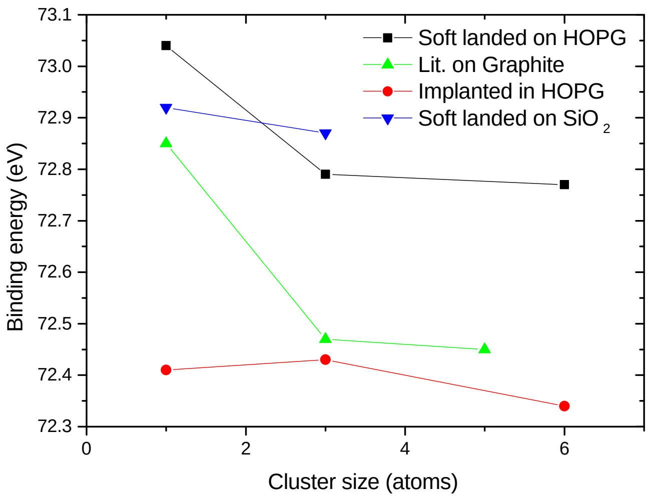

Figure 8.8.: Binding energy of the Pt 4f$_{7/2}$ line for soft landed (black) and implanted (red) clusters on HOPG. The green values were deposited on amorphous graphite [159]. Additionally soft landed clusters on SiO$_2$ are depicted (blue).

lead to implantation or dissociation of the clusters [158]. In figure 8.7 XPS spectra of Pt$_1$, Pt$_3$ and Pt$_6$ on highly oriented pyrolytic graphite (HOPG) are shown. One set of clusters was soft landed (solid line) on the surface, while the other (dashed line) was deposited with a kinetic energy of 16.6 eV/atom (e.g. 100 V bias voltage for Pt$_6$).

In general the clusters deposited without bias voltage show higher BEs and their BE value decreases with increasing size. The clusters deposited with bias voltage remain at the same, lower BE position independent of the cluster size. This can be understood by examining the chemical environment of the clusters. The soft landed clusters are located on top of the HOPG surface, thus they show a pronounced final state effect. For the samples with higher kinetic energy the clusters are partially embedded and therefore the hole of the photoelectron is additionally screened by the metallic substrate, leading to a lower BEs. An evaluation of the BEs is done in figure 8.8, including literature values for platinum clusters on amorphous graphite [159] and clusters on SiO$_2$. It is interesting to note that the literature values on amorphous graphite are situated in-between the soft-landed and implanted data points. This fits within the idea of shielding effects induced by the substrate, as amorphous carbon will exhibit a larger surface roughness than HOPG, which is atomically flat. Hence, the increased roughness provides a higher coordination and thus a better shielding of the core hole, however a complete shielding – as is the case for implanted clusters – is not observed.

These three measurements give an idea about the magnitude of the initial and final state effects present in these clusters. For soft landed clusters the lowest electronic shielding of the photoelectron hole can be expected since they are located on a saturated van der Waals surface. This is also the reason for the most pronounced change in BE when increasing the cluster size. The implanted clusters show no such definitive BE-size correlation. Here the BE remains at approximately 72.4 eV. The final state is screened by the increased electron density of the substrate. If we assume that the final state of the embedded cluster is completely negligible, the remaining 1.3 eV shift compared to bulk platinum (71.09 eV) is in fact due to the initial state and therefore the chemical environment of the platinum cluster. A value very close to the calculated value of Mason of 1.4 eV for platinum dissolved in carbon [47].

When comparing the BE of evaporated platinum on SiO_2 with the one observed for platinum clusters soft landed on HOPG the same trends are observed. As was stressed in the previous section, platinum evaporated on SiO_2 must have a particulate nature because the coverage is below one monolayer. The general similarities indicate that isolated platinum clusters on silicon dioxide might not be different from platinum on HOPG, meaning that in both cases only a small interaction with the substrate occurs.

To test this speculation atomic platinum was soft landed on a passivated silicon wafer. They show a Pt $4f_{7/2}$ BE of 72.92 eV, in good agreement with the one encountered for Pt_1 on HOPG of 73.03 eV. This is quite surprising given the fact that silicon dioxide is an insulator, thus a more pronounced final state effect would be expected. In addition, the high electronegativity of oxygen in the SiO_2 substrate also seems to have little impact on the clusters as the observed BEs are quite similar to the ones found for HOPG. The same observation was made by Eberhardt et al. who also identified a quite similar behavior on graphite and on SiO_2 [150, 159]. The small discrepancy between their values and the values presented here, can be attributed to the differently prepared substrates. In Eberhardts report amorphous carbon instead of HOPG was used, and their SiO_2 layer was a native oxide, whereas here a thermal oxide was grown.

To further identify the impact of the kinetic energy, Pt_3 clusters were deposited on SiO_2 with a kinetic energy of 100 eV. In figure 8.9 the Pt 4f lines of two coverages of Pt_3 clusters are depicted. The line splits into two components. The high BE component (green) Pt $4f_{7/2}$ line is situated at 72.87 and 72.90 eV, for 1 and 5 %ML respectively. The low BE components (red) are at 71.46 (1 %ML) and 71.42 eV (5 %ML). The spin orbit splitting remains at approximately 3.3 eV as for metallic platinum.

Both BEs have already been observed in the previous experiments. A BE of 71.4 eV was encountered in the sputter deposition experiments, whereas the high BE of 72.9 eV is identical to Pt_3 soft landed on HOPG and SiO_2. A fragmentation of the cluster can not be excluded, as a BE around 72.9 eV is observed for both, Pt_1 and Pt_3. However, both show a high BE. Hence, the low BE component correlates to the formation of platinum silicides, already found during sputter deposition. The question arises why these Pt_3 clusters exhibit the BE observed for soft landed clusters, although they were deposited with accelerating voltage.

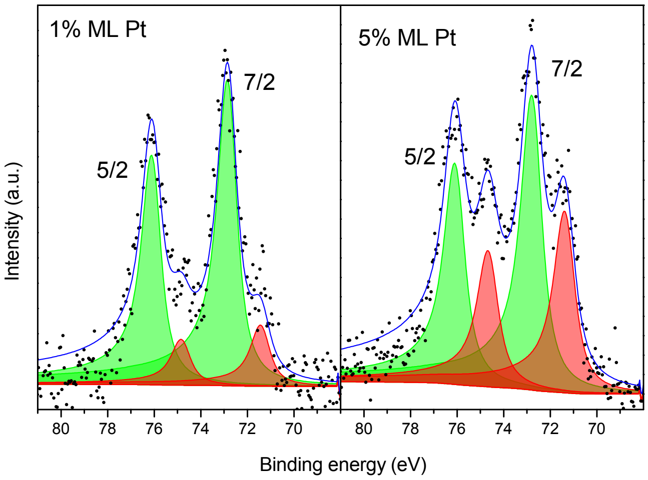

Figure 8.9.: 1 % and 5 % of a monolayer of Pt_3 clusters deposited on silicon dioxide. The Pt 4f line splits into a high (green) and a low (red) BE component.

In contrast to the deposition on HOPG most of the platinum clusters remain on the surface and are not implanted. This can intuitively be understood, recalling that the hardness of SiO_2 is significantly higher than for graphite. The high kinetic energy seems to enable two reaction pathways. Either they remain loosely coupled on the SiO_2, or they react to form platinum silicide or silicate. This process might be coupled with a fragmentation of the cluster, i.e. part of the clusters reacts and part of it is loosely coupled to the surface. As Pt_1 and Pt_3 differ only slightly in their BE (compare figure 8.8) the fragmentation cannot be excluded on basis of the given data.

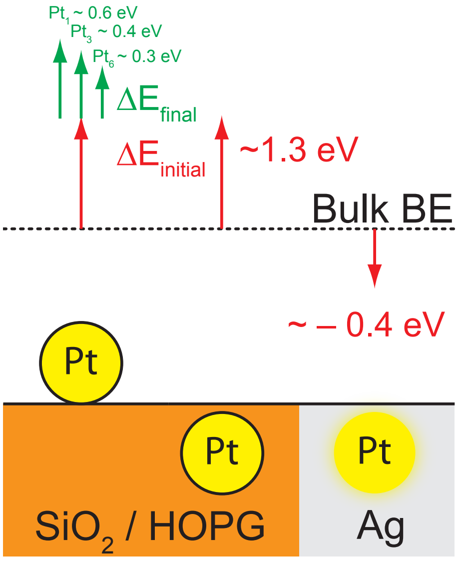

Figure 8.10.: Schematic Pt $4f_{7/2}$ BE shifts encountered for several combinations. Clusters on top side show initial and final state contribution, whereas for implanted clusters the final state is shielded. Alloying in the case of silver leads even to a negative initial (chemical) state shift.

8.4 Conclusion

With these experiments it was possible to confirm the theory of Mason [47], that the chemical state (size) of the cluster has the most pronounced impact on the BE. In addition, it was shown that for clusters up to a size of six atoms the initial state shifts the BEs of the clusters to higher values. In this context both, HOPG and SiO_2, generally behave as substrates, showing little interaction with the cluster. The similarity between both substrates indicates that the 1.3 eV shift in BE is in fact due to the intrinsic cluster size. This is in good agreement with the data published by Mason, who calculated a 1.4 eV shift for platinum dissolved in carbon from a thermodynamic point of view. Any observed additional shift is due to final state effects and is only observable for isolated clusters on weakly interacting surfaces. The scheme in figure 8.10 summarizes the possible scenarios.

For a cluster on the surface (left), initial state and final state are positive and shift the BE to higher values. Hereby, the final state contribution is strongly dependent on the cluster sizes, as can be inferred from figure 8.8. Implanted clusters (middle) only show the initial state contribution, since the final charged state is shielded by the substrate. The initial state itself does not (in this size range) strongly depend on the clusters size. Finally, on silver (right) it is unimportant whether the cluster was embedded or is at the surface, because platinum readily forms an alloy with silver. Hence, there is even a negative initial state shift with negligible final state contribution.

An important criteria influencing the chemical state of the cluster is its kinetic energy when being deposited. In agreement with evaporation and sputter deposition experiments it was possible to pinpoint the effect of the kinetic energy. High kinetic energies lead to an increased reactivity of the clusters that can result in the formation of platinum silicide, probably accompanied with a loss of oxygen.

9 Electrolyte adsorption

So far isolated clusters on clean surfaces were investigated. An important aspect for water splitting has been neglected, namely the interaction with the electrolyte. As was already mentioned in the introduction, it can be expected that clusters immersed in the electrolyte behave different than clusters in vacuum. In general the investigation of the solid-liquid interface by PES techniques is difficult due to the high vapor pressure of the electrolyte. Nowadays dedicated equipment like a high pressure XPS with differential pumping can access also these interfaces.

Here the approach differed by the fact that water was adsorbed at cryogenic temperatures from the gas phase. Although this leads to the formation of an ice-like layer that is not identical to liquid water, similar surface reactions might be observable.

This technique enables us to monitor changes in the substrate and the cluster simultaneously. Hence, charge transfers from the substrate or the catalyst in presence of water can directly be revealed.

Three types of substrates were tested. First, graphite was studied, which should behave like an inert substrate towards the adsorption of water. Second, indium tin oxide (ITO) was investigated, that can easily attach hydroxide groups since the hydroxide is thermodynamically favored over the oxide. And at last silicon, where deviating reports are found on its reactivity towards water. All samples were modified with platinum clusters to study the effect of the clusters on the substrates hydroxylation reaction and vice versa, the substrates impact on the clusters electronic configuration.

9.1 Metallic substrate (Graphite)

As a metallic and inert substrate HOPG obtained from SPL was employed. It is easily cleaned by adhesive tape liftoff followed by a fast introduction into the UHV environment. To suppress the diffusion of clusters on the surface, the sample was sputtered with Ar^+ at 500 V for 10 min [160].

Afterwards clusters were soft-landed with a size inbetween one and four atoms [161]. At this early stage, experiments with only a singular cluster size were not possible yet. Also the coverage was still low at only 0.008 %ML for the first and 0.016 %ML for the second sample.

In addition to the two cluster modified samples also a reference HOPG sample without platinum was investigated. The samples were subjected to water vapor at cryogenic temperatures at BESSY II as described in chapter 3.3.4. In figure 9.1 the valence band after stepwise water adsorption on the reference sample is shown. The valence band changes stepwise from the one for HOPG to the typical DOS observed for water. To clarify the process at small coverages, where the DOS is still dominated by the HOPG contribution, also difference spectra were constructed by subtracting the pure HOPG VB. The difference spectra show that already at 0.1 L coverage, mostly molecular water adsorption is occurring. This is evident by the three $1b_2$, $3a_1$ and $1b_1$ molecular orbitals, which indicate the presence of molecular water [162, 163]. In fact, when comparing the intensity of the $1b_2$ with the $3a_1$ orbital, water shows – as expected – the VB shape characteristic for ice [128].

During adsorption a shift of all molecular orbitals to higher binding energies is observed. This parallel shift of all components and also of the O 1s emission line is not due to a chemical composition change, but of a simple charging mechanisms resulting from the dielectric nature of water.

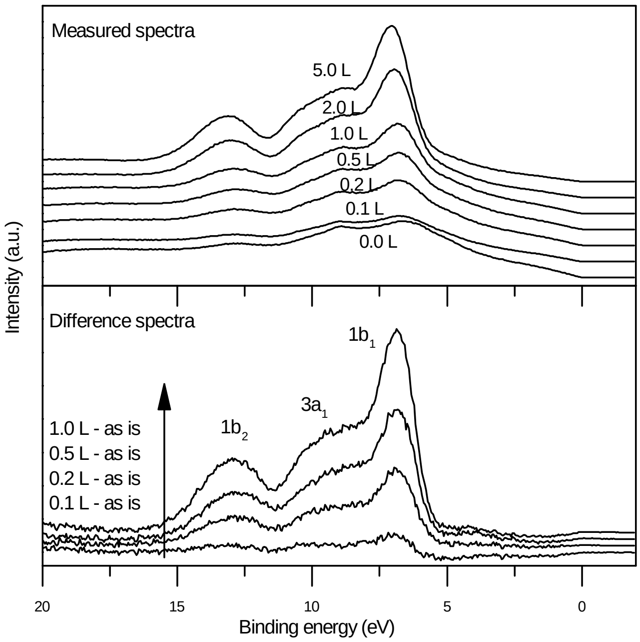

Figure 9.1.: Top: Stepwise water adsorption on HOPG. The valence band spectra transforms from the one for HOPG into the DOS of water. Bottom: The difference spectra clearly show that the MOs of water are already present at low coverages, highlighting the molecular water adsorption. Already at 0.1 L the $1b_2$ orbital characteristic for molecular water is present.

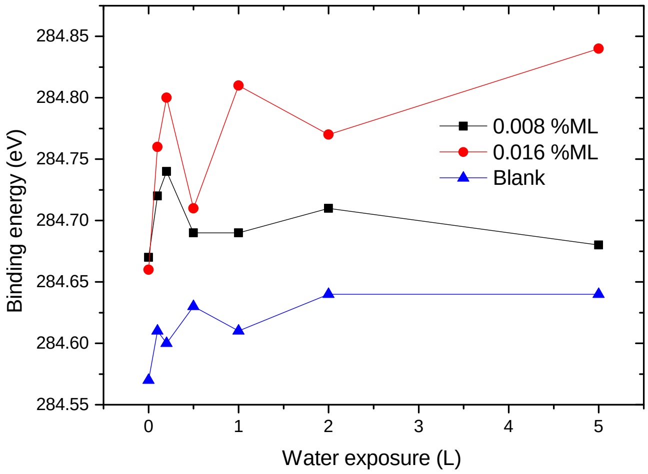

Figure 9.2.: Binding energy of the C 1s level of HOPG during stepwise water adsorption. The BE tends to shift to higher values as more water is adsorbed.

The adsorption of water manifests itself in a change in the C 1s binding energy of HOPG. In figure 9.2 the BE of the C 1s line is plotted against the amount of water exposure.

Recalling the metallic nature of HOPG it is surprising to find such a trend for the C 1s BE. The electrostatic interaction with the oxygen atoms is most likely to cause the observed shift, since HOPG is easily polarizable along the [0001] direction. Partial hydroxylation of the surface by water dissociation can be excluded. This can be concluded from the binding energies of the molecular orbitals of water upon adsorption. Beginning with the first adsorption step, molecular water is found as indicated by the presence of the $1b_2$ molecular orbital.

Besides the substrate, the effect of adsorbed water onto the catalyst is also of interest. The initial position of the Pt 4f line is approximately 71.5 eV. This value is lower than it was later observed for clusters of this size (chapter 8), even for the implanted ones. Most likely also clusters outside of the mass range of the quadrupole mass filter passed through (> 20 Pt atoms). The quadrupole mass filter was only used for recording the mass distribution spectra, but was turned off for the deposition on the sample.

During water adsorption no distinct change in the Pt 4f BE can be identified as seen in figure 9.3. Both samples scatter with no definite trend being discernible. The

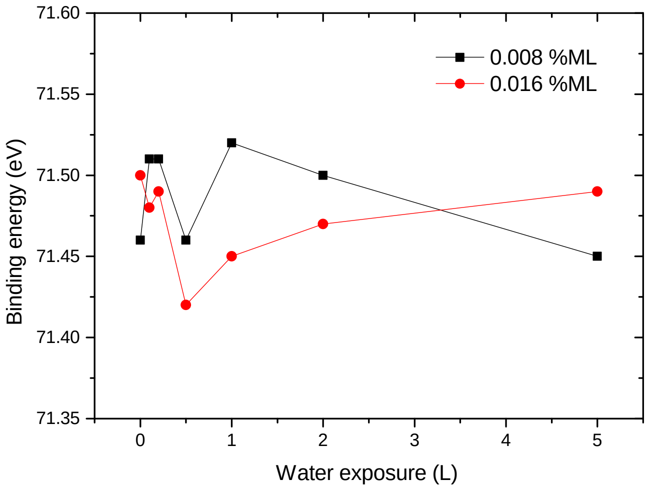

Figure 9.3.: BE of Pt 4f during water adsorption. No clear trend is visible.

Pt 4f BE suggests a size of a few nanometers that might be already capable of developing metallic conductance and hence shield the influence of the surrounding water.

At the same time the metallic nature of the substrate may lead to the observed low BE. The Fermi level of the cluster seems to be therefore aligned with the substrate and the addition of water does not change this situation.

Whether the cluster itself or the metallic substrate is the reason for the stationary behavior of the Pt 4f line cannot be determined with certainty. An argument for the interaction with the substrate is the BE of the Pt 4f line that still indicates small particles. On the other hand, a change in BE is observed for the substrate but not for the platinum line.

The shifts in BE allow the derivation of an energetic band diagram displayed in figure 9.4. Representative for the platinum cluster, the Pt 5d and 6s valence band DOS are indicated. Their curved shape represents the finite number of 5d and 6s states localized at the interface, as no complete band is formed for the isolated clusters. Due to its limited size the cluster is not yet fully metallic and the 5d states lie below the Fermi level [150]. Besides a small polarization of the HOPG, the energy diagram does not change during water adsorption. Since the Pt 4f line remains at its initial position we expect the same for the Pt 5d molecular orbitals.

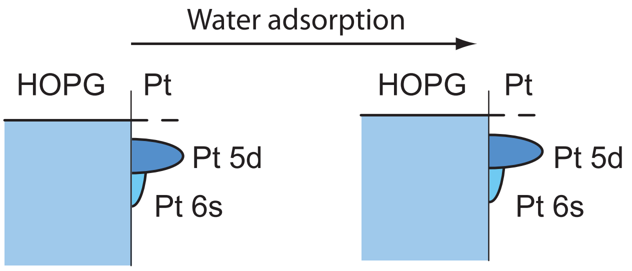

Figure 9.4.: Schematic band diagram before and after water adsorption. The stationery behavior of the Pt 4f line leads to an unchanged Pt 5d orbital position. The finite size of the 5d-states is consequence of the cluster size.

The lack of a shift in the Pt 4f line has another important implication. A change of the Pt 4f BE should also be expected if the platinum clusters directly interact with the surrounding water molecules. Since this is not observed there is only a small interaction between Pt clusters and the water layer.

9.1.1 Electrochemical performance

In order to assess the electrochemical performance of these platinum clusters deposited on HOPG, cyclovoltammogramms ware recoded in 0.1 M H_2SO_4. In figure 9.5a the obtained CV curves are shown. In comparison to the HOPG substrate material an increase in current density and onset potential can be observed. However, compared to a platinum sheet metal, or the thermodynamic HER onset, very high overvoltages can be identified. For these small clusters it can be expected that they are easily poisoned by adsorbed CO, considering their carbon support. However, the high overvoltage can also be a result of a changed reaction mechanism. In contrast to bulk platinum, in the anodic region no desorption features can be observed. It needs to be studied further whether this is due to the lack of an adsorption site for the small clusters, or if it is simply the limited resolution of the cyclovoltammogramm.

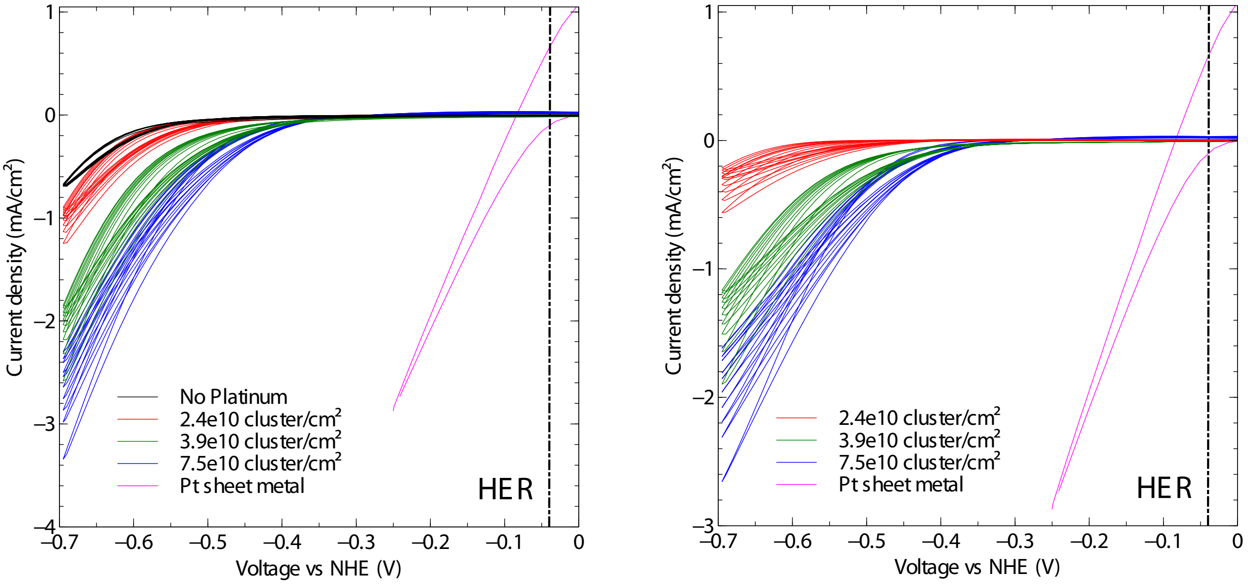

(a) **(b)**

Figure 9.5.: CV curves of platinum clusters on HOPG, the HOPG support and a platinum sheet metal electrode (a). The activity of the clusters after subtraction of the current originating from the substrate (b). (scan rate 50 mV/s)

In figure 9.5b the same curves are shown after removal of the HOPG background current. Here it can be seen that the achieved current scales approximately with the coverage. This is expected since the coverage is well below one monolayer.

For subsequent cycles always a reduction of the current density is observed. This shows that the particles are not stable on the surface. During hydrogen bubble formation they are most likely removed from the surface leading to a quick decrease in HER current.

The electrochemical activity of the platinum clusters is reduced compared to bulk platinum, mostly because of the low surface coverage and thus low electrochemically active surface area. Especially for such small coverages CO poisoning of the small clusters must be excluded for future experiments. It was purposely refrained from calculating mass activities, because the division by some nano-grams of platinum yields absurd high values.

9.2 Reactive substrate (ITO)

Indium tin oxide (ITO) and fluorine doped tin oxide (FTO) are well established support materials for electrodes. They are oxides and therefore stable under oxidizing conditions and show a good electrical conductivity.

In contrast to the HOPG support, ITO is not an inert interface in contact to water. In fact the surface is easily hydroxylated. This is no surprise given the fact that indium hydroxide is thermodynamically more stable than indium oxide [161].

The ITO surface was prepared via sputter annealing cycles in vacuum. The sputtering process leads to a preferential removal of oxygen from the ITO substrate, thus to the generation of oxygen vacancies. Large quantities of oxygen vacancies can lead to the transformation of Sn^{4+} to a Sn^{2+} species, acting as an acceptor defect that induces a depletion layer at the surface [164].

Platinum clusters were deposited onto the ITO surfaces under the same conditions as for HOPG. The initial position of the In $3d_{5/2}$ line after platinum deposition deviates

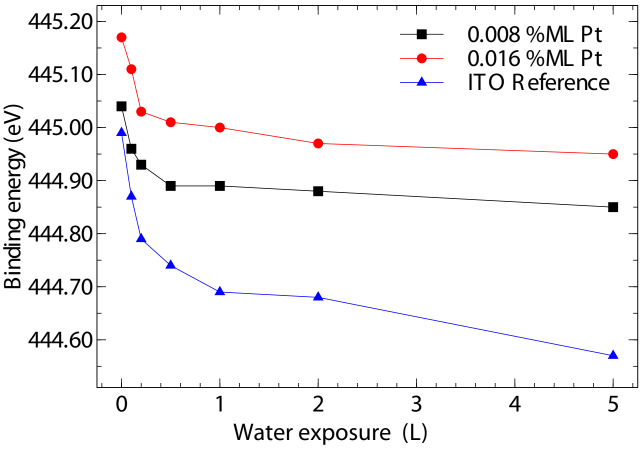

Figure 9.6.: In 3d BE of ITO during water adsorption. For all samples an increase in the depletion region is induced.

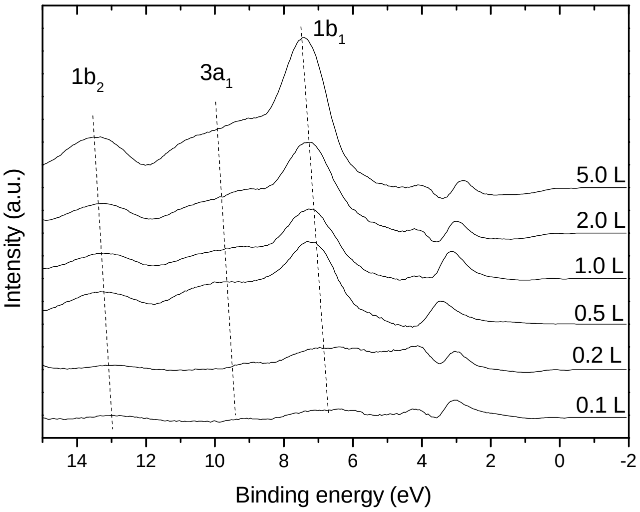

Figure 9.7.: Difference spectra of the VB of ITO during stepwise water adsorption.

by approximately 200 meV between the different samples. With respect to the a priory existent band bending in these samples this deviation in the starting condition is unavoidable. Hence, relative changes of the samples with respect to their initial configuration were investigated.

When these substrates were exposed to water vapor, an increased band bending could be observed. In figure 9.6 the change in the In 3d BE is plotted against the water dosage. For all samples the BE decreases with increasing water exposure. This decrease in BE corresponds to an upward band bending, i.e. an increase in the depletion zone.

The depletion zone is maximized for the reference sample without the addition of platinum clusters ($eV_{bb} \approx 0.4$ eV). It is the smallest for the sample with the highest amount of deposited platinum ($eV_{bb} \approx 0.2$ eV).

An evaluation of the stoichiometry reveals an increase in oxygen content during water adsorption. Considering that the water O 1s and the ITO O 1s deviate in BE, this increase in oxygen content can definitively be attributed to the oxygen contained in ITO and is not wrongly attributed to water. The increase in oxygen content is the highest with the largest amount of deposited platinum and the least for the reference sample.

This problem can be addressed by investigating the valence band during water adsorption. In figure 9.7 difference spectra for the VB are depicted. Up to 0.5 monolayer of coverage the 1b$_2$ molecular orbital of water is not observable. At low coverages water therefore chemisorbs forming hydroxide groups [165]. As the coverage increases the adsorption transforms into a non-dissociative process. However, this hydroxylation process fails to describe the change in Fermi level as no delocalized electrons are added or removed from the substrate.

The governing process responsible for the increased depletion zone must be the annihilation of oxygen vacancy donor sites. Removal of those donor sites will shift the surface Fermi level more mid-gap and produce the observed band bending. The corresponding reaction is shown in equation 9.1.

On samples with platinum we find that the formation of the depletion layer is impaired while the oxygen uptake is increased. There must be a competitive process that leads to an oxidation of the surface, resulting in an decrease in the depletion zone. Such a process is the oxidation of the Sn^{2+} defect states in presence of platinum (equation 9.2).

$$2e^- + V_O^{\bullet\bullet} + H_2O \rightarrow O_O + H_2 \tag{9.1}$$

$$V_O^{\bullet\bullet} + (Sn_{In}^{2+})' + H_2O \overset{\text{Pt}}{\rightarrow} O_O + H_2 + (Sn_{In}^{4+})^{\bullet} \tag{9.2}$$

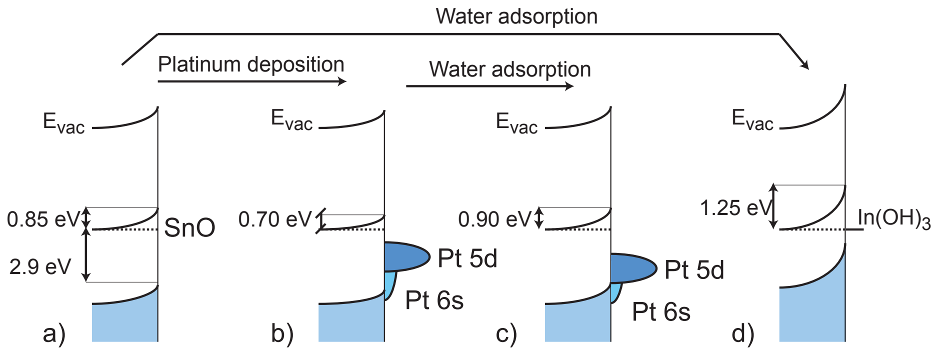

Figure 9.8.: Schematic band alignment of the ITO/Pt interface before and after water adsorption. The positive shift of the Pt 4f BE is mimicked by the DOS of the 5d and 6s states.

The total band bending is therefore reduced in the presence of platinum, as it channels the oxidation of vacancies with an associated removal of free electrons into an oxidation of the Sn^{2+} defects.

In figure 9.8 the competitive effects are schematically presented.

The hydroxylation of the surface also has an impact on the clusters. Even though the catalytic activity of platinum diminishes the overall band bending compared to the blank sample, the surface Fermi level is still lowered as is seen by the increased depletion zone. This leads to an electron transfer from the platinum cluster into the ITO substrate in order to compensate for the change in the surface Fermi level. This partial charge transfer can be observed in figure 9.9.

It is evident that the cluster is bound to the surface Fermi level of the support. Any change in the energetics of the substrate has a direct influence on the cluster. The energetic structure of the cluster not only depends on the substrate, but also on the electrolyte. The cluster therefore induces an inhomogeneous band alignment across the sample surface. This is the direct observation of the "pinch off" effect originally proposed by Nakato [42].

Furthermore its finite size does not allow it to shield these effects, as it would be the case for a bulk platinum layer. As a consequence the Pt 4f line shifts during water adsorption. The energetics before and after water adsorption are depicted in the band alignment in figure 9.8

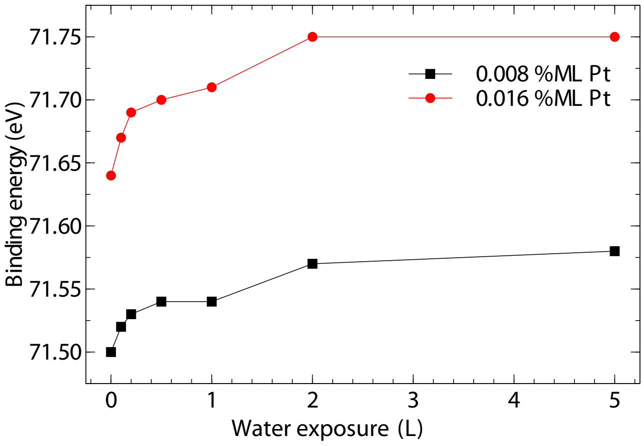

Figure 9.9.: Pt 4f BE during water adsorption. Platinum shows the inverse trend compared to the ITO substrate. Charge must be transfered from the cluster to the substrate, leaving a partial positive charge.

Here it was again assumed that the platinum Pt 5d orbitals change in accordance with the Pt 4f core line. While for the ITO layer an upward band bending is encountered due to the hydroxylation of the surface, the same defect leads to a positive BE shift of the platinum lines.

9.3 Adsorption experiments on passivated silicon

For silicon dioxide there is still a controversy whether it tends to form hydroxides or not. It is well established that silica gel can be used as a drying agent. The chemisorption of water can be directly observed by IR spectroscopy [166] and thermal desorption spectroscopy [167]. However, there are also reports of hydrophobic silica surfaces, if they are mostly free of defects [168].

The reactivity of these surfaces was again assessed by water adsorption from gas phase. In contrast to the previous experiments it was also tried to investigate the influence of the kinetic energy of the deposited particles.

In the first section soft landed platinum clusters will be discussed as well as their impact on the water adsorption. The second section deals with platinum clusters deposited with 100 eV kinetic energy.

9.3.1 Soft landed platinum atoms

Atomic platinum (Pt_1) was soft landed on silicon passivated with a 0.2 nm thick silicon dioxide layer [169]. The dioxide layer was chosen to be that thin, in order to monitor changes in the surface Fermi level of the substrates by observing the Si 2p signal, which is not prone to show chemical shifts.

One sample was decorated with atomic platinum with a coverage of 0.5 %ML, the other left blank as a reference. Subsequently water was adsorbed stepwise. In figure 9.10 the spectra of the stepwise adsorption are reproduced. The kinetic energy of the photoelectrons of Si 2p, of O 1s and of the valence band are almost identical, thus the same escape depth for the photoelectrons is realized for these spectra.

The O 1s spectra show the typical transition from the silicon dioxide position of 532.81 eV to the one for water. Again for thicker water layers charging leads to a shift of the O 1s peak to a higher BE of up to 536 eV. Comparing the O 1s spectra of the blank sample with the ones with platinum clusters, it is evident that the water adsorption progresses faster on the sample modified with platinum atoms.

The Si 2p line is accompanied by an oxide shoulder at higher BE. The Si $2p_{3/2}$ is situated at 99.93 eV when measured with 220 eV excitation energy. In-between the bulk Si 2p peak and the oxide peak the presence of not stoichiometric sub-oxides can be identified. The Si 2p line is completely damped after exposure to 600 L of water vapor. A completely covering ice layer was therefore deposited. After desorption the Si 2p line is restored.

The adsorption of water can also be identified in the valence band. After 600 L of exposure, a pure water spectrum is obtained. To reveal the small gradual changes in the valence band, difference spectra were constructed by subtracting the spectrum of the sample without adsorbate. These spectra are shown in figure 9.11.

The difference spectra reveal the presence of a hydroxyl species as well as molecular water. At 10 L the $1b_2$ orbital is diminished compared to the one at 100 L exposure. As was already discussed, this molecular orbital is representative for non-dissociated water, whereas the other two occur also for hydroxides [165]. The presence of hydroxides is confirmed by the 1π bonding orbital also arising at low coverages. After desorption the sample modified with platinum shows a remnant signal. Here still hydroxides are located on the surface, whereas they are completely removed for the blank sample.

Likewise, when monitoring the binding energies for the Si 2p core line the sample with platinum shows a shift to lower BE, while the blank sample returns to its initial position. These trends are depicted in figure 9.12.

A further effect that can be observed is the change in BE of the Pt 4f line. Here the opposite shift is occurring compared to the substrate material. As for the case of ITO, this can be interpreted as an electron back transfer from the platinum atom to the SiO_2 support material.

The general process therefore resembles the one observed for ITO, where a hydroxylation of the surface is observed. However, in contrast to ITO the SiO_2 surface is not strongly defective and also has no multivalent element like Sn. Thus, no hydroxylation of oxygen vacancies is to be expected that would lead to the observed depletion zone. Another mechanism must govern the defect formation on the SiO_2 surface.

A known defect that can act as an acceptor state is the nonbridging oxygen (NBO) Si-O· defect [170]. It is estab-

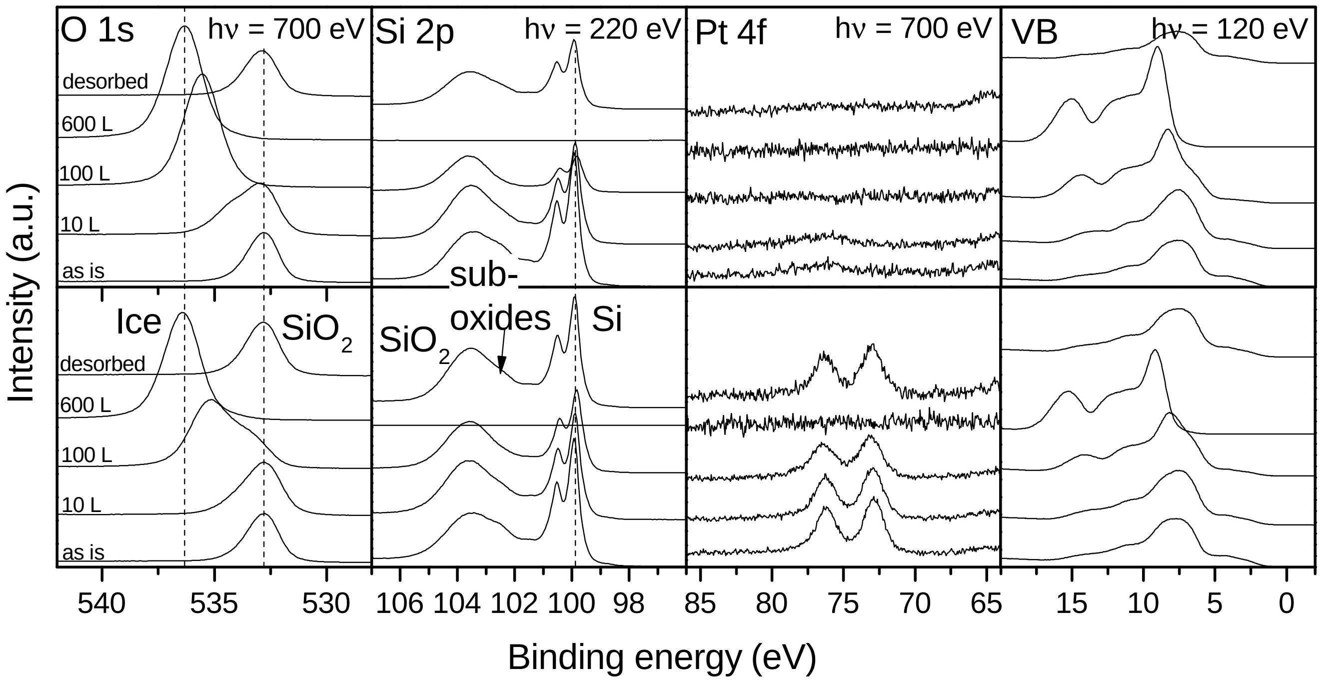

Figure 9.10.: Water adsorption on passivated silicon (top) and with deposited platinum atoms (bottom). hν defines the excitation energy. All spectra were recorded with almost the same kinetic energy of the photoelectron (except for Pt 4f).

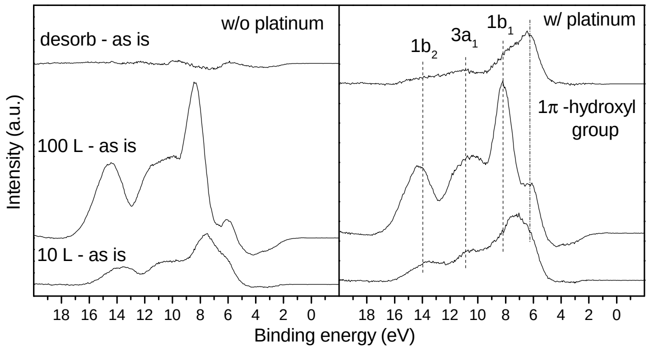

Figure 9.11.: Difference spectra of the VB. The 600 L spectra are omitted, because they only have a water contribution. With platinum atoms after desorption a residual water/hydroxide signal can be identified.

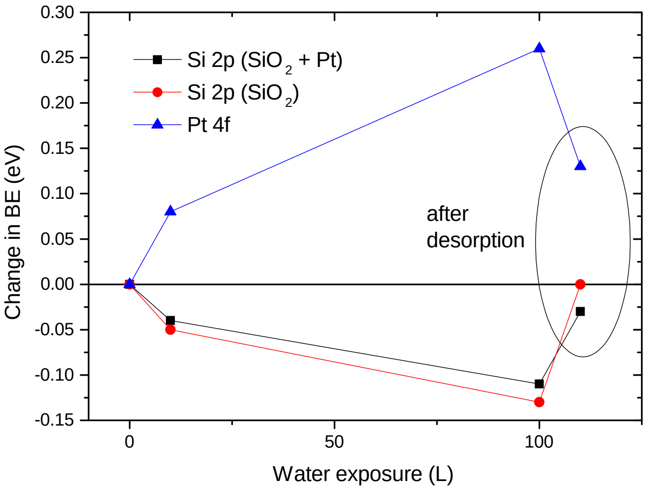

Figure 9.12.: Change in BE compared to the initial position.

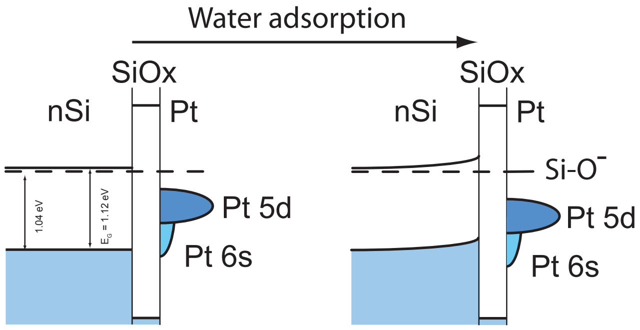

Figure 9.13.: Band diagram of passivated n-Si in contact to water. The nonbonding oxygen defect state leads to the formation of a depletion zone.

lished that this defect can be readily formed at a hydroxylated surface under illumination by breaking the OH-bond [171, 172]. The defects electron affinity is calculated to be around 5.3 eV - 5.8 eV, depending on the SiO_2-phase. An electron transfer from the Si substrate is therefore possible.

Equations 9.3 – 9.5 summarize the necessary reaction steps, which involve: 1. Hydroxylation of the surface. 2. Formation of the NBO-defect and 3. electron transfer from the Si support. For step 2 it is unclear if the hydrogen is released in its gaseous form, or remains trapped at the surface as some other chemical species.

$$\equiv \mathrm{Si{-}O{-}Si} \equiv + \mathrm{H_2O} \longrightarrow 2 \quad \equiv \mathrm{Si{-}OH} \tag{9.3}$$

$$\equiv \mathrm{Si{-}OH} \xrightarrow{h\nu} \equiv \mathrm{Si{-}O}\cdot + \tfrac{1}{2}\mathrm{H_2} \tag{9.4}$$

$$\mathrm{e}^- + \equiv \mathrm{Si{-}O}\cdot \longrightarrow \equiv \mathrm{Si{-}O}^- \tag{9.5}$$

The final band alignment with a hydroxylated surface is depicted in figure 9.13. The initial valence band offset of silicon was taken from the XPS measurements done in the DAISY-Fun laboratory.

Platinum seems to have little impact during the adsorption experiment. However, after desorption the presence of a hydroxide fingerprint on the platinum modified surface must be further explored. For the pure silicon dioxide we observe complete reversibility, thus the OH-groups are not stable at room temperature. With platinum these groups are suddenly stabilized.

One proposed mechanism is that the hydroxide group needs to be stabilized by surrounding water molecules [173]. The formation of the 1π bonding orbital upon water exposure confirms this assumption. When the stabilizing surrounding water molecules are desorbed also the hydroxide group decomposes in accordance with the reversible form of the hydroxylation in equation 9.3.

After platinum deposition the scenario changes and two possibilities could potentially explain the stabilization effect. For one, the deposition of platinum may remove the bridging oxygen leaving silicon surface atoms with dangling bonds which react with the adsorbed water (eq. 9.6)

$$\equiv \mathrm{Si}\cdot + \mathrm{H_2O} \longrightarrow \equiv \mathrm{Si{-}OH} + \tfrac{1}{2}\mathrm{H_2} \tag{9.6}$$

However, this hydroxylation reaction would strictly lead to the situation described in equation 9.3 and commence to decompose the hydroxide groups, if only point defects are considered.

The other possibility is that the platinum atoms supersede the surrounding water molecules and by their presence stabilize the hydroxide groups on the surface. The presence of vicinal hydroxides could also explain the positive shift of the Pt 4f line after desorption.

In related work Antonietti et al. studied the adsorption of gold atoms on SiO_2 [174]. They found that gold atoms preferentially adsorb at the NBO site, and not at regular Si-O or Si-OH surface sites. The same conclusion was reached for Ag clusters up to the size of four atoms [175]. Given that no new defects are induced during deposition, it can be assumed that this is also true for platinum, eq. 9.7.

$$\equiv \mathrm{Si{-}O}\cdot + \mathrm{Pt} \rightarrow \mathrm{Si{-}O{-}Pt} \tag{9.7}$$

Additionally, charged $\mathrm{Si{-}O{-}Au^-}$ and $\mathrm{Si{-}(OH)_2{-}Au^-}$ complexes are considered. These complexes however are less stable than the neutral Si—O—Au configuration. This interpretation is corroborated by Martinez et al. who found an electron back transfer from the charged Si—O$^-$ state into the substrate for a thin SiO_2 layer on Mo upon gold adsorption [176].

Unfortunately, no such DFT calculations exist for platinum on SiO_2. However, the experimental observations make it possible to postulate a slightly different reaction mechanism for Pt on SiO_2 upon water adsorption.

For gold the calculated formation energy difference between the Si—$(OH)_2$—Au$^-$ complex and the neutral Pt-O-Au complex is 0.8 eV. Considering the strong HO-Pt and O-Pt interaction (compare chapter 6 for single crystal experiments) it is reasonable to assume that in the case of platinum, the charged Si—$(OH)_2$—Pt$^-$ complex could be the stable compound. This would be in agreement with the observation of hydroxides on the surface after water desorption, as these are stabilized in the proximity of the platinum atom. Furthermore, the small remnant band bending in the silicon substrate is a result of the still charged Si—$(OH)_2$—Pt$^-$ defect state. Consequently, the back reaction of 9.3 is diminished.

9.3.2 Implanted clusters

Samples with partially implanted clusters were also investigated. The platinum deposition was carried out while employing an acceleration voltage of 100 V. The sample is the same Si/SiO_2 as was already discussed in the previous cluster chapter 8. There, a splitting of the Pt 4f line was observed in a high BE component that was identified as Pt_3 and a low BE component which is attributed to (PtSi).

Unfortunately during this measurement time at BESSY the pressure gauge in the adsorption chamber was defective, making the exact dosage of water vapor difficult. Nevertheless, stepwise adsorption was possible, although the exact exposure remains elusive. Therefore, the emphasis will be placed on comparing the as deposited sample with the one after desorption.

The adsorption process can most easily be monitored by the O 1s line. It clearly shifts from 533.1 eV (SiO_2) to 535.4 eV (H_2O) binding energy (figure 9.14). After water desorption the binding energy of the O 1s level is unchanged for the blank sample. Therefore, it can be assumed that the adsorption is mostly of molecular nature and a complete water desorption is possible. Investigation of the valence band at 100 eV excitation energy supports this assumption. Starting with the first adsorption steps the $1b_2$ orbital is visible confirming the presence of molecular water. After the desorption, no traces of water can be found in the valence band.

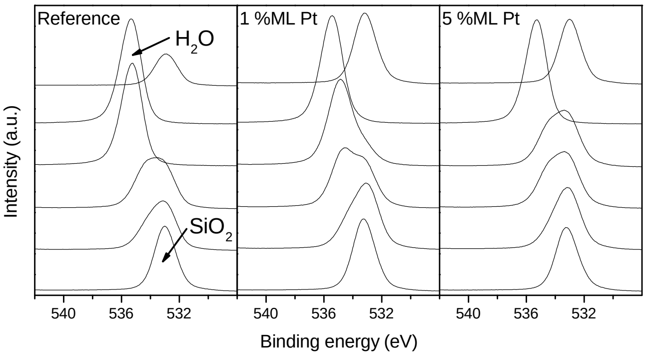

Figure 9.14.: Evolution of the O 1s signal upon water adsorption of the sample modified with 1 %ML, 5 %ML and a blank sample. The topmost spectrum is after desorption.

Concerning the BE after desorption, the blank sample returns to its initial position. However, there is a distinct shift in the binding energies of some core lines after the water desorption took place. Signals originating from the bulk of the sample, like Si 2p and the valence band excited with 700 eV, show no change in binding energy. On the other hand, the O 1s signal from the SiO_2 layer as well as the valence band excited with 100 eV photons show a distinct shift to lower binding energies. This is contrasted by the Pt 4f signal that shows a shift in opposite direction. It is important to note that these changes in the binding energy only occur on samples with deposited platinum clusters.

In figure 9.16 the Pt 4f spectra are reproduced. Again a platinum silicide and the Pt_3 cluster were identified. The spectrum is shown before adsorption and after water desorption. In general a peak shift to higher BE can be identified for both components. When examining the PtSi:Pt_3 ratio for the 5 %ML sample, a decrease can be observed

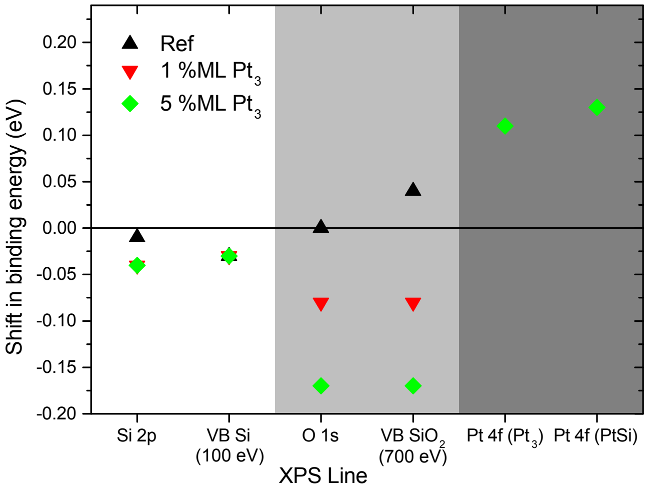

Figure 9.15.: Difference in BE before and after adsorption. The background color represents the origin of the signal. White is from the silicon substrate, light gray from the oxide passivation layer and dark gray the Pt deposit.

from 0.64 to 0.46. The 1 %ML sample shows a negligible change from 0.20 to 0.23. Here it must be noted that the low intensity makes a reliable fit difficult.

The decrease in PtSi can be explained by the oxidation of the PtSi species. It has been shown that platinum catalytically splits oxygen and as a result facilitates the oxidation of silicon [177]. Breaking of the Pt-Si bond consequently releases platinum in the form of a weakly coupled species. An equivalent process involving water is suggested in reaction 9.8.

$$PtSi + H_2O \longrightarrow Pt + Si{-}OH + \tfrac{1}{2}H_2 \qquad (9.8)$$

The overall observed shifts before and after desorption are reproduced in figure 9.15. The background coloration is related to the origin of these signals. White background BEs stem from the silicon substrate material, whereas light gray from the silicon dioxide passivation layer. In dark gray the Pt 4f signals are plotted for both PtSi and Pt_3. The change in peak position of the PtSi component of the 1 %ML sample is not given, since its contribution to the overall Pt 4f line is too small to warrant a definitive BE determination.

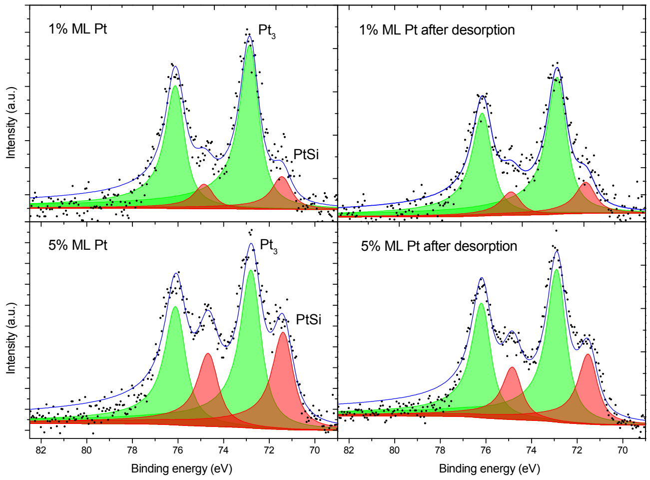

Figure 9.16.: Deconvolution of the Pt 4f signal of 1 %ML and 5 %ML Pt on SiO_x before and after water adsorption.

A nearly perfect reversibility is achieved for the silicon reference sample without platinum. Here no remnant shifts are observable for either substrate or the passivating oxide layer.

If platinum was deposited beforehand the situation changes. Still, the substrate Si 2p signal is unchanged after desorption. The silicon dioxide layer however shows a shift to lower BEs that also corresponds to the amount of deposited platinum. The platinum catalyst itself shifts to higher BE. Similar results were obtained for the soft landed platinum atoms in the previous section, albeit in lower magnitude.

Picking up the argument from the previous chapter, where it was concluded that either platinum or a defect associated with its deposition leads to a stabilization of the hydroxide group, the same reasoning should still apply here. Unfortunately, due to the thicker SiO_2 layer the difference spectra revealed no distinct new features of either hydroxide or water. If they were either not formed, or are just below the detection limit is impossible to judge. Referring to the changes in BE, it is almost certain that some chemical reaction must have occurred.

What is striking is that the relative peak shifts of the Pt 4f line is identical to the one observed for soft landed clusters of approximately 100 meV and the Si 2p line correlates with the amount of deposited platinum. Also the PtSi component shows the same shift. Since the kinetic energy was much higher, one would have expected more defects and as a consequence a larger peak shift. Since this is not observed here, it can be concluded that not the defects induced during deposition are the cause for the change in BE, but the presence of platinum itself. The stabilization of a charged $Si{-}(OH)_2{-}Pt_n^-$ species is therefore independent of the deposition energy and seems to be the most stable compound on the surface. It has to be noted that in this case Pt_3 was the deposited cluster and not atomic Pt. The acceptor state seems to be related to atomic Pt, its exact structure however remains illusive.

9.4 Conclusion

With regards to the results of the previous chapter 8 concerning single cluster on surfaces, it was possible to prove that indeed the presence of an electrolyte has a direct influence on the electronic structure of these clusters. In particular if the support material undergoes a chemical reaction with the electrolyte, even an inert cluster will react by redistributing its electronic configuration.

For both n-type substrates a depletion region is formed. In the case of ITO the oxidation of donor type oxygen vacancies leads to a more mid-gap surface Fermi level, thus introducing the depletion zone. For silicon oxide the process is more complicated, as it requires the formation of nonbridging oxygen defects on the hydroxylated surface, that in turn act as acceptor sites. The change of the surface Fermi level also influences the clusters, which is evident by a partial positive shift to higher BE.

These effects were observed for both, soft landed and implanted clusters. The introduction of more defects by increasing the kinetic energy of the clusters does not influence the extent of the charge redistribution in contact with water. Consequently, the acceptor type defect state is in fact stabilized thermodynamically and not a result of the kinetic energy of the platinum cluster upon deposition.

On metallic HOPG no influence of the water on the platinum catalyst can be identified. In this case the cluster seems to be shielded from the electrolyte by the metallic HOPG substrate.

10 Experimental setup

10.1 Mobile ultra-high vacuum transport chamber

In the scope of this thesis it was necessary to transfer samples between several UHV laboratories, namely the DArmstadt Integrated SYstem for FUNdamental research (DAISY-FUN) for substrate preparation, the cluster source for cluster deposition and the Solid Liquid Analysis System (SoLiAs) at BESSY II. Especially for a transport to Berlin a pumping system is required to hold the pressure bellow $1 \cdot 10^{-8}$ mbar for several days. A further requirement is portability and flexibility, while considering that especially UHV equipment becomes heavy very fast. In order to be attachable to all the laboratories, the height of the transport chamber must be adjustable, because all laboratories deviate in mounting height. In analogy to the naming of other UHV systems the chamber was named **DAISY-move**.

10.1.1 Chassis design

Several concepts were considered and it was finally decided to use a modified hand truck concept. In figure 10.1 the colored CAD drawings are shown. Since the chassis only rolls on two wheels it is easily rotatable even in a cramped laboratory environment. By mounting it on a linear actuator (olive green) the height can be adjusted. To further reduce the space necessary for turning and to protect the sensible UHV linear transfer (red), a folding mechanism was integrated to turn the whole chamber upright. In the horizontal configuration the chamber is attached to the UHV system (fig. 10.1a). When the chamber is lowered and turned upright the chamber is fixed by a latching mechanism and can safely be transported (fig. 10.1b).

In figure 10.2 a photograph of the finished chamber is shown. At the bottom the battery pack for the pressure gauge is visible. For practicability purposes the position of the pressure gauge and the sample stage were switched. For transportation additional grips were added at the side of the hand truck.

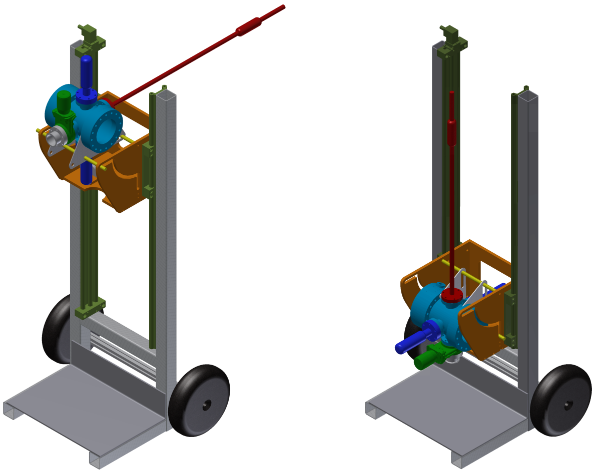
(a) (b)

Figure 10.1.: CAD drawings of the transfer chamber in horizontal configuration for sample transfer (a) and upright configuration for transportation (b).

10.1.2 Chamber design

In figure 10.3 the inside of the transfer chamber is illustrated. The transfer rod (red) and the valve (green) are mounted along the transfer axis. At the bottom the linear rotatable manipulator for the sample stage is mounted. The sample stage itself is located in the middle. At the backside the nonevaporable getter (NEG) pump is mounted. Finally at the top flange the pressure gauge can be attached. When attached to the system, up to eight samples can be stored in the integrated sample stage (middle). The stage is operated with a rotatable linear transfer (dark blue). Additionally the chamber was fitted with a hot cathode pressure gauge powered by a battery pack. With a plate valve (green) the chamber can be sealed and then be dis-

Figure 10.2.: Photograph of the completed DAISY-move transport chamber.

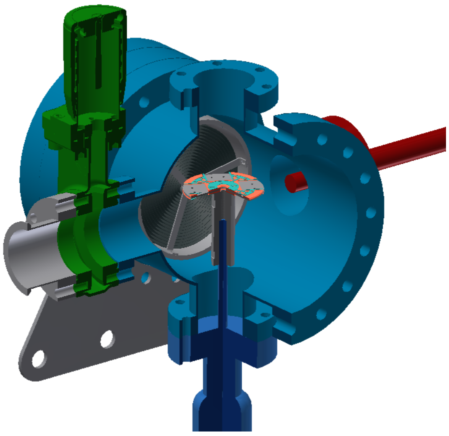

Figure 10.3.: Section view of the inside of the transport chamber consisting of: Transfer rod (red), valve (green), sample stage in the center and NEG pump at the backside.

connected from the system. In red the linear transfer rod with a stroke of 600 mm can be seen.

To keep the pressure during transport, pumping the chamber is a requisite. Ion getter pumps need a constant power supply, thus requiring a large battery pack. This would have a negative impact on the mobility. A pump based on a chemical getter material can solve this problem [178]. The getter "strip" was acquired from SAES getters and requires an initial thermal activation process [179]. Afterwards it adsorbs reactive gaseous species, except inert ones like argon or methane. The design of the pump itself was inspired by a publication from Firpo [180].

In contrast to Firpos publication we wanted to integrate the heating of the getter strip into our vacuum chamber, so it is not required to heat it up to 400 °C with outside heating tapes. In figure 10.4 a cross section view of our nonevaporable getter (NEG) pump is shown.

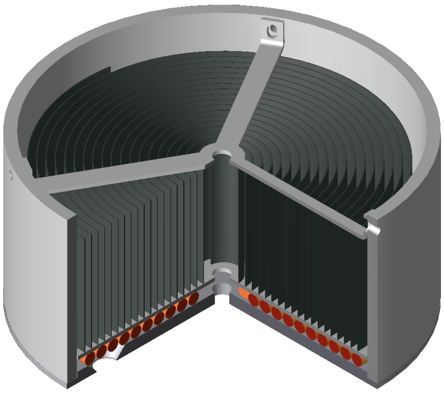

Figure 10.4.: Section view of the NEG pump. The heating wire (orange) is sandwiched between two metal plates below the getter material (dark gray).

The whole pump is separated from the flange by three spacer screws to minimize the heat transfer to the chamber. The heating wire (orange) is sandwiched between the back and an intermediate metal plate. On top of this, the getter material is wound as a spiral. To separate the getter strips individual turns from each other and to facilitate an improved heat transfer, a corrugated copper sheet metal is put in-between the getter material (not depicted). At the bottom side a K-type thermocouple is attached to monitor the temperature at the pump itself.

The pump was attached to a blank flange at the backside of the chamber. The front was fitted with CF100 window to monitor the sample transfer.

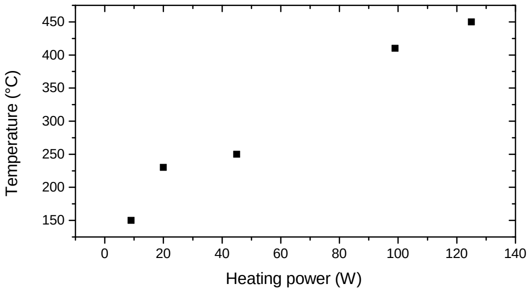

Figure 10.5.: Internal temperature at the getter pump as a function of heating power.

10.1.3 DAISY-move bake-out/activation

Prior to bake out, the electronics and the hot cathode gauge must be removed and the chamber has to be attached to the vacuum system. The valves connecting DAISY-move and the UHV system must be opened. An external pumping using a turbomolecular pump is required to remove desorbing species. The chamber is heated to 150 °C using external heating tapes, during this time the pressure rises. The chamber is kept at that temperature over night, thus degassing the chamber before activation. Then the internal heater is activated. Figure 10.5 shows the temperature measured by the internal thermocouple in dependence of heating power. The temperature is ramped up to 400 °C and kept there for approximately 60 min according to the product specification [181]. Afterwards the power is turned off and the chamber slowly cools down. When it reaches 200 °C, also the external chamber heating is turned off and the whole chamber cools to room temperature. Then the plate valve connecting the UHV system with the transport chamber is closed and the activation process is finished.

In figure 10.6 a bake-out cycle was monitored with a quadrupole mass spectrometer in order to identify the species in gas phase. While heating up the chamber, the release of hydrogen, nitrogen, oxygen and water can be observed. Hereby the oxygen signal is most likely a decomposition product of water. As soon as the oxygen signal starts to decrease, also a drop in the hydrogen signal can be seen. During the whole heating process water is released. However, the major contaminant by far is hydrogen gas. The exceptionally high hydrogen signal can be explained by the production process of the heating wire. The insulation granulate is processed in a hydrogen atmosphere, giving rise to the strong release of hydrogen during heating.

After turning off the heater the temperature starts to drop quickly. At the same time the hydrogen partial pressure decreases below the detection limit. At 140 min the hot-cathode pressure gauge was degassed while the chamber was still hot. This leads to a sharp increase in water and nitrogen partial pressures. At the end of the experiment water is still the main constituent and decreases slowly. The final cool down to room temperature then takes several hours. At the end the total pressure drops bellow the detection limit of the pressure gauge ($1 \cdot 10^{-10}$ mbar).

The strong rise in pressure during degassing of the pressure gauge reveals a general problem of the hot-cathode gauge. The filament always leads to the formation of new gaseous species that in return lead to a pressure increase [182]. Given this circumstance the pressure gauge was only activated in case of necessity and remained off most of the time.

10.2 In-situ electrochemistry cell

A general problem when combining electrochemistry with XPS measurements is the uncertainty on what happens dur-

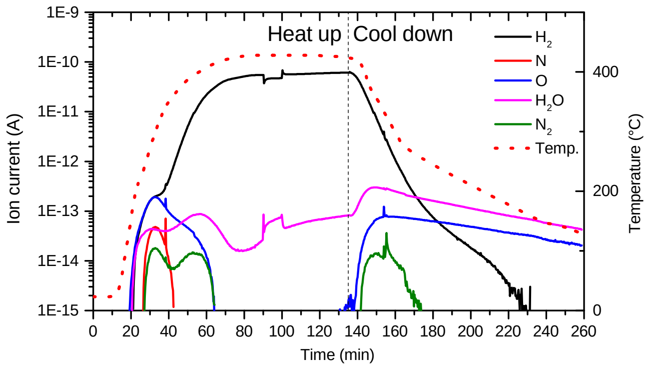

Figure 10.6.: Bake-out cycle monitored with quadrupole mass spectrometer. During warm up a lot of hydrogen gas is set free. During bake-out especially the degassing of the pressure gauge leads to a pressure increase.

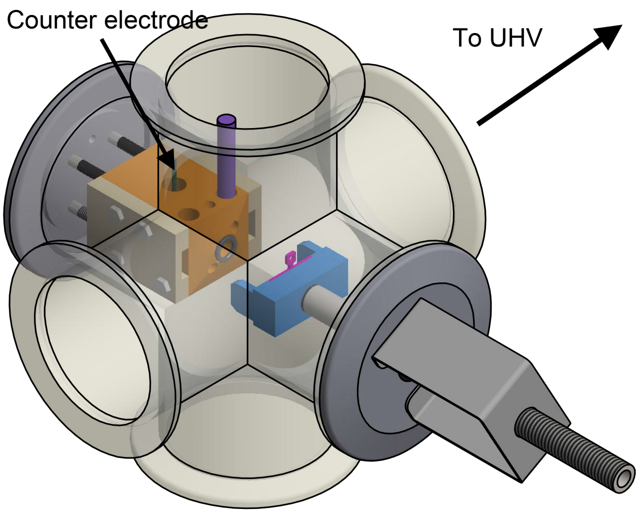

Figure 10.7.: CAD image of the electrochemical cell.

ing transport from the electrochemical cell into the XPS machine. For any chemical species detected in XPS it is a priori unknown whether this species was formed during electrochemistry or during transport. To circumvent this problem an integrated in situ cell was constructed. Flushed with argon gas, it be would possible to measure samples immersed in the electrolyte and then to transfer them in an inert gas atmosphere to the integrated system.

A rudimentary setup for etching samples in inert gas was already in place. It was placed within a KF50 glass double cross attached to the UHV system. Using pre-filled pipettes it was possible to drop acids onto the sample and to rinse them afterwards. However, electrochemical measurements were not available. With the new in-situ cell it is now possible to do standard electrochemical testing including the possibility to switch electrolytes or rinse the samples with water. All while avoiding contact to air.

In figure 10.7 the electrochemical cell (orange) within the glass cross is shown. The sample (magenta) is pressed against the O-ring and then the chamber is filled with electrolyte. The counter electrode is colored in green and the reference electrode in violet. To inject and remove electrolytes a small fitting is placed at the bottom of the cell. After measurements the cell is emptied and the sample retracted. By turning it by 90° it can be picked up by a linear manipulator and subsequently transfered into the UHV system. The whole setup is fitted in the same KF50 glass cross and flushed with argon to guarantee an inert gas atmosphere.

The tubing to interchange electrolytes stems from HPLC supplies. The cell is connected through a four-way distribution hub to four reservoirs. Three of them can be filled with electrolytes (typically acid, base and water) and one is the waste container. The three electrolyte containers are put under a slight argon overpressure (+ 0.3 bar), while the waste bottle is attached to a vacuum pump (- 1 bar). By opening one valve at a time, the electrolytes can either be injected or removed without breaking the inert gas atmosphere in the cell. In scheme 10.8 the connections are shown for clarification.

A further advantage of this cell is that the electrolytes can be flushed with argon in order to remove dissolved oxygen and that they are also stored under argon atmosphere. Especially for the hydrogen ad- and desorption measurements it is essential to have no dissolved oxygen residuals in the electrolyte, as they would give a parasitic cathodic background current.

This setup was used for all measurements in dark. Only photoactive measurements could not be done in this cell due to the lack of a light source.

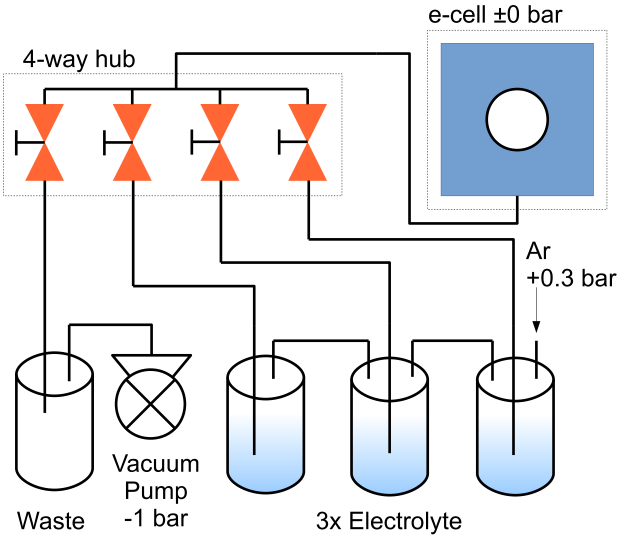

Figure 10.8.: Scheme of the tubing to inject and extract electrolytes. The cell itself is at atmospheric pressure and flushed with argon. Electrolytes are pressed with +0.3 bar into the cell. Extraction is done by a vacuum pump.

11 Conclusion and Outlook

To understand the solar to hydrogen efficiency of the photoelectrochemical cell, the interplay between solar cell, protective layer, catalyst and electrolyte was investigated. The electronic properties of small clusters were found to be influenced by their support as well as the electrolyte. Care must be taken when combining the individual parts to a working water splitting device.

To protect the tandem cell from the electrolyte titania was identified as an appropriate intermediate layer that also couples well to the platinum catalyst. The titania layer was prepared by sputter deposition. An inherent problem with this technique is the oxidation of the silicon substrate during the reactive sputtering process. For the model experiments on passivated n-silicon this was of no concern, since the semiconductor surface was already passivated with a silicon dioxide layer. However, Ziegler has shown that the voltage loss associated with charge transfer across the interfacial oxide layer can be detrimental [183]. The reduction of this interfacial oxide will be of great importance. As was shown, variation of the oxygen partial pressure in the sputter gas has a direct influence on the current-voltage characteristic. Seger et al. showed that a graded sputter deposition starting with titanium and transitioning into TiO_2 can improve the contact properties [184]. Otherwise, a step forward will be the switch to more gentle techniques, like atomic layer deposition [113].

Further, the deposition of platinum catalysts was investigated. Depending on the deposition technique alloying of the deposit with the substrate was observed. At the same time, the particle size effect complicates the normally straightforward interpretation of photoelectron spectra. It was shown that the observed binding energies strongly depend on the substrate and the kinetic energy during deposition. In this context it will be necessary to ensure "soft landing" conditions when investigating the catalytic performance of such clusters. It was shown, that the partial implantation can completely decouple the clusters from any interaction with the electrolyte.

In parallel, the synthesis of platinum catalysts by a CVD technique was further explored. This gentle deposition technique should enable the deposition of catalysts without damaging the support material. The process is now well characterized and yields stable results. So far however, mostly thick layers were synthesized and the process must be further developed.

The CVD deposition in hydrogen atmosphere seems promising to finally achieve spherical platinum particles with little size deviation while avoiding the introduction of defects in the substrate. From these experiments a clear correlation between the active surface area and the overvoltage can be derived. This correlation shows a Butler-Volmer like dependence. Hence, in order to reduce the overvoltage, a high surface area is necessary. This can most easily be achieved by further reducing the average size of the particles. Switching from forming gas to pure hydrogen should significantly increase the nucleation density and consequently reduce the average particle size. Alternatively, also the flux ratio between carrier gas and reactive gas can be adjusted in favor of the reactive gas to reduce the average particles size. An alternative way to increase the active surface area is to change the aspect ratio. For the growth of platinum on Hastelloy, needle shaped particles were obtained [185].

Alternatively, the CVD deposition can also be applied in order to coat existing particles with a thin platinum overlayer. As has been shown recently, a monolayer coverage of platinum enabled WC particles to exhibit the same HER performance as their pure Pt-counterpart, while reducing the amount of required precious metal [186, 187].

To evaluate the performance of these particles, model experiments on platinum single crystals were performed. Although these experiments proved to be more complicated than anticipated, as a result it was possible to correlate morphologies of polycrystalline CVD samples to their response in CV measurements at least qualitatively.

Also the validity of the d-band theory was tested for platinum single crystals. It emerged that the d-band center is not a sufficiently exact criterion to extrapolate activity in electrochemistry. Only some qualitative agreement between activity and d-band center was found. It was therefore also refrained from determining d-band centers for the CVD synthesized samples.

Finally, electrochemistry and semiconductor physics were combined when investigating the electronic properties of platinum clusters during water adsorption. It was clearly revealed that not the direct interaction between water and the cluster is decisive, but that chemical reactions occurring on the support's surface during water exposure affect the cluster.

Depending on the substrate it was found that platinum clusters behave differently. On inert HOPG no effect by the presence of platinum clusters was revealed. On ITO, a substrate easily hydroxylated, platinum clusters lead to a preferential oxidation of Sn^{2+} instead of an oxygen vacancies. On silicon dioxide however, neither trend could be definitively supported. Here, the hydroxylation is easily reversible as the hydroxides are stabilized by surrounding water molecules. For the non-reversible acceptor defect, a charged $Si{-}(OH)_2{-}Pt^-$ species was suggested.

In light of the already mentioned highly active Pt_8 cluster on CeO_2 [41], a closer investigation using adsorption experiments would be interesting. Based on DFT calculations the authors claim that the ceria support acts as an oxygen donor, facilitating the formation of adsorbed hydroxides on the Pt_8 catalyst. However, no spectroscopic evidence is given. In this thesis it was possible to directly monitor the formation of hydroxides in presence of atomic platinum on SiO_2. Probably, this approach would also be feasible in the case of ceria.

An important step missing is the electrochemical characterization of the small platinum particles. Usually the amount of particles was sufficient for PES, but not so for electrochemistry. As a next step forward, the electrochemical activity of those platinum particles must be assessed. Hereby it must be noted that SiO_2 passivated wafers are not an ideal substrate as the charge transfer across the oxide gives rise to a voltage loss. In addition, the charge carrier injection at the back contact of the silicon wafer must also be considered.

Therefore, it will be necessary to switch from passivated silicon to a more conductive substrate. The passivated silicon is an appropriate support for PES and adsorption experiments because its low defect density guarantees a direct insight into the cluster-semiconductor relationship. However, its bad conductivity combined with the necessity of a tunneling process through the passivation layer makes it unfavorable for electrochemical measurements.

As was already discussed in the chapter 5.1 titania was identified as a well adhering, conductive and electrochemically stable intermediate layer. For electrochemical measurements of small clusters it seems to be a good support material. In addition, titania itself has a negligible catalytic activity towards the HER making it possible to easily distinguish the catalyst activity from the activity of the titania support. Alternatively, HOPG is an unproblematic support as well. However, it could easily lead to CO poisoning of the small metal clusters and is for this reason not recommended for future experiments.

In this context, also the influence of the support material on the energetic position of the catalytic important Pt 5d states must be investigated. It would be interesting to analyze how the position of the 5d states, in dependence of the support, influences the overall catalytic activity.

12 Bibliography

[1] J. Tollefson. “Hydrogen vehicles: fuel of the future”. *Nature* 464.7293 (2010), pp. 1262–4.

[2] K. Rajeshwar, R. D. McConnell, and S. Licht. *Solar hydrogen generation*. Springer, 2008.

[3] C. A. Grimes, O. K. Varghese, and S. Ranjan. *Light, water, hydrogen: The solar generation of hydrogen by water photoelectrolysis*. New York: Springer, 2008.

[4] J. Guo and X. Chen. *Solar hydrogen generation*. McGraw-Hill Professional, 2011.

[5] R. Van de Krol and M. Grätzel. *Photoelectrochemical hydrogen production*. Springer, 2012.

[6] H.-J. Lewerenz and L. Peter, eds. *Photoelectrochemical Water Splitting. Materials, Processes and Architectures*. RSC Energy and Environment Series. The Royal Society of Chemistry, 2013, P001–468.

[7] J. J. Romm. *The hype about hydrogen: fact and fiction in the race to save the climate*. Island Press, 2004.

[8] J. Ziegler et al. “Photoelectrochemical and Photovoltaic Characteristics of Amorphous-Silicon-Based Tandem Cells as Photocathodes for Water Splitting”. *ChemPhysChem* 15.18 (2014), pp. 4026–4031.

[9] P. C. K. Vesborg, B. Seger, and I. Chorkendorff. “Recent Development in Hydrogen Evolution Reaction Catalysts and Their Practical Implementation”. *The Journal of Physical Chemistry Letters* 6.6 (2015). PMID: 26262851, pp. 951–957.

[10] E. Kemppainen et al. “Scalability and feasibility of photoelectrochemical H_2 evolution: the ultimate limit of Pt nanoparticle as an HER catalyst”. *Energy & Environmental Science* 8.10 (2015), pp. 2991–2999.

[11] V. Climent and J. M. Feliu. “Thirty years of platinum single crystal electrochemistry”. *Journal of Solid State Electrochemistry* 15.7 (2011), pp. 1297–1315.

[12] G. Rothenberg. “The Basics of Catalysis”. *Catalysis*. Wiley-VCH Verlag GmbH & Co. KGaA, 2008, pp. 39–75.

[13] S. A. Vilekar, I. Fishtik, and R. Datta. “Kinetics of the hydrogen electrode reaction”. *Journal of The Electrochemical Society* 157.7 (2010), B1040–B1050.

[14] S. Trasatti. “Work function, electronegativity, and electrochemical behaviour of metals: III. Electrolytic hydrogen evolution in acid solutions”. *Journal of Electroanalytical Chemistry and Interfacial Electrochemistry* 39.1 (1972), pp. 163–184.

[15] S. Trasatti. “Electronegativity, work function, and heat of adsorption of hydrogen on metals”. *Journal of the Chemical Society, Faraday Transactions 1: Physical Chemistry in Condensed Phases* 68 (1972), pp. 229–236.

[16] B. Hammer and J. Nørskov. “Electronic factors determining the reactivity of metal surfaces”. *Surface Science* 343.3 (1995), pp. 211–220.

[17] R. Hoffmann. *Solids and surfaces: a chemist’s view of bonding in extended structures*. VCH Publishers, 1988.

[18] N. M. Markovića et al. “Hydrogen electrochemistry on platinum low-index single-crystal surfaces in alkaline solution”. *J. Chem. Soc., Faraday Trans.* 92.20 (1996), pp. 3719–3725.

[19] S. Morin, H. Dumont, and B. Conway. “Evaluation of the effect of two-dimensional geometry of Pt single-crystal faces on the kinetics of UPD of H using impedance spectroscopy”. *Journal of Electroanalytical Chemistry* 412.1 (1996), pp. 39–52.

[20] S. Motoo and N. Furuya. “Electrochemistry of platinum single crystal surfaces: Part I. Structural change of the Pt (111) surface followed by an electrochemical method”. *Journal of electroanalytical chemistry and interfacial electrochemistry* 172.1 (1984), pp. 339–358.

[21] N. Furuya and S. Koide. “Hydrogen adsorption on platinum single-crystal surfaces”. *Surface science* 220.1 (1989), pp. 18–28.

[22] T. Roman and A. Groß. “Structure of water layers on hydrogen-covered Pt electrodes”. *Catalysis Today* 202 (2013). Electrocatalysis, pp. 183–190.

[23] J. Kitchin et al. “Modification of the surface electronic and chemical properties of Pt (111) by subsurface 3d transition metals”. *Journal of Chemical Physics* 120.21 (2004), pp. 10240–10246.

[24] B. Hammer and J. Norskov. “Why gold is the noblest of all the metals”. *Nature* 376.6537 (1995), pp. 238–240.

[25] A. Ruban et al. “Surface electronic structure and reactivity of transition and noble metals”. *Journal of Molecular Catalysis A: Chemical* 115.3 (1997), pp. 421–429.

[26] M. Jaksic. “Volcano plots along the Periodic table, their causes and consequences on electrocatalysis for hydrogen electrode reactions”. *Journal of New Materials for Electrochemical Systems* 3.2 (2000), pp. 153–168.

[27] J. M. Jakšić et al. “Volcanic periodicity plots along transition series, hypo-hyper-dd-interelectronic correlations and electrocatalysis for hydrogen electrode reactions”. *Macedonian Journal of Chemistry and Chemical Engineering* 30.1 (2011), pp. 3–18.

[28] D. Zhao, B. Yan, and B.-Q. Xu. “Proper alloying of Pt with underlying Ag nanoparticles leads to dramatic activity enhancement of Pt electrocatalyst”. *Electrochemistry Communications* 10.6 (2008), pp. 884–887.

[29] B. S. Mun et al. “A study of electronic structures of Pt_3M (M= Ti, V, Cr, Fe, Co, Ni) polycrystalline alloys with valence-band photoemission spectroscopy.” *The Journal of chemical physics* 123.20 (2005), pp. 204717–204717.

[30] T. Hofmann et al. “Using Photoelectron Spectroscopy and Quantum Mechanics to Determine d-Band Energies of Metals for Catalytic Applications”. *The Journal of Physical Chemistry C* 116.45 (2012), pp. 24016–24026.

[31] I. E. L. Stephens et al. “Understanding the electrocatalysis of oxygen reduction on platinum and its alloys”. *Energy & Environmental Science* 5.5 (2012), pp. 6744–6762.

[32] V. R. Stamenkovic et al. “Improved oxygen reduction activity on Pt_3Ni (111) via increased surface site availability”. *Science* 315.5811 (2007), pp. 493–497.

[33] D. Bimberg. “Der Zoo der Quantenpunkte”. *Physik Journal* 5.8/9 (2006), p. 43.

[34] E. Toyoda et al. “The d-band structure of Pt nanoclusters correlated with the catalytic activity for an oxygen reduction reaction”. *The Journal of Physical Chemistry C* 115.43 (2011), pp. 21236–21240.

[35] U. Heiz et al. “Catalytic oxidation of carbon monoxide on monodispersed platinum clusters: each atom counts”. *Journal of the American Chemical Society* 121.13 (1999), pp. 3214–3217.

[36] W. E. Kaden et al. “Electronic Structure Controls Reactivity of Size-Selected Pd Clusters Adsorbed on TiO_2 Surfaces”. *Science* 326.5954 (2009), pp. 826–829.

[37] Y. Watanabe et al. “Size-dependent catalytic activity and geometries of size-selected Pt clusters on TiO_2 (110) surfaces”. *Catalysis Science & Technology* 1.8 (2011), pp. 1490–1495.

[38] M. Nesselberger et al. “The particle size effect on the oxygen reduction reaction activity of Pt catalysts: influence of electrolyte and relation to single crystal models”. *Journal of the American Chemical Society* 133.43 (2011), pp. 17428–17433.

[39] F. F. Schweinberger et al. “Cluster Size Effects in the Photocatalytic Hydrogen Evolution Reaction”. *Journal of the American Chemical Society* 135.36 (2013), pp. 13262–13265.

[40] M. Nesselberger et al. “The effect of particle proximity on the oxygen reduction rate of size-selected platinum clusters”. *Nature materials* 12.10 (2013), pp. 919–924.

[41] A. Bruix et al. “A New Type of Strong Metal–Support Interaction and the Production of H_2 through the Transformation of Water on Pt/CeO_2 (111) and Pt/CeO x/TiO_2 (110) Catalysts”. *Journal of the American Chemical Society* 134.21 (2012), pp. 8968–8974.

[42] Y. Nakato and H. Tsubomura. “Structures and functions of thin metal layers on semiconductor electrodes”. *Journal of Photochemistry* 29.1 (1985), pp. 257–266.

[43] S. M. Sze and K. K. Ng. *Physics of semiconductor devices*. John Wiley & Sons, 2006.

[44] P. Atkins and J. de Paula. *Atkins’ Physical Chemistry*. OUP Oxford, 2010.

[45] A. D. McNaught and A. D. McNaught. *Compendium of chemical terminology*. Vol. 1669. Blackwell Science Oxford, 1997.

[46] T. Erdey-Gruz and M. Volmer. “Zur theorie der wasserstoffüberspannung”. *Z. Phys. Chem. A* 150 (1930), p. 203.

[47] M. Mason. “Electronic structure of supported small metal clusters”. *Physical review B* 27.2 (1983), p. 748.

[48] P. Fayet et al. “Electronic structure of supported mass-selected transition metal clusters: a photoemission study”. *Surface Science* 269–270 (1992), pp. 1101–1108.

[49] Y. Xu, W. A. Shelton, and W. F. Schneider. “Effect of particle size on the oxidizability of platinum clusters”. *The Journal of Physical Chemistry A* 110.17 (2006), pp. 5839–5846.

[50] W. B. Schneider, U. Benedikt, and A. A. Auer. “Interaction of Platinum Nanoparticles with Graphitic Carbon Structures: A Computational Study”. *ChemPhysChem* 14.13 (2013), pp. 2984–2989.

[51] L. Xiao and L. Wang. “Structures of platinum clusters: Planar or spherical?” *The Journal of Physical Chemistry A* 108.41 (2004), pp. 8605–8614.

[52] Z. Jiang et al. “Direct XPS evidence for charge transfer from a reduced rutile TiO_2 (110) surface to Au clusters”. *The Journal of Physical Chemistry C* 111.33 (2007), pp. 12434–12439.

[53] G. Ramos-Sanchez and P. B. Balbuena. “Interactions of Platinum Clusters with a Graphite Substrate”. *Phys. Chem. Chem. Phys.* (2013).

[54] Y. Nie et al. “Size dependent 2p $_{3/2}$ binding-energy shift of Ni nanoclusters on SiO $_2$ support: Skin-depth local strain and quantum trapping”. *Applied Surface Science* 256.14 (2010), pp. 4667–4671.

[55] V. Borman et al. “Evolution of the electronic properties of transition metal nanoclusters on graphite surface”. *Journal of Experimental and Theoretical Physics* 110.6 (2010), pp. 1005–1025.

[56] R. C. Weast. *Handbook of chemistry and physics*. CRC Press Inc., 1985.

[57] B. Elger. “Charakterisierung einer Magnetron-Sputterquelle zur Herstellung massenselektierter Metallcluster”. MA thesis. TU Darmstadt, 2012.

[58] B. M. Smirnov. “Generation of cluster beams”. *Physics-Uspekhi* 46.6 (2003), pp. 589–628.

[59] D. Briggs and P. Seah. *Practical Surface Analysis, Auger and X-ray Photoelectron Spectroscopy*. Practical Surface Analysis. Wiley, 1990.

[60] J. C. Vickerman and I. S. Gilmore. *Surface analysis: the principal techniques*. Vol. 2. Wiley Online Library, 2009.

[61] G. Wertheim. “Electronic structure of metal clusters”. *Small Particles and Inorganic Clusters*. Springer, 1989, pp. 319–326.

[62] J. H. Thomas III and S. Hofmann. “Ion bombardment induced changes in silicon dioxide surface composition studied by x-ray photoelectron spectroscopy”. *Journal of Vacuum Science & Technology A* 3.5 (1985), pp. 1921–1928.

[63] M. Seah and W. Dench. “Quantitative electron spectroscopy of surfaces: a standard data base for electron inelastic mean free paths in solids”. *Surface and interface analysis* 1.1 (1979), pp. 2–11.

[64] J. Yeh and I. Lindau. “Atomic subshell photoionization cross sections and asymmetry parameters: $1 \leq Z \leq 103$”. *Atomic data and nuclear data tables* 32.1 (1985), pp. 1–155.

[65] C. Wagner et al. “Empirical atomic sensitivity factors for quantitative analysis by electron spectroscopy for chemical analysis”. *Surface and Interface Analysis* 3.5 (2004), pp. 211–225.

[66] N. Fairley and A. Carrick. *The Casa cookbook: Recipes for XPS data processing*. Knutsford: Acolyte Science, 2005.

[67] C. Powell and A. Jablonski. *NIST Electron Inelastic-Mean-Free-Path Database, Version 1.2, SRD 71*. National Institute of Standards and Technology; Gaithersburg, MD, 2010.

[68] S. Tanuma, C. J. Powell, and D. R. Penn. “Calculations of electron inelastic mean free paths (IMFPS). IV. Evaluation of calculated IMFPs and of the predictive IMFP formula TPP-2 for electron energies between 50 and 2000 eV”. *Surface and Interface Analysis* 20.1 (1993), pp. 77–89.

[69] A. Klein et al. “Photoelectron spectroscopy in materials science and physical chemistry”. *Bunsen-Magazin* 10.4 (2008), pp. 124–139.

[70] J. M. Doña Rodríguez, J. A. Herrera Melián, and J. Pérez Peña. “Determination of the real surface area of Pt electrodes by hydrogen adsorption using cyclic voltammetry”. *Journal of Chemical Education* 77.9 (2000), p. 1195.

[71] D. Chen et al. “Determining the Active Surface Area for Various Platinum Electrodes”. English. *Electrocatalysis* 2.3 (2011), pp. 207–219.

[72] S. Trasatti and O. Petrii. “Real surface area measurements in electrochemistry”. *Pure and applied chemistry* 63.5 (1991), pp. 711–734.

[73] F. J. Vidal-Iglesias et al. “Electrochemical characterization of shape-controlled Pt nanoparticles in different supporting electrolytes”. *ACS Catalysis* 2.5 (2012), pp. 901–910.

[74] *Practice for Conversion Between Resistivity and Dopant or Carrier Density for Boron-Doped, Phosphorous-Doped, and Arsenic-Doped Silicon*. SEMI MF723-0307E. Semiconductor Equipment and Materials International.

[75] G. Pietsch. “Hydrogen on Si: Ubiquitous surface termination after wet-chemical processing”. *Applied Physics A: Materials Science & Processing* 60.4 (1995), pp. 347–363.

[76] J. Hill et al. “Properties of oxidized silicon as determined by angular-dependent X-ray photoelectron spectroscopy”. *Chemical Physics Letters* 44.2 (1976), pp. 225–231.

[77] X. G. Zhang. *Electrochemistry of Silicon and its Oxide*. Springer, 2001.

[78] I. Constant, F. Tardif, and J. Derrien. “Deposition and removal of sodium contamination on silicon wafers”. *Semiconductor science and technology* 15.1 (2000), p. 61.

[79] M. R. Houston and R. Maboudian. “Stability of ammonium fluoride-treated Si(100)”. *Journal of Applied Physics* 78.6 (1995), pp. 3801–3808.

[80] J. M. C. Thornton and R. H. Williams. “An S/XPS study of hydrogen terminated, ordered silicon (100) and (111) surfaces prepared by chemical etching”. *Physica Scripta* 41.6 (1990), p. 1047.

[81] J. Shi, D. Kojima, and M. Hashimoto. “The interaction between platinum films and silicon substrates: Effects of substrate bias during sputtering deposition”. *Journal of Applied Physics* 88.3 (2000), pp. 1679–1683.

[82] B. E. Deal et al. “Characteristics of the Surface-State Charge (Qss) of Thermally Oxidized Silicon”. *Journal of The Electrochemical Society* 114.3 (1967), pp. 266–274.

[83] D. K. Schroder. *Semiconductor material and device characterization*. John Wiley & Sons, 2006.

[84] S. Sze, D. Coleman Jr, and A. Loya. “Current transport in metal-semiconductor-metal (MSM) structures”. *Solid-State Electronics* 14.12 (1971), pp. 1209–1218.

[85] P. Mur et al. “Ultra-thin oxides grown on silicon (1 0 0) by rapid thermal oxidation for CMOS and advanced devices”. *Applied Surface Science* 175–176 (2001), pp. 726–733.

[86] Y. Lee et al. “Ultrathin oxide passivation layer by rapid thermal oxidation for the silicon heterojunction solar cell applications”. *International Journal of Photoenergy* 2012 (2012).

[87] J. Nulman, J. Krusius, and A. Gat. “Rapid thermal processing of thin gate dielectrics. Oxidation of silicon”. *Electron Device Letters, IEEE* 6.5 (1985), pp. 205–207.

[88] F. Rochet et al. “The thermal oxidation of silicon the special case of the growth of very thin films”. *Advances in Physics* 35.3 (1986), pp. 237–274.

[89] F. Himpsel, G. Hollinger, and R. Pollak. “Determination of the Fermi-level pinning position at Si (111) surfaces”. *Physical Review B* 28.12 (1983), p. 7014.

[90] Y. Kim, T. Wei, and D. Goodman. “Identification of defect sites on SiO_2 thin films grown on Mo (112)”. *Langmuir* 19.2 (2003), pp. 354–357.

[91] J. L. Alay and M. Hirose. “The valence band alignment at ultrathin SiO_2/Si interfaces”. *Journal of Applied Physics* 81.3 (1997), pp. 1606–1608.

[92] H. Nohira et al. “Valence band edge of ultra-thin silicon oxide near the interface”. *Applied Surface Science* 123–124 (1998), pp. 546–549.

[93] A. Kramida et al. NIST Atomic Spectra Database (ver. 5.2), [Online]. Available: `http://physics.nist.gov/asd` [2015, August 10]. National Institute of Standards and Technology, Gaithersburg, MD. 2014.

[94] G. Hollinger et al. “X-ray photoelectron spectroscopy of thermally grown silicon dioxide films on silicon”. *Chemical Physics Letters* 36.4 (1975), pp. 441–445.

[95] C. Ionescu, M. A. Ionescu, and I. Ciuca. “Pyrometer calibration, sample mounting, and sample processing for Silicon (111)-7x7 reconstruction”. English. *Optoelectronics and Advanced Materials: Rapid Communications* 5.11 (Nov. 2011), 1213–1215.

[96] S. Morgan, R. Williams, and J. Mooney. “An XPS study of thin Pt and Ir silicide overlayer formation on Si (100) 2 X 1 surfaces”. *Applied surface science* 56 (1992), pp. 493–500.

[97] Z. A. Weinberg, G. W. Rubloff, and E. Bassous. “Transmission, photoconductivity, and the experimental band gap of thermally grown SiO_2 films”. *PhysRevB* 19 (6 Mar. 1979), pp. 3107–3117.

[98] J. Klett et al. “Band engineering for efficient catalyst-substrate coupling for photoelectrochemical water splitting”. *Physical Chemistry Chemical Physics* accepted (2016).

[99] B. Beverskog and I. Puigdomenech. “Revised Pourbaix diagrams for nickel at 25–300 degC”. *Corrosion Science* 39.5 (1997), pp. 969–980.

[100] K. Nakaoka, J. Ueyama, and K. Ogura. “Semiconductor and electrochromic properties of electrochemically deposited nickel oxide films”. *Journal of Electroanalytical Chemistry* 571.1 (2004), pp. 93–99.

[101] S. Uhlenbrock et al. “The influence of defects on the Ni 2p and O 1s XPS of NiO”. *Journal of Physics: Condensed Matter* 4.40 (1992), p. 7973.

[102] J. M. McKay and V. E. Henrich. “Structure of valence and conduction levels in NiO”. *Physical review letters* 53.24 (1984), p. 2343.

[103] A. Varkey and A. Fort. “Solution growth technique for deposition of nickel oxide thin films”. *Thin Solid Films* 235.1–2 (1993), pp. 47–50.

[104] P. Tengvall and I. Lundström. “Physico-chemical considerations of titanium as a biomaterial”. *Clinical materials* 9.2 (1992), pp. 115–134.

[105] V. Pfeifer et al. “Energy Band Alignment between Anatase and Rutile TiO_2”. *The Journal of Physical Chemistry Letters* 4.23 (2013), pp. 4182–4187.

[106] K.-L. Ou et al. “Titanium dioxide electron-selective interlayers created by chemical vapor deposition for inverted configuration organic solar cells”. *Journal of Materials Chemistry A* 1.23 (2013), pp. 6794–6803.

[107] R. Sanjinés et al. “Electronic structure of anatase TiO_2 oxide”. *Journal of Applied Physics* 75.6 (1994), pp. 2945–2951.

[108] A. Burke et al. “Ignition mechanism of the titanium–boron pyrotechnic mixture”. *Surface and Interface Analysis* 11.6-7 (1988), pp. 353–358.

[109] V. Mikhelashvili and G. Eisenstein. “Optical and electrical characterization of the electron beam gun evaporated TiO_2 film”. *Microelectronics Reliability* 41.7 (2001), pp. 1057–1061.

[110] J. F. Moulder et al. *Handbook of X-Ray Photoelectron Spectroscopy*. Ed. by J. Chastain and R. C. King. Physical Electronics Inc., 1995.

[111] A. Sasahara, C. L. Pang, and H. Onishi. “Probe Microscope Observation of Platinum Atoms Deposited on the TiO_2(110)-(1x1) Surface”. *The Journal of Physical Chemistry B* 110.27 (2006). PMID: 16821870, pp. 13453–13457.

[112] L. Forro et al. “High mobility n-type charge carriers in large single crystals of anatase (TiO_2)”. *Journal of Applied Physics* 75.1 (1994), pp. 633–635.

[113] B. Seger et al. “Silicon protected with atomic layer deposited TiO_2: durability studies of photocathodic H_2 evolution”. *Rsc Advances* 3.48 (2013), pp. 25902–25907.

[114] Y. Takasu et al. “Electrocatalytic properties of ultrafine platinum particles for hydrogen electrode reaction in an aqueous solution of sulfuric acid”. *Electrochimica Acta* 34.3 (1989), pp. 453–458.

[115] F. Heinz. “In situ Charakterisierung von einkristallinen Platinoberflächen”. B.S. Thesis. TU Darmstadt, 2014.

[116] Kibler. *Preparation and Characterization of Noble Metal Single Crystal Electrode Surfaces*. 2003.

[117] S. Shaikhutdinov, M. Ritter, and W. Weiss. “Hexagonal heterolayers on a square lattice: A combined STM and LEED study of FeO (111) on Pt (100)”. *Physical Review B* 62.11 (2000), p. 7535.

[118] P. van Beurden. “On the surface reconstruction of Pt-Group metals : a theoretical study of adsorbate-induced dynamics”. PhD thesis. Ein dhoven University of Technolog, 2003.

[119] T. Zhu et al. “Reconstruction of Clean and Oxygen-Covered Pt (110) Surfaces”. *The Journal of Physical Chemistry C* 117.21 (2013), pp. 11251–11257.

[120] B.-C. Lin and C.-S. Shern. “A Study of Pt (110) Surface Reconstruction and Oxygen-Chemisorption”. *Chinese Journal of Physics* 28.4 (1990), pp. 355–366.

[121] A. Von Oertzen et al. “The scanning photoemission microscope: a novel tool in surface science”. *Ultramicroscopy* 36.1 (1991), pp. 107–116.

[122] K. Yamamoto et al. “Hydrogen adsorption and oxide formation on platinum single crystal electrodes”. *Journal of Electroanalytical Chemistry and Interfacial Electrochemistry* 96.2 (1979), pp. 233–239.

[123] N. Furuya and M. Shibata. “Structural changes at various Pt single crystal surfaces with potential cycles in acidic and alkaline solutions”. *Journal of Electroanalytical Chemistry* 467.1 (1999), pp. 85–91.

[124] H. Herrera-Suárez, A. Rubio-Ponce, and D. Olguín. “Electronic band structure of platinum low-index surfaces: an ab initio and tight-binding study. II”. *Revista mexicana de física* 58.1 (2012), pp. 46–54.

[125] W. Di, K. E. Smith, and S. D. Kevan. “Angle-resolved photoemission study of the clean and hydrogen-covered Pt (111) surface”. *Physical Review B* 45.7 (1992), p. 3652.

[126] S. Meng, E. Wang, and S. Gao. “Water adsorption on metal surfaces: A general picture from density functional theory studies”. *Physical Review B* 69.19 (2004), p. 195404.

[127] H. Bonzel and R. Ku. “Adsorbate interactions on a Pt (110) surface. I. Sulfur and carbon monoxide”. *The Journal of Chemical Physics* 58.10 (2003), pp. 4617–4624.

[128] B. Winter et al. “Full valence band photoemission from liquid water using EUV synchrotron radiation”. *The Journal of Physical Chemistry A* 108.14 (2004), pp. 2625–2632.

[129] A. Nilsson et al. “The hydrogen bond in ice probed by soft x-ray spectroscopy and density functional theory”. *The Journal of Chemical Physics* 122.15, 154505 (2005).

[130] R. Blanco and J. M. Orts. “B3LYP study of water adsorption on cluster models of Pt (111), Pt (100) and Pt (110): Effect of applied electric field”. *Electrochimica Acta* 53.26 (2008), pp. 7796–7804.

[131] H. Ogasawara et al. “Structure and bonding of water on Pt (111)”. *Physical review letters* 89.27 (2002), p. 276102.

[132] A. Eva. “Metalorganic Chemical Vapor Deposition of Platinum Nanoparticles for Water Electrolysis”. MA thesis. TU Darmstadt, 2014.

[133] J. Klett et al. “Electrocatalytic Performance of High-Surface-Area Platinum Catalysts Synthesized by Chemical Vapor Deposition for Water Splitting”. *ChemCatChem* 8 (2 2016), pp. 345–351.

[134] I. Igumenov et al. “Overview of Coating Growth Mechanisms in MOCVD Processes as Observed in Pt Group Metals”. *Chemical Vapor Deposition* 13.11 (2007), pp. 633–637.

[135] Morozova, N. B. et al. “Vapor pressure of precursors for CVD on the base of platinum group metals”. *J. Phys. IV France* 11 (2001).

[136] J. S. Chickos and W. E. Acree Jr. “Enthalpies of sublimation of organic and organometallic compounds. 1910–2001”. *Journal of Physical and Chemical Reference Data* 31.2 (2002), pp. 537–698.

[137] F. Urbain et al. “a-Si:H/μc-Si:H tandem junction based photocathodes with high open-circuit voltage for efficient hydrogen production”. *Journal of Materials Research* 29 (22 2014), pp. 2605–2614.

[138] N. L. Jeon et al. “Selective Chemical Vapor Deposition of Platinum and Palladium Directed by Monolayers Patterned Using Microcontact Printing”. *Langmuir* 13.14 (1997), pp. 3833–3838.

[139] I. Karakaya and W. Thompson. “The Ag-Pt (Silver-Platinum) system”. *Journal of Phase Equilibria* 8.4 (1987), pp. 334–340.

[140] M. Seah, I. Gilmore, and G. Beamson. “XPS: binding energy calibration of electron spectrometers 5—re-evaluation of the reference energies”. *Surface and Interface Analysis* 26.9 (1998), pp. 642–649.

[141] C. Powell. “Recommended Auger parameters for 42 elemental solids”. *Journal of Electron Spectroscopy and Related Phenomena* 185.1–2 (2012), pp. 1–3.

[142] S. Doniach and M. Sunjic. “Many-electron singularity in X-ray photoemission and X-ray line spectra from metals”. *Journal of Physics C: Solid State Physics* 3.2 (2001), p. 285.

[143] T. Cheung. “Lineshape studies of the X-ray photoemission of small metal clusters”. *Surface Science Letters* 127.2 (1983), pp. L129–L134.

[144] M. T. Schaal et al. “Theoretical and experimental studies of Ag–Pt interactions for supported Ag–Pt bimetallic catalysts”. *Surface Science* 603.4 (2009), pp. 690–696.

[145] T. Härtel, U. Strüber, and J. Küppers. “Growth and properties of thin Ag films on Pt (111) surfaces”. *Thin Solid Films* 229.2 (1993), pp. 163–170.

[146] J. A. Rodriguez and M. Kuhn. “Electronic and Chemical Properties of Ag/Pt (111) and Cu/Pt (111) Surfaces: Importance of Changes in the d Electron Populations”. *The Journal of Physical Chemistry* 98.44 (1994), pp. 11251–11255.

[147] D. Shuzhong, X. Fanhua, and D. Jingfa. “The adsorption of oxygen and the oxidation of methanol on silver-platinum alloys”. *Journal of Catalysis* 109.1 (1988), pp. 170–179.

[148] C. Kittel. “Introduction to Solid State Physics, (Wiley, New York, 1976).” *K. Balasubramanian, Chem. Rev.* 35 (1990), pp. 90–93.

[149] J. Keister et al. “Photoemission spectroscopy of platinum overlayers on silicon dioxide films”. *Journal of Vacuum Science & Technology B* 18.4 (2000), pp. 2174–2178.

[150] W. Eberhardt et al. “Photoemission from mass-selected monodispersed Pt clusters”. *Physical Review Letters* 64.7 (1990), pp. 780–783.

[151] S. Peters et al. “Size-dependent XPS spectra of small supported Au-clusters”. *Surface Science* 608 (2013), pp. 129–134.

[152] D. M. Mattox. *Handbook of physical vapor deposition (PVD) processing*. William Andrew, 2010.

[153] S. Hofmann and J. Thomas III. “An XPS study of the influence of ion sputtering on bonding in thermally grown silicon dioxide”. *Journal of Vacuum Science & Technology B* 1.1 (1983), pp. 43–47.

[154] S. Danyluk and G. McGuire. “Platinum silicide formation: Electron spectroscopy of the platinum-platinum silicide interface”. *Journal of Applied Physics* 45.12 (1974), pp. 5141–5144.

[155] J. Hammond and N. Winograd. “XPS spectroscopic study of potentiostatic and galvanostatic oxidation of Pt electrodes in H_2SO_4 and $HClO_4$”. *Journal of Electroanalytical Chemistry and Interfacial Electrochemistry* 78.1 (1977), pp. 55–69.

[156] M. Peuckert and H. P. Bonzel. “Characterization of oxidized platinum surfaces by X-ray photoelectron spectroscopy”. *Surface Science* 145.1 (1984), pp. 239–259.

[157] L. Da Silva et al. “XPS study of the state of iridium, platinum, titanium and oxygen in thermally formed $IrO_2 + TiO_2 + PtO_X$ films”. *Colloids and Surfaces A: Physicochemical and Engineering Aspects* 170.2 (2000), pp. 119–126.

[158] M. Turra et al. “An improved time-of-flight method for cluster deposition and ion-scattering experiments”. *Review of Scientific Instruments* 79.1, 013905 (2008), p. 013905.

[159] W. Eberhardt et al. “Core level photoemission from monosize mass selected Pt clusters deposited on SiO_2 and amorphous carbon”. *Physica Scripta* 41.6 (1990), p. 892.

[160] D. C. Lim et al. “Chemistry of mass-selected Au clusters deposited on sputter-damaged HOPG surfaces: The unique properties of Au_8 clusters”. *Chemical physics letters* 439.4 (2007), pp. 364–368.

[161] J. Klett et al. “The Electronic Interaction of Pt-Clusters with ITO and HOPG Surfaces upon Water Adsorption”. *Zeitschrift für Physikalische Chemie* 228.4-5 (2014), pp. 503–520.

[162] M. A. Henderson. “The interaction of water with solid surfaces: fundamental aspects revisited”. *Surface Science Reports* 46.1–8 (2002), pp. 1–308.

[163] T. Mayer et al. “Elementary processes at semiconductor/electrolyte interfaces: perspectives and limits of electron spectroscopy”. *Applied surface science* 252.1 (2005), pp. 31–42.

[164] H. Y. Yu et al. “Surface electronic structure of plasma-treated indium tin oxides”. *Applied Physics Letters* 78.17 (2001), pp. 2595–2597.

[165] S. Krischok et al. “H_2O interaction with bare and Li-precovered TiO_2 : studies with electron spectroscopies (MIES and UPS(HeI and II))”. *Surface Science* 495.1 - 2 (2001), pp. 8–18.

[166] D. B. Asay and S. H. Kim. “Evolution of the adsorbed water layer structure on silicon oxide at room temperature”. *The Journal of Physical Chemistry B* 109.35 (2005), pp. 16760–16763.

[167] O. Sneh and S. M. George. “Thermal stability of hydroxyl groups on a well-defined silica surface”. *The Journal of physical chemistry* 99.13 (1995), pp. 4639–4647.

[168] S. Wendt et al. “The interaction of water with silica thin films grown on Mo (112)”. *Surface science* 565.2 (2004), pp. 107–120.

[169] J. Klett et al. “Water dissociation on silica in the presence of atomic platinum”. *Applied Surface Science* (submitted 2016).

[170] G. Pacchioni and G. Ierańo. “Ab initio theory of optical transitions of point defects in SiO_2”. *Physical Review B* 57.2 (1998), p. 818.

[171] L. Giordano et al. “Electron trapping at point defects on hydroxylated silica surfaces”. *Physical review letters* 99.13 (2007), p. 136801.

[172] L. Skuja et al. “Defects in oxide glasses”. *physica status solidi (c)* 2.1 (2005), pp. 15–24.

[173] Y. Kim et al. “Dissociation of water on a flat, ordered silica surface”. *Langmuir* 19.4 (2003), pp. 1140–1142.

[174] J.-M. Antonietti et al. “Optical absorption spectrum of gold atoms deposited on SiO_2 from cavity ringdown spectroscopy”. *Physical review letters* 94.21 (2005), p. 213402.

[175] A. M. Shor et al. “Small silver clusters at paramagnetic defects of silica surfaces: A density functional embedded-cluster study”. *Surface Science* 604.19–20 (2010), pp. 1705–1712.

[176] U. Martinez, L. Giordano, and G. Pacchioni. “Nature of point defects on SiO_2/Mo (112) thin films and their interaction with Au atoms”. *The Journal of Physical Chemistry B* 110.34 (2006), pp. 17015–17023.

[177] H. Kobayashi et al. “Mechanism of platinum-enhanced oxidation of silicon at low temperatures”. *The Journal of Chemical Physics* 109.12 (1998), pp. 4997–5001.

[178] G. Firpo et al. “High performance portable vacuum suitcase”. *Review of scientific instruments* 76.2 (2005), pp. 026108–026108.

[179] C. Benvenuti and P. Chiggiato. “Pumping characteristics of the St707 nonevaporable getter (Zr 70 V 24.6 Fe 5.4 wt%)”. *Journal of Vacuum Science & Technology A: Vacuum, Surfaces, and Films* 14.6 (1996), pp. 3278–3282.

[180] G. Firpo and A. Pozzo. “New getter pump for ultrahigh vacuum systems and transportable enclosure”. *Review of Scientific Instruments* 75.11 (2004), pp. 4828–4832.

[181] SAES Getters. *Non eveporable getters - Activation at low temperatures*.

[182] K. Jousten. “Ultrahigh vacuum gauges”. *CERN Accelerator School Vacuum in accelerators* (2007), p. 145.

[183] J. Ziegler. “Photoelektrosynthese von Wasserstoff mit Silizium-Dünnschicht-Tandemsolarzellen”. PhD thesis. TU Darmstadt, 2015.

[184] B. Seger et al. “Using TiO_2 as a Conductive Protective Layer for Photocathodic H_2 Evolution”. *Journal of the American Chemical Society* 135.3 (2013). PMID: 23289745, pp. 1057–1064.

[185] G. Malandrino, R. L. Nigro, and I. L. Fragalà. “MOCVD of Platinum (100) Films on Random Hastelloy C276”. *Chemical Vapor Deposition* 5.2 (1999), pp. 59–61.

[186] D. V. Esposito et al. “Low-Cost Hydrogen-Evolution Catalysts Based on Monolayer Platinum on Tungsten Monocarbide Substrates”. *Angewandte Chemie International Edition* 49.51 (2010), pp. 9859–9862.

[187] D. V. Esposito and J. G. Chen. “Monolayer platinum supported on tungsten carbides as low-cost electrocatalysts: opportunities and limitations”. *Energy & Environmental Science* 4.10 (2011), pp. 3900–3912.

A Acknowledgments

Im Folgenden möchte ich gerne einer Reihe an Personen danken, ohne welche die Erstellung dieser Arbeit nicht möglich gewesen wäre.

Zunächst gilt mein Dank Professor Schäfer und Professor Jaegermann welche mir die Arbeit an diesem interessanten Thema überhaupt ermöglicht haben. Es war mir eine große Freude in beiden Arbeitsgruppen involviert zu sein. Trotz der großen gewährten Freiheiten hat es nie an Anleitung oder hilfreichen Diskussionen gemangelt – hierfür mein Dank.

Frau Prof. Kramm und Herrn Prof. Hess möchte ich gerne für das Lesen und Bewerten der Dissertation, sowie der noch ausstehenden mündlichen Prüfung, danken.

Dr. Kaiser möchte ich ebenso für die Betreuung während meiner Arbeit danken.

Für Ihren steten Einsatz an der "Crazy-Daisy" um Cluster zu preparieren, bedanke ich mich bei Stephan Krähling, Benjamin Elger und unserem Späteinsteiger Florian Neuberger. Weiterhin viel Erfolg beim Schrauben drehen, Muttern drehen...

Den fleißigen Lesern Jürgen Ziegler und Anke Schachtsiek danke ich für die ausgiebige inhaltliche und formale Korrektur. Insbesondere die Diskussionen mit Jürgen waren sehr hilfreich und deckten auch die kleinsten Fehler auf.

Ich weiß auch die Hilfe des Werkstattteams um Jochen Rank und Michael Weber sehr zu schätzen. Dies gilt im Besonderen für die mobile UHV Transportkammer, welche nicht ohne die tatkräftige Unterstützung des Teams so schnell und zuverlässig einsatzbereit gewesen.

Den von mir betreuten Studenten Andreas Eva und Frederick Heinz danke ich für ihr großes Engagement und eine hervorragende Zusammenarbeiten. Beiden wünsche ich alles gute für die Zukunft.

Am BESSY möchte ich mich gerne bei Wolfram Calvet bedanken. Ohne seine ständige Unterstützung vor Ort wären viele Messungen vermutlich nicht möglich gewesen. Ansonsten gilt mein Dank natürlich auch den ganz Mitfahrern nach Berlin: Jürgen Ziegler, Sven Tengeler, Natascha Weidler, Florent Yang, Ruben Precht, Philip Reckers und Markus Motzko. Ohne euch wären die Aufenthalte nicht halb so amüsant gewesen.

All den restlichen Kollegen möchte ich sagen, dass es eine wunderbare Zeit war und danke Ihnen für die hervorragende Gruppenatmosphäre.

Zu guter Letzt, möchte ich meinen Eltern danken, deren uneingeschränkter Unterstützung ich mir stets sicher sein konnte.

Financial support of this project by the DFG priority program SPP 1613 as well as by the DFG Excellence Initiative, Darmstadt Graduate School of Energy Science and Engineering (GSC 1070) is gratefully acknowledged. Further, I like to thank the Helmholtz-Zentrum Berlin Electron Storage Ring BESSY II for provision of synchrotron radiation at U49-2 and support of the travel expenses.

B Curriculum Vitae

Employment History

Mar 2012 - Present TU Darmstadt – Eduard-Zintl-Insitut für physikalsiche Chemie, Germany

Research Associate

Research associate within the DFG SPP 1613, Fuels Produced Regeneratively Through Light-Driven Water Splitting: Clarification of the Elemental Processes Involved and Prospects for Implementation in Technological Concepts

Aug 2010 - Dec 2010 Merck KGaA, Darmstadt, Germany

Internship

Characterization of fluorescent powders for LED-applications

Education

2012-Today PhD student in Physical Chemistry, TU Darmstadt, Germany

Thesis: Interface and catalyst investigation for solar water splitting

2006-2011 Dipl.-Ing. in Materials Science, TU Darmstadt, Germany

Thesis: Optimierung von GaP–Rückkontakten zur photochemischen Wasserspaltung

2008-2009 Exchange student at University of Illinois at Urbana-Champaign, USA

2005 Abitur (general qualification for university entrance) Justus-Liebig-Schule, Darmstadt, Germany

Joachim Klett, Darmstadt den 04. Februar 2016

Publications

- **Klett, J.**; Krähling, S.; Elger, B.; Schäfer, R.; Kaiser, B. & Jaegermann, W. The Electronic Interaction of Pt-Clusters with ITO and HOPG Surfaces upon Water Adsorption *Zeitschrift für Physikalische Chemie*, 228, 503-520, 2014

- **Klett, J.**; Eva, A.; Heinz, F.; Kaiser, B.; Jaegermann, W. & Schäfer, R. Electrocatalytic Performance of High-Surface-Area Platinum Catalysts Synthesized by Chemical Vapor Deposition for Water Splitting *ChemCatChem*, WILEY-VCH Verlag, 8, 345-351, 2016

- **Klett, J.**; Ziegler, J.; Radetinac, A.; Kaiser, B.; Schäfer, R.; Jaegermann, W.; Urbain, F.; Becker, J.-P.; Smirnov, V. & Finger, F. Band engineering for efficient catalyst-substrate coupling for photoelectrochemical water splitting *Physical Chemistry Chemical Physics*, Royal Society of Chemistry, **in press**, 2016

- **Klett, J.**; Elger, B.; Krähling, S.; Kaiser, B.; Jaegermann, W. & Schäfer, R. Water dissociation on silica in the presence of atomic platinum *Applied Surface Science*, **accepted**, 2016

- Kaiser, B.; Fertig, D.; Ziegler, J.; **Klett, J.**; Hoch, S. & Jaegermann, W. Solar Hydrogen Generation with Wide-Band-Gap Semiconductors: GaP (100) Photoelectrodes and Surface Modification *ChemPhysChem*, 13, 3053-3060, 2012

- Calvet, W.; Murugasen, E.; **Klett, J.**; Kaiser, B.; Jaegermann, W.; Finger, F.; Hoch, S.; Blug, M. & Busse, J. Silicon based tandem cells: novel photocathodes for hydrogen production *Physical Chemistry Chemical Physics*, 16, 12043-12050, 2014

- Reckers, P.; Dimamay, M.; **Klett, J.**; Trost, S.; Zilberberg, K.; Riedl, T.; Parkinson, B. A.; Brötz, J.; Jaegermann, W. & Mayer, T. Deep and Shallow TiO_2 Gap States on Cleaved Anatase Single Crystal (101) Surfaces, Nanocrystalline Anatase Films, and ALD Titania Ante and Post Annealing *The Journal of Physical Chemistry C*, 119, 9890-9898, 2015

- Weidler, N.; Paulus, S.; Schuch, J.; **Klett, J.**; Hoch, S.; Maljusch, A.; Brötz, J.; Wittich, C.; Kaiser, B. & Jaegermann, W. CoOx Thin Film Deposited by CVD as Efficient Water Oxidation Catalyst: Change in Oxidation State in XPS and its Correlation to Electrochemical Activity *Physical Chemistry Chemical Physics*, **in press**, 2015

- Jaegermann, W.; Kaiser, B.; Ziegler, J.; **Klett, J.**; Gimenez, S. & Bisquert, J. (Eds.) Chapter: Interface engineering of semiconductor electrodes for photoelectrochemical water splitting: Application of surface characterization with photoelectron spectroscopy. *Photoelectrochemical solar fuel production. From basic principles to advanced devices.* **in press**, 2016

- Jaegermann, W.; Kaiser, B.; Ziegler, J.; Urbain, F.; Becker, J.; Smirnov, V.; Finger, F.; **Klett, J.** & Schäfer, R. Optimisation and characterisation of thin-film multijunction photovoltaic cells based on silicon for buried junction photovoltaic-electrochemical water splitting devices *Materials Chemistry A*, **submitted**, 2016

Conference contributions

- Spring EMRS 2014 Conference in Lille, France (Presentation)
- MSE 2014 Conference in Darmstadt, Germany (Poster)
- SolarFuels15 Conference in Palma de Mallorca, Spain (Poster)